Palacky University, Olomouc
Faculty of Science
Department of Experimental Physics

Iron Oxide Nanoparticles Prepared by Thermally Induced Decomposition of Ferrous Oxalate Dihydrate

Doctoral Dissertation
Martin Heřmánek

ACKNOWLEDGEMENTS

I would like to express my gratitude to all those who gave me a hand to complete this doctoral dissertation:

I am especially deeply indebted to my supervisor Miroslav Mašláň and consultant Radek Zbořil for their guidance and thought-provoking ideas.

I warmly thank to:

Ivo Medřík for sample preparation,

Jiří Pechoušek for BET measurements,

Institute of Physics of Materials in Brno for XRD patterns,

Čeněk Gregor for catalysis measurements,

Dalibor Jančík for TEM images,

Milan Vůjtek for AFM images and professional and formal advice,

Libor Machala for professional and formal advice and

Jiří Tuček for professional advice.

Many thanks to all my colleagues and friends at the lab. It is a pleasure to co-operate with them.

My special thanks belong to my grandmother who supported my studies and Edita for language correction.

OVERVIEW OF THE AUTHOR'S PUBLICATIONS

1. R. Zboril, L. Machala, M. Mashlan, **M. Hermanek**, M. Miglierini and J. Fojtik, *phys. stat. sol. (c),* 2004, **1**, 12, 3583.

2. R. Zboril, L. Machala, M. Mashlan and **M. Hermanek**, *Industrial Applications of the Mössbauer Effect*, 2005.

3. **M. Hermanek**, R. Zboril, M. Mashlan, L. Machala and O. Schneeweiss, *J. Mater. Chem.,* 2006, **16**, 1273.

AFFIRMATION

I declare that I made prevailing contribution to the publication No 3, the content of which represents a part of this doctoral dissertation.

Olomouc, June 16th 2006.

....

Martin Heřmánek

I, as a co-author of the publication No 3, declare that Martin Heřmánek's contribution to it is prevailing.

....

Radek Zbořil

....

Miroslav Mašláň

....

Libor Machala

....

Oldřich Schneeweiss

CONTENTS

LEAD IN

There are sixteen iron oxides known nowadays, which can be divided into two big groups: a) pure oxides and b) hydroxides and oxides-hydroxides. ***Ferric oxide*** (Fe_2O_3) is a typical representative of the first group. Fe_2O_3 is well known for its polymorphous character – there are four structural modifications of it: α-Fe_2O_3 (hematite; hexagonal structure), β-Fe_2O_3 (cubic structure), γ-Fe_2O_3 (maghemite; cubic structure) and ε-Fe_2O_3 (orthorhombic structure). Iron(III) oxide is widely used in many industrial and scientific fields. In recent years there has been a strong increase in the application potential of Fe_2O_3 particles with dimensions within units–tens nanometers. Such particles are commonly known as ***nanoparticles***.

Thermally induced transformations of iron bearing salts and minerals represent a way of synthesis of nanoparticles. When comparing to other synthetical routes, the solid-state reactions have many indisputable advantages – they are experimentally and cost effective, allow to prepare a relatively huge amount of the material, moreover without a matrix, which significantly enhances its applicability, etc.

The syntheses directly aimed at a particular structural form of Fe_2O_3 (alpha, beta, gamma or epsilon) with appropriate properties, however, demand full comprehension of all possible factors, which may influence the course of the solid-state reactions. Decomposition temperature, time and reaction atmosphere belong to the commonly known ones. It has recently become apparent that the ***sample mass*** and the ***gases evolving during the decomposition*** represent another group of significant conditions, which, what is more, have not been adequately studied yet and therefore are not fully understood.

Hence, the crucial aim of the presented work has been to study the influence of the sample mass and participation of evolving gases on the thermally induced decomposition of ferrous oxalate dihydrate ($FeC_2O_4{\cdot}2H_2O$). Such a study should provide two pieces of information: the first one concerning the influence on the phase composition and the second one describing the obtained materials from the point of view of their dimension, morphology and other properties, which are important for their possible applicability.

Keeping all above mentioned information in mind, the presented work is divided into six main sections. The first one gives a theoretical view on the structures and applications of some iron oxides relevant to this work. The notion ***nanoparticles*** is defined and the most novel application possibilities and ways of syntheses are also discussed. In the second section there are described basic principles of Mössbauer spectroscopy, which has been used as a leading experimental method allowing to perform exact qualitative and quantitative analyses of the phase composition of synthesised materials. The final part of this section introduces some iron oxides from the viewpoint of Mössbauer spectroscopy. The third section discusses up to date knowledge of the thermal decomposition of ferrous oxalate dihydrate ($FeC_2O_4 \cdot 2H_2O$). The reasons leading towards my experimental work are also mentioned. The fourth and fifth sections deal with the obtained results of the thermal decomposition of $FeC_2O_4 \cdot 2H_2O$ from the point of view of the participation of the decomposition gases and the sample mass of $FeC_2O_4 \cdot 2H_2O$ respectively. They give a detailed view on the phase composition of the obtained materials, which was monitored by a powerful combination of Mössbauer spectroscopy and X-Ray powder Diffraction (XRD). The size and morphology of obtained powder materials were studied by Transmission Electron Microscopy (TEM) and Atomic Force Microscopy (AFM). The size properties of the synthesised materials were studied by the measurements of their specific surface areas and computed by the Brunauer-Emmet-Teller (BET) method. The final parts of both fourth and fifth sections refer to the experiments studying the possible applicability of the prepared materials and summarize the obtained results.

1 IRON OXIDES

Iron oxides are commonly widespread almost everywhere in our surroundings. Such broad occurrence has naturally caused an intense interest in Fe oxides in various scientific fields such as medicine, biology, environmental chemistry, geochemistry, soil sciences, etc.

There are generally known sixteen iron oxides,[1] which can be divided into two main groups: A) ***pure oxides*** (hematite α-Fe_2O_3, magnetite Fe_3O_4, maghemite γ-Fe_2O_3, wüstite FeO and the rare forms β-Fe_2O_3 and ε-Fe_2O_3), and B) ***hydroxides*** and ***oxide–hydroxides*** that include: α-FeOOH (goethite), γ-FeOOH (lepidocrocite), β-FeOOH (akagenéite), $Fe_{16}O_{16}(OH)_y(SO_4)_z \cdot nH_2O$ (schwertmannite), δ-FeOOH, δ'-FeOOH (feroxyhyte), high pressure FeOOH, $Fe_5HO_8 \cdot 4H_2O$ (ferrihydrite), $Fe(OH)_3$ (bernalite) and $Fe(OH)_2$.

1.1 STRUCTURES

Iron oxides, hydroxides and oxide hydroxides consist of arrays of Fe ions and O^{2-} or OH^- ions. As the anions (radius of O^{2-} anion is 0.14 nm) are much larger than the cations (the radii of Fe^{III} and Fe^{II} are 0.065 and 0.082 nm respectively), the arrangement of anions governs the crystal structure. In this sense iron oxides are made up of close packed arrays of anions. The commonest arrangement of these sheets of anions in 3D space are ***hexagonal close packing*** (hcp) with the sheets stacked in ABAB… arrangement, and ***cubic close packing*** (ccp) with ABCABC… stacking of anion sheets. The sheets are stacked along some particular crystallographic direction with an average distance within 0.23–0.25 nm. There are twice as many interstices between the sheets of anions as there are anions in a layer. The cations fit either into the octahedral (sixfold coordination) or the smaller tetrahedral interstices. Due to charge balance requirements, in compounds containing Fe^{III} ions only a portion of interstices can be filled and this opens up the possibility of several different arrangements of cations between the anion sheets resulting in different iron oxide structures.

In ideally close packed anion sheets, the O–O distance is 0.304 nm for octahedrally coordinated Fe^{II}, whereas for Fe^{III} it is 0.29 nm in octahedral and 0.33 nm in tetrahedral coordination.

The basic structural unit of iron oxides is the $Fe(O)_6$ octahedron, or more rarely, $Fe(O)_4$ tetrahedron. These units can be mutually bound together either by corners, edges or faces, or by their combinations. As a result, the Fe–Fe distances depend on the type of linkage.

HEMATITE (α-Fe_2O_3)

Hematite is the oldest known Fe oxide and is commonly widespread in rocks and soils. Its colour strongly depends on the grain size and varies from blood-red (fine grains) to black or sparkling grey when coarsely crystalline.

The unit cell of hematite is hexagonal with lattice parameters $a = 0.5034$ nm and $c = 1.3750$ nm. There are six formula units per cell. The structure can be described as consisting of hexagonal close-packed (hcp) arrays of oxygen anions stacked along the [001] direction, i.e. planes of anions are parallel to the (001) plane. Two thirds of the interstices are filled with Fe^{III} ions that are arranged regularly with two filled sites being followed by one vacant site in the (001) plane resulting in the formation of sixfold rings. The arrangement of Fe^{III} cations produces pairs of $Fe(O)_6$ octahedra. Each octahedron shares its edges with three neighbouring octahedra in the same plane and one face with an octahedron in an adjacent plane along the *c*-axis. This face sharing is responsible for the distortion of the cation sublattice resulting in different O–O distances along the shared face (0.2669 nm) and unshared edge (0.3035 nm). Hence the octahedron is trigonally distorted and this distortion influences magnetic properties of hematite.

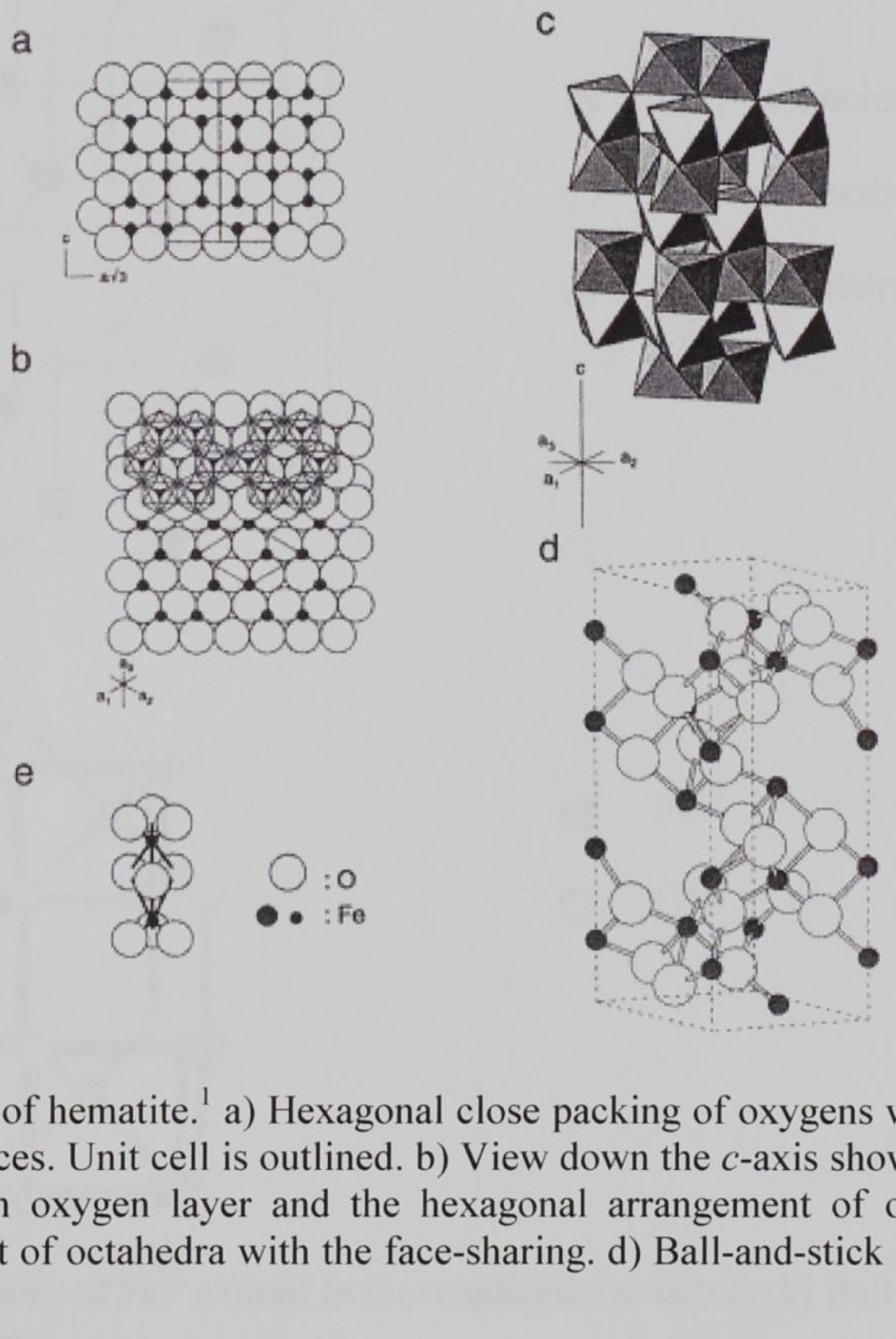

Fig. 1. Crystal structure of hematite.[1] a) Hexagonal close packing of oxygens with cations distributed in the octahedral interstices. Unit cell is outlined. b) View down the *c*-axis showing the distribution of Fe cations over a given oxygen layer and the hexagonal arrangement of octahedra. Unit cell is outlined. c) Arrangement of octahedra with the face-sharing. d) Ball-and-stick model of a unit cell. e) O_3-Fe-O_3-Fe-O_3 triplets.

MAGHEMITE (γ-Fe_2O_3)

The colour of maghemite is red-brown. Natural maghemite occurs in soils as a weathering product of magnetite (maghemite and magnetite are isostructural compounds) or as a product of heating of other iron oxides.

γ-Fe_2O_3 is a cation-deficient defect spinel of an AB_2O_4 structural composition with a cubic unit cell of $a = 0.834$ nm. There are 32 O^{2-} anions together with 64/3 Fe^{III} ions and 8/3 vacant positions per unit cell. Eight cations occupy tetrahedral sites (A) and the remaining cations are randomly distributed over the octahedral sites (B). All vacancies occupy exclusively the B-sites. The stoichiometry formula of maghemite can be therefore generally written as $(Fe_8)^A[Fe_{13.3}\square_{2.67}]^B O_{32}$, in which $\square$ represents vacant sites.

Synthetically prepared maghemites often display so-called superstructure forms that arise as a result of cation (vacancy) ordering. The extent of vacancy ordering is related to the crystallite size, the nature of the precursor and the amount of Fe^{II} in the structure (maghemite/magnetite solid solutions).

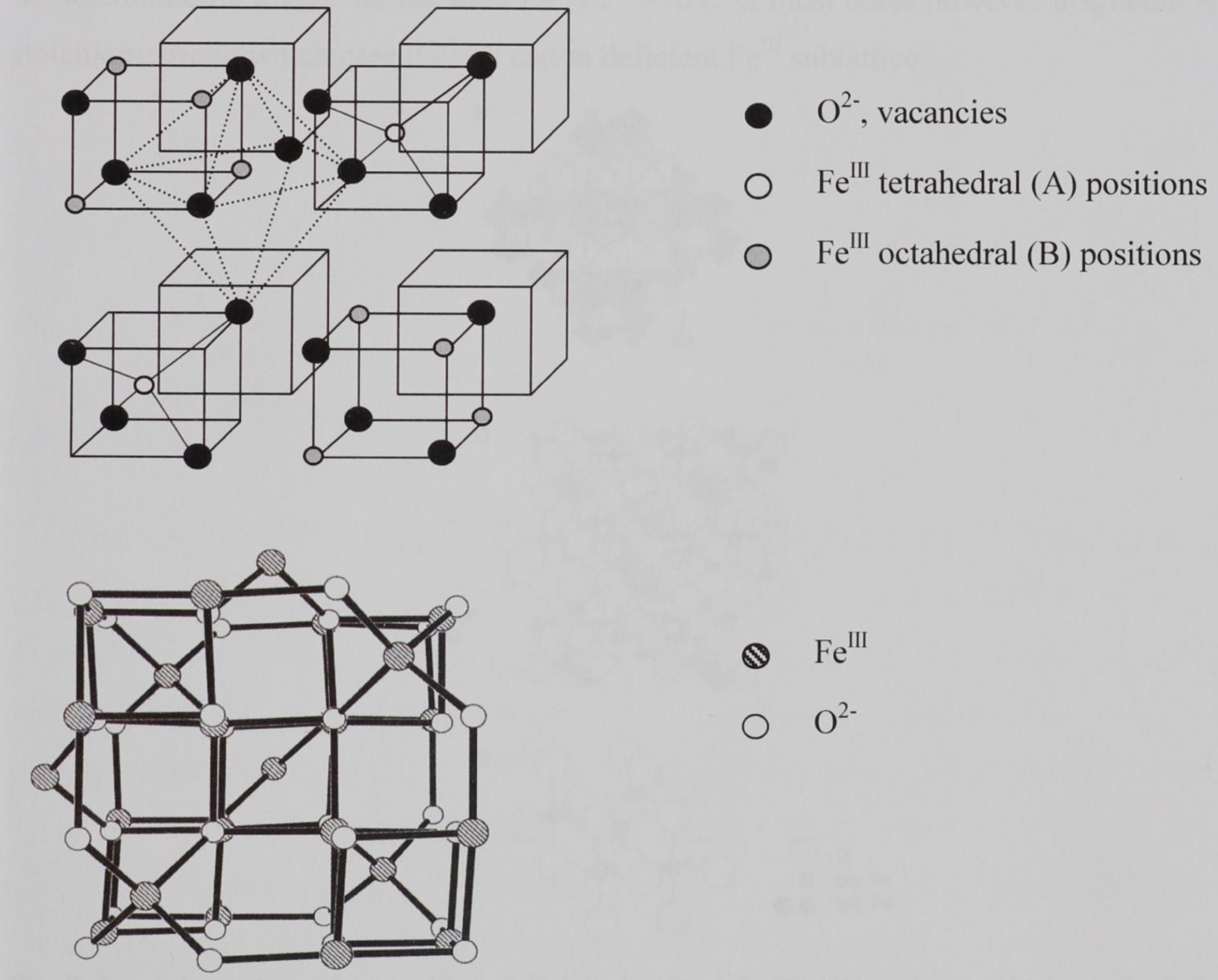

Fig. 2. a) Different positions of Fe^{III} cations in the maghemite structure. b) Ball-and-stick model of the structure. (100) plane view.

MAGNETITE (Fe_3O_4)

The colour of magnetite is black. It is an important Fe ore that is responsible for the magnetic properties of rocks. It is also formed in various organisms in which it serves as an orientation aid.

The structure of magnetite is as in the case of maghemite that of an inverse spinel. This structural similarity causes that maghemite and magnetite are almost indistinguishable by the means of XRD. Magnetite has a face-centered cubic cell (fcc) of $a = 0.839$ nm containing 32 O^{2-} anions which are regularly cubic close packed along the [111]. There are eight formula units per unit cell.

Magnetite differs from the majority of other iron oxides in that it contains iron in both divalent and trivalent oxidation states. Its formula can be written as $Y[XY]O_4$ where X stands for Fe^{II}, Y for Fe^{III} and the brackets stand for octahedral sites. Eight tetrahedral sites are distributed between Fe^{II} and Fe^{III}, i.e. the trivalent cations occupy both tetrahedral and octahedral sites. The structure consists of octahedral and mixed tetrahedral/octahedral layers stacked along [111].

In stoichiometric magnetite the ratio $Fe^{II}/Fe^{III} = 1/2$. In most cases however magnetite is non-stoichiometric in which case it has a cation deficient Fe^{III} sublattice.

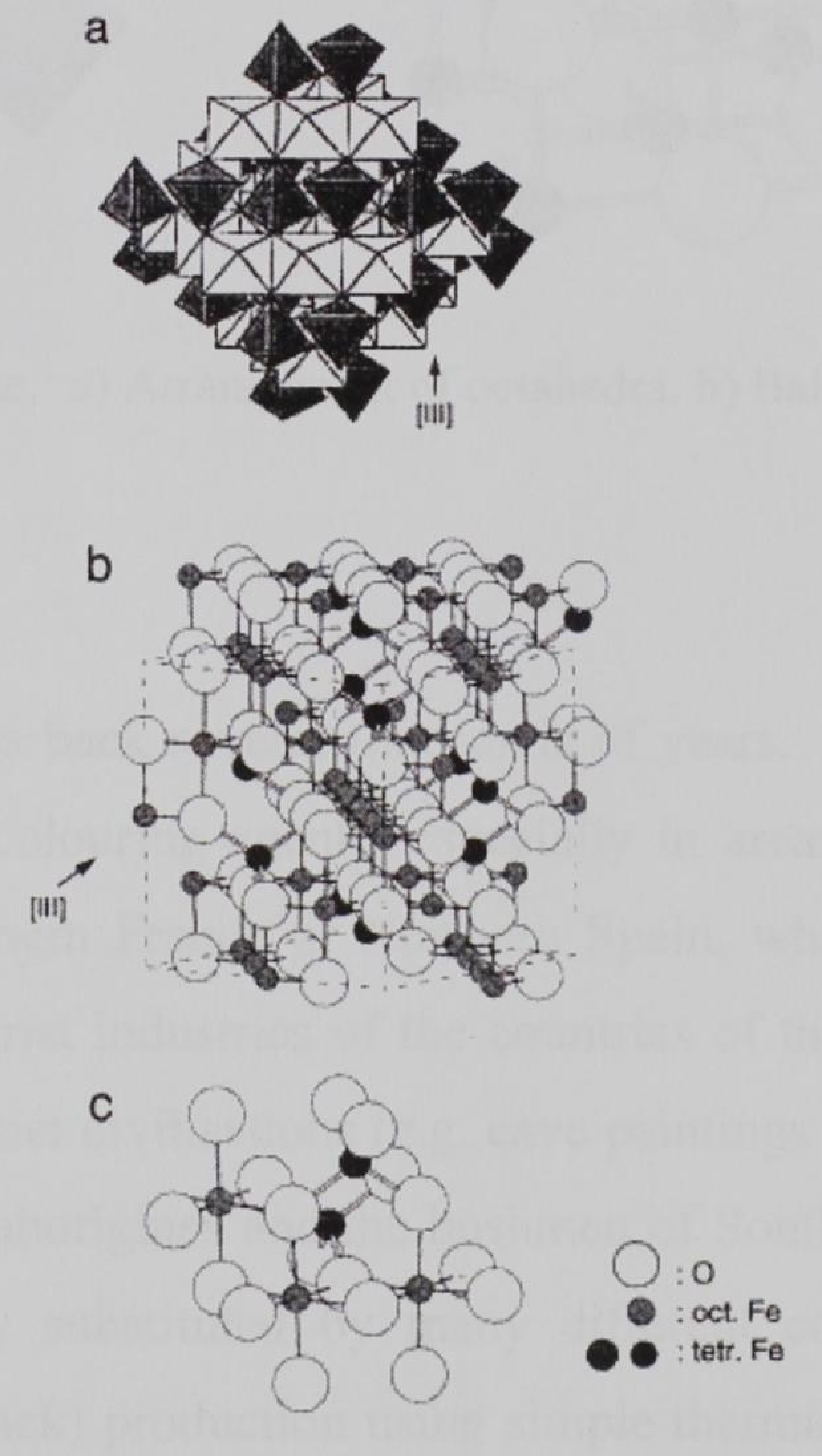

Fig. 3. Crystal structure of magnetite.[1] a) Polyhedral model with alternating octahedra and tetrahedral-octahedra layers. b) Ball-and-stick model. Unit cell outlined. c) Ball-and-stick model of the arrangement of octahedra and tetrahedra.

WÜSTITE ($Fe_{1-x}O$)

The stoichiometric wüstite (FeO) does not exist as a stable phase at pressures below 10 MPa. Under common pressures it is therefore more correct to use the non-stoichiometric formula $Fe_{1-x}O$ in which a proportion of the Fe ions are oxidized. Such a cation-deficient phase with $1- x$ ranging within 0.83–0.95 already exists at 0.1 MPa at temperatures higher than 567 °C. Below this temperature $Fe_{1-x}O$ disproportionates to Fe and Fe_3O_4. At 567 °C the equilibrium curves $Fe/Fe_{1-x}O$ and $Fe_{1-x}O/Fe_3O_4$ intersect. In the case, however, the non-stoichiometric $Fe_{1-x}O$ is rapidly quenched from the equilibrium region; it can stabilize as a metastable phase at room temperature.

FeO has a defective NaCl structure. It consists of two interpenetrating fcc structures of Fe^{II} and O^{2-}, there are four formula units in the cubic unit cell. Depending on the vacancy content, the lattice parameter a ranges within 0.428–0.431 nm. Most of the Fe cations are situated in octahedral interstices with a small proportion of Fe^{III} on the usually vacant tetrahedral sites.

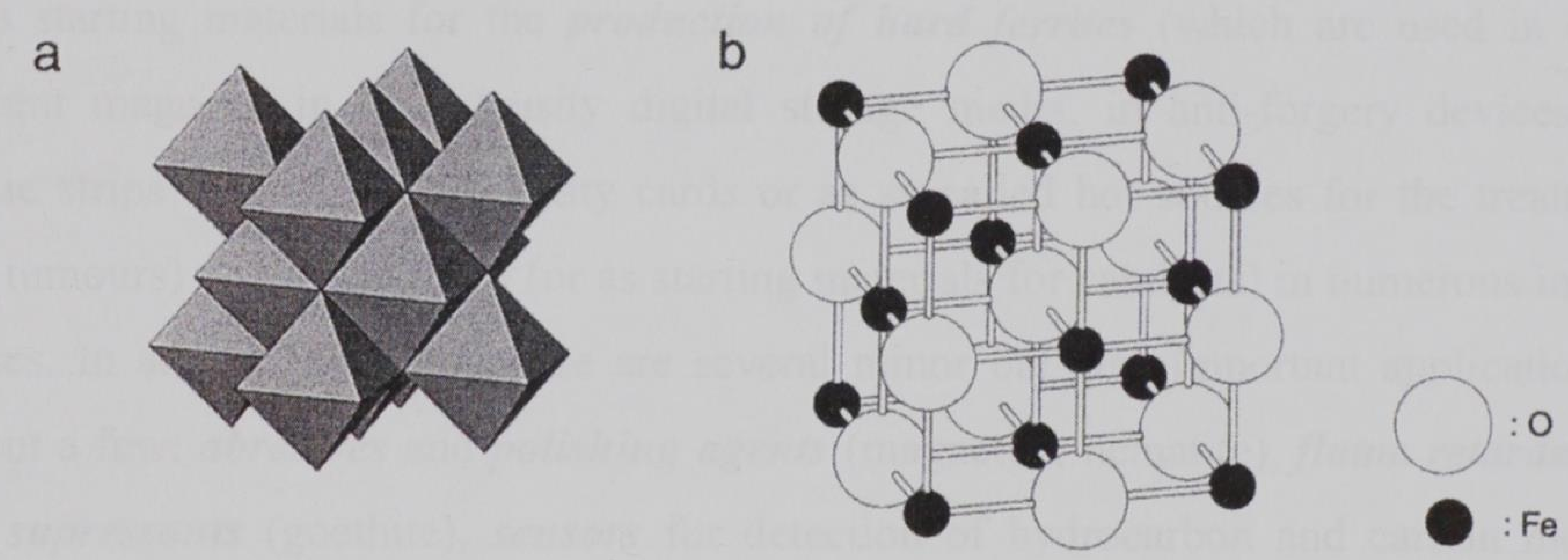

Fig. 4. Crystal structure of wüstite.[1] a) Arrangement of octahedra. b) Ball-and-stick model.

1.2 APPLICATIONS

The usage of iron oxides dates back several thousands of years. In the very beginning they were predominantly used as colouring agents, especially in areas as Sahara region, central Australia, South Africa, Southern France or Northern Spain, where suitable ochre deposits were available. Nowadays tourist industries of the countries of these regions profit from the iron oxide deposits left by former civilisations (e.g. cave paintings at Lescaux and Altamira or the rock art of the Australian aborigines and the bushmen of South Africa). In later years the raw materials were gradually substituted by many different colour pigments (especially hematite red and magnetite black) production using simple thermal conversions of accessible minerals. In antiquity raw and thermally treated ochres provided colours for decoration of pottery. In addition to natural colour pigments iron oxides were used for example in cosmetics production or in navigation, when magnetite in the form of lodestone was used in first compasses.[1]

In the course of time, however, with extensive progress in technology, the use of iron oxides was not solely focused on pigments anymore but became far more sophisticated and thus many more interesting applications were observed. After the discovery of the possibility to smelt them, mankind started to produce iron, which proved to be the base material for making weapons, utensils, tools, constructions, etc.

The most important contemporary applications of iron oxides are as ores for the ***iron*** and ***steel making***, as natural or synthetic ***colour pigments*** (for colouring concrete, asphalt, tiles, bricks, ceramics, glass, porcelain, rubber, paper, plastics, etc.), especially maghemite and magnetite are used as ***magnetic pigments*** in electronic recording and information storage media (audio and videotapes) or are added into inks and toners of printers and faxes. Iron oxides are often used as starting materials for the ***production of hard ferrites*** (which are used in ceramic permanent magnets, in high-density digital storage media, in anti-forgery devices in the magnetic strips of credit and identity cards or as so-called hot sources for the treatment of certain tumours) and as ***catalysts*** (or as starting materials for catalysts) in numerous industrial syntheses. In addition to them there are several minor but also important applications – to name but a few: ***abrasives*** and ***polishing agents*** (magnetite, hematite), ***flame retardants*** and ***smoke supressants*** (goethite), ***sensors*** for detection of hydrocarbon and carbon monoxide (hematite), airbags in automobiles contain hematite that serves as a ***catalyst*** for rapid release of nitrogen which inflates the bags, ***adsorbents*** for water and gas purification, low-level ***radioactive waste decontamination*** (by coprecipitation of radionuclides with ferric oxides at pH > 10), removal of sulphur from coal gas (FeOOH), production of ***photochemicals*** or ***fertilizers***, ***animal feeds***, etc.[1–4]

1.3 NANOPARTICLES

In recent years a rapt attention has been focused on the study of structure and properties of particles with dimensions units–tens nanometers, which are commonly called ***nanoparticles*** (i.e. an overall name for nanopowders, nanocomposites, core-shell particles or colloidal particles). Decreasing particle dimension causes a rise of a ratio *surface : volume* of a particle and at a particular size the surface effects fully prevail. Electrical, magnetic, optical and mechanical properties of nanoparticles are completely different from those of the *bulk* (high-volume) particles. Such an advantageous combination of small dimensions with unique properties is efficiently used in the development of new ***electronic*** and ***optical devices***, ***high storage media*** or ***ferrofluid techniques*** (i.e. magnetic fluids that contain nanometre-sized magnetic iron oxide particles in aqueous or organic media). The biggest advantage of iron oxides nanoparticles in comparison with the commonly used ultrafine metal particles (Fe, Co, Ni) is their chemical stability, which predestine their use in many ***medical applications***. They are successfully used as e.g. contrast agents, drug-delivery agents or for destruction of certain tumours (hyperthermia).[4]

1.3.1 ***METHODS OF SYNTHESES***

Due to the increasing number of applications of Fe_2O_3 nanoparticles, the novel methods for their synthesis have been developed in the past few years. Wang *et al.* obtained pure γ-Fe_2O_3 nanoparticles by ***laser ablation*** of Fe wire.[5] Zhou *et al.* prepared γ-Fe_2O_3 nanoparticles by ***hydrothermal chemical vapour deposition***.[6] Deshpande *et al.* used ***aqueous combustion*** synthesis technique. The method is based on a self-sustained reaction between an oxidizer (e.g., metal nitrate) and a fuel (e.g., glycine or hydrazine). Using this approach, spherical, nanoscale (6–10 nm) iron oxide particles with excellent ferrimagnetic properties were synthesized.[7] Makovec *et al.* synthesised magnetic maghemite nanoparticles with a narrow size distribution in ***water-CTAB-hexanol-butanol microemulsions***. The particle size was controlled with the composition of the microemulsion (water-to-CTAB ratio) and the temperature during synthesis.[8] Woo *et al.* synthesised nearly monodisperse, roughly spherical, and non-aggregated γ-Fe_2O_3 nanoparticles with average diameter of 5.5 nm by a ***sol-gel reaction*** of common ferric salt in reverse micelles and then crystallization of the gel particles by reflux.[9] Lee *et al.* prepared γ-Fe_2O_3 nanoparticles by a ***chemical coprecipitation technique*** of ferric and ferrous ions in alkali solution through the pipette drop method (pipette diameter: 2000 nm) and the piezoelectric nozzle method (nozzle size: 50 nm). The size distribution of the maghemite nanoparticles prepared by a typical pipette drop method was from 5 to 8 nm. However, the nanoparticles made by piezoelectric nozzle method exhibited a very narrow size distribution from 3 to 5 nm.[10] Popovici *et al.* synthesised monoliths of iron oxide-silica aerogel nanocomposites using a novel synthesis route which consisted of ***impregnating silica wet gels with anhydrous iron(II) precursors followed by ethanol supercritical drying of the gels***. The process yielded aerogels exhibiting high porosity, large surface areas (*ca.* 900 $m^2\ g^{-1}$), rather low densities (*ca.* 0.6 $g\ cm^{-3}$), and a homogeneous distribution of single-phase maghemite nanoparticles with average sizes ranging from 7 to 8 nm.[11] Kulikov *et al.* prepared fine-particle Fe_2O_3 via ***microwave processing*** of $Fe(NO_3)_3 \cdot nH_2O$, followed by a low temperature annealing. The particle size of the resulting γ-Fe_2O_3 was 5–6 nm after microwave processing and 80–110 nm after subsequent low-temperature heat treatment.[12] Janot *et al.* directly synthesised maghemite nanoparticles by ***ball milling*** of an iron powder within water for different duration using a planetary ball mill equipped with stainless steel vials. The *in-situ* production of hydrogen hindered the hematite formation during grinding. Particles of about 15 nanometres were obtained after 48 hrs of milling.[13] Hyeon *et al.* used the ***high-temperature (300 °C) aging*** of iron-oleic acid metal complex, which was prepared by the thermal decomposition of iron pentacarbonyl in the presence of oleic acid at 100 °C, for the synthesis of monodisperse iron nanoparticles. As-prepared Fe nanoparticles were consequently transformed to monodisperse γ-Fe_2O_3 nanocrystallites by controlled oxidation by using trimethylamine oxide as a mild oxidant. Particle size was varied from 4 to 16 nm by controlling the experimental parameters.[14] Veintemillas-Verdaguer *et al.* synthesised pure γ-Fe_2O_3 particles by a continuous wave ***CO_2 laser-induced pyrolysis*** of iron pentacarbonyl vapour in an oxidizing atmosphere.[15] Pascal *et al.* carried out the ***electrochemical synthesis*** of γ-Fe_2O_3 nanoparticles in an organic medium. The size was directly controlled by the imposed current density and the resulting particles were stabilized as a colloidal suspension by the use of cationic surfactants. The size distributions of the particles were narrow, with the average sizes varying from 3 to 8 nm.[16]

Thermally induced transformations of iron bearing salts and minerals represent another way of synthesis of nanoparticles. Compared with several of above mentioned routes of syntheses, the solid-state reactions have many indisputable advantages. They are experimentally and cost effective, allow to prepare a relatively huge amount of material, moreover without a matrix, which significantly enhances its applicability, enable to synthesise also rare forms of β- and ε-Fe_2O_3 polymorphs respectively[2,17] in addition to more common α- and γ-Fe_2O_3 nanoparticles,[18–20] or allow to controll the particle size and chemical composition of the product through the particle size of the precursor,[21–24] etc.

The syntheses directly aimed at a particular structural form of Fe_2O_3 (alpha, beta, gamma or epsilon) with appropriate properties, however, demand full comprehension of all possible factors, which may influence the course of the solid-state reactions. Decomposition temperature and time and reaction atmosphere belong to the commonly known ones. It has been recently proved that the ***sample weight*** and the ***gases evolving during the***

decomposition could represent another group of significant conditions, which have not been adequately studied yet and therefore are difficult to comprehend.

This work is aimed at a study of the influence of the participation of evolving gases and the sample mass on the thermally induced decomposition of ferrous oxalate dihydrate ($FeC_2O_4{\cdot}2H_2O$) as a typical representative of metal oxalates, which are commonly employed in solid-state chemistry as precursors for thermally induced syntheses of various nanocrystalline metal oxides.

2 FUNDAMENTALS OF MÖSSBAUER SPECTROSCOPY

As Mössbauer spectroscopy is a leading method used for the identification of various iron-bearing compounds in this study and with keeping in mind that this unique method is not as commonly widespread as for example XRD, the basic principles and parameters of Mössbauer spectra are briefly discussed in the following sections.

2.1 THEORY OF THE MÖSSBAUER EFFECT

Mössbauer spectroscopy is based on the Mössbauer effect – the resonant recoilless emission and absorption of the gamma rays by an atomic nucleus. The probability of the Mössbauer effect can be expressed as:[25]

$$f = \exp\left[\frac{-6R}{k_B\theta_D}\left\{\frac{1}{4}+\left(\frac{T}{\theta_D}\right)^2\int_0^{\theta_D/T}\frac{x\,dx}{e^x-1}\right\}\right], \tag{1}$$

where R is the recoil energy (a constant for a particular nucleus which can be evaluated as: $E_\gamma^2/2Mc^2$, where E_γ is the energy of the gamma ray, M is the mass of emitting nucleus and c is the velocity of light), k_B Boltzmann constant, θ_D Debye temperature (characterizing the strength of the atomic bonding) and T stands for the measurement temperature. One can easily visualize that the maximum value of f can be obtained for T = 0 K and the minimum value of the ratio R/θ_D. This requirement drastically reduces the amount of usable energies E_γ (which appears in the equation for R squared) and sets the maximum value $E_\gamma \approx 100$ keV (for spectra recorded in transmission geometry). This represents severe limitation since a large proportion of gamma-ray energies lies in the MeV energy region. In addition, another restriction is denoted by the fact that these low E_γ values have to represent only transitions to the ground energy state otherwise could not be absorbed. There are only eight Mössbauer transitions fulfilling these restrictions that can be successfully run at room temperature (RT). Among them a transition in ^{57}Fe with E_γ = 14.4 keV that allows studying Fe-containing materials by the means of Mössbauer spectroscopy also appears.

2.2 EXPERIMENTAL OBSERVATION OF THE MÖSSBAUER EFFECT

The non-zero value of the probability of the Mössbauer effect discussed in the previous section represents only one of the conditions necessary for its successful observation. Another important condition is the identity of the energy states of the Mössbauer nuclei of the source and the absorber. This identity is obviously broken if the source and the absorber are either different chemical compounds, or if they are exposed to different magnetic fields or temperatures. In this case emission and absorption spectral lines do not overlay and Mössbauer spectrum cannot be obtained.

Compensation of such a difference is achieved by the change of the energy of either the emitted or the absorbed gamma-ray photon. This is made by the relative movement of the source against the absorber (or *vice versa*) with the velocity v resulting in the Doppler energy shift that modulates the transition energy E_γ. In the case of ^{57}Fe sufficient values of v are in the units of mm s^{-1}. The drawing of the experimental arrangement used for the measurement of ^{57}Fe Mössbauer spectra in transmission geometry is given in Fig. 5.

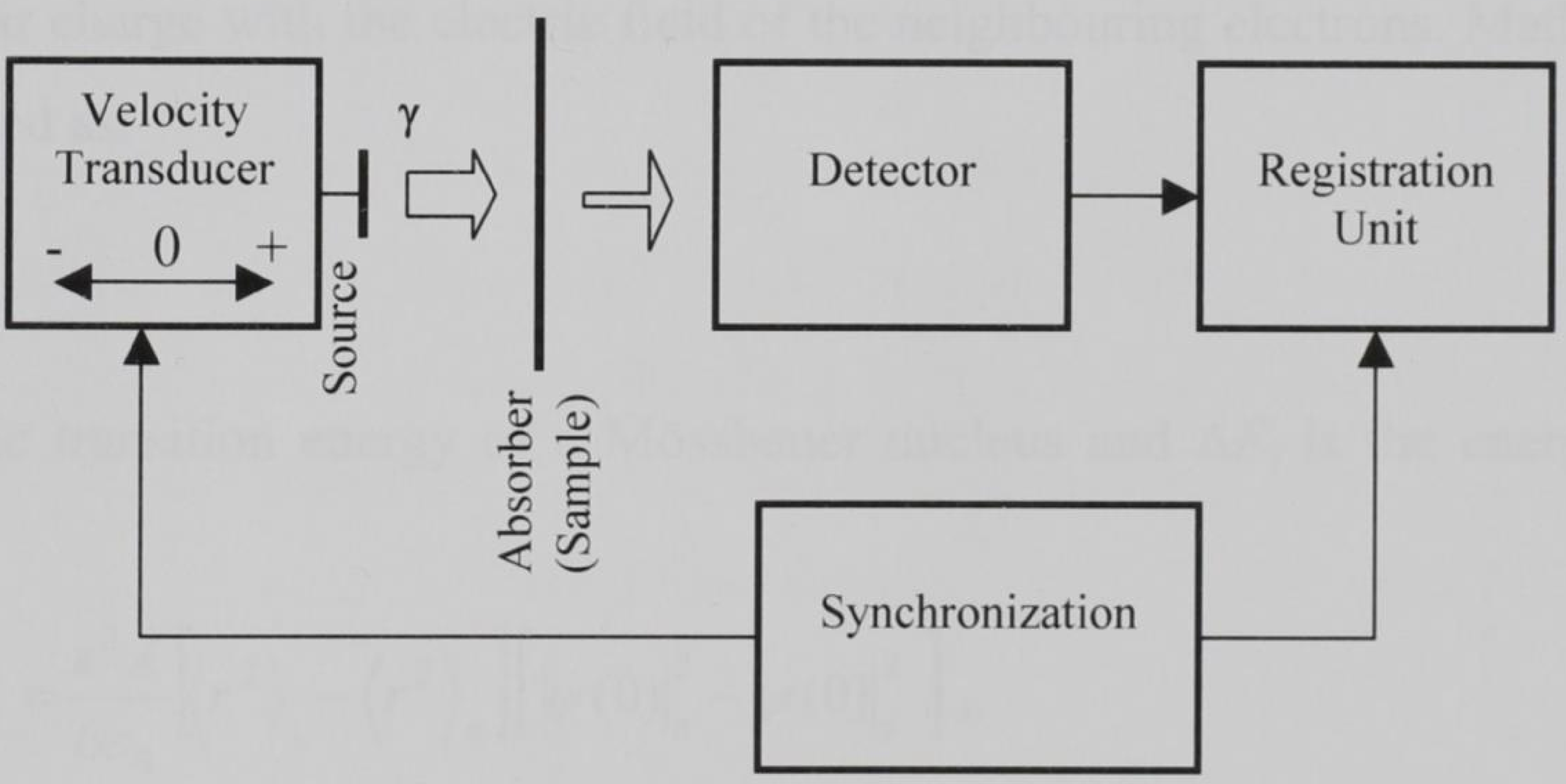

Fig. 5. Experimental arrangement of a Mössbauer spectrometer in transmission geometry.

The intensity of the γ-ray photons passing through the absorber depends on the velocity of the relative source-absorber movement and is registered by a detector. This dependence is called Mössbauer spectrum in which the minima correspond to the resonant absorption of γ photons. The magnitude of the resonant absorption is usually expressed as:

$$\varepsilon(v) = \frac{I(\infty) - I(v)}{I(\infty)}, \tag{2}$$

where $I(v)$ is the intensity of γ-ray photons which pass through the absorber at the relative velocity v, and $I(\infty)$ is the intensity of γ-rays passing through the absorber out of the resonance.

2.3 HYPERFINE INTERACTIONS

As the hyperfine interactions in Mössbauer spectroscopy are regarded the electromagnetic interactions of the nucleus with neighbouring electrons and ions which cause changes in atomic and nuclear energy levels. From the viewpoint of the parameters of measured Mössbauer spectra there are three important types of them: electric monopole interaction resulting in ***isomer shift***, electric quadrupole interaction resulting in so-called ***quadrupole splitting (shift)*** and magnetic dipole interaction resulting in ***magnetic splitting*** of the measured spectra.

ISOMER (CHEMICAL) SHIFT δ

Isomer shift of the spectral lines arises as a consequence of the mutual interaction of the positive nuclear charge with the electric field of the neighbouring electrons. Mathematically it can be expressed as:

$$\delta = \frac{c\,\Delta E_\gamma}{E_\mathrm{t}}, \tag{3}$$

where E_t is the transition energy of a Mössbauer nucleus and ΔE_γ is the energy difference expressed by:

$$\Delta E_\gamma = E_\gamma^\mathrm{a} - E_\gamma^\mathrm{s} = \frac{e^2 Z}{6\varepsilon_0}\left[\langle r^2\rangle_1 - \langle r^2\rangle_0\right]\left[|\psi(0)|_\mathrm{a}^2 - |\psi(0)|_\mathrm{s}^2\right], \tag{4}$$

where E_γ^a and E_γ^s are nuclear transition energies in the absorber and the source respectively, Z atomic number, e electron charge, ε_0 permittivity of vacuum, $\langle r^2\rangle_1$ and $\langle r^2\rangle_0$ are mean square radii of the nuclei in excited and ground energy states respectively, $|\psi(0)|_\mathrm{a}^2$ and $|\psi(0)|_\mathrm{s}^2$ are electron densities in the absorber and the source respectively.

Provided the source and the absorber are chemically identical and/or are exposed to the same conditions (external magnetic field, temperature) the emission and absorption lines overlap and $\delta = 0$ mm s^{-1}. In the opposite case $\Delta E_\gamma \neq 0$ that results in a non-zero value of δ and the centre of a Mössbauer spectrum is shifted. An example of the origin of isomer shift is given in Fig. 6.

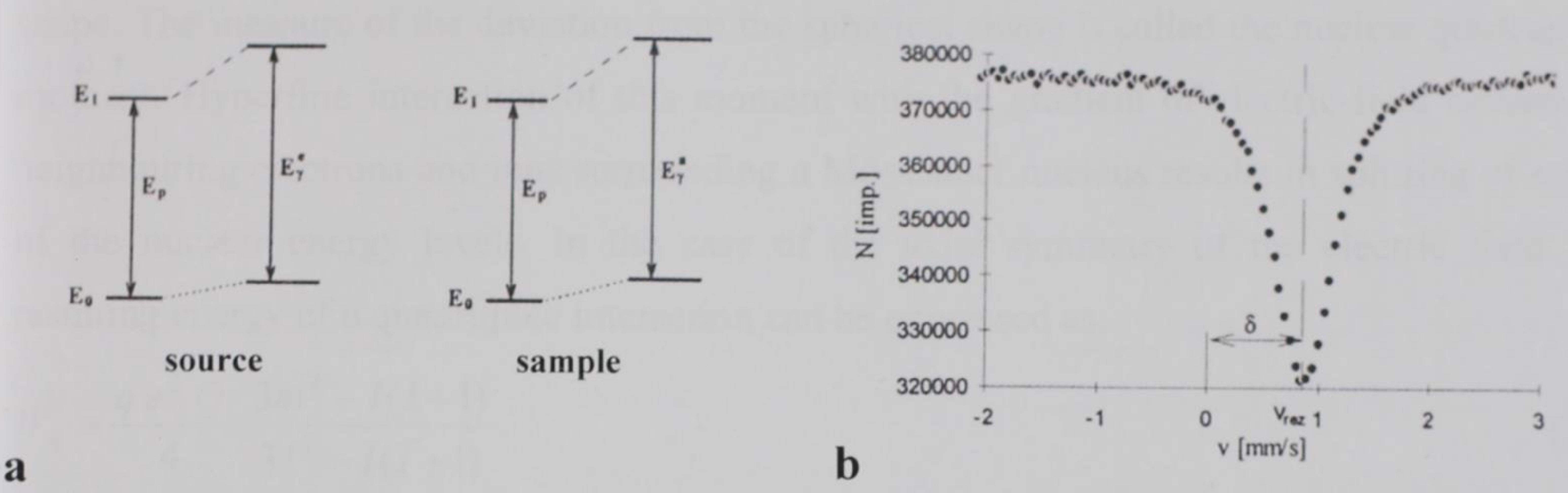

Fig. 6. The change of the nuclei energy levels in a source and a sample during the electric monopole interaction (a) resulting in the isomer shift of a Mössbauer spectrum (b).

Isomer shift provides information about the oxidation state, coordination number, ligand-type coordinated to iron cations and the spin state of iron atoms in a compound. The obtained value of isomer shift strongly depends on a calibration standard (α-Fe, α-Fe_2O_3, etc.) in which the mid-point of the individual spectrum is measured for the zero velocity. At room temperature Fe^{III} in a crystalline lattice gives values of δ (relative to α-Fe) within 0.20–0.50 mm s^{-1}, in minerals within 0.35–0.50 mm s^{-1} for octahedral and 0.17–0.30 mm s^{-1} for tetrahedral coordination respectively.[26] High-spin Fe^{II} gives values of isomer shift usually above 0.5 mm s^{-1}.

It is also necessary to keep in mind that the observed values of δ strongly depend on the measurement temperature (i.e. the temperature to which a sample is subjected) the change of which is accompanied by the so-called thermal shift: the lower the measurement temperature with respect to RT, the higher the value of the thermal shift and *vice versa* (measurement temperatures of 600, 78 and 4 K result to the thermal shifts of –0.22, +0.12 and +0.14 mm s^{-1}).[25]

QUADRUPOLE SPLITTING ΔE_Q, QUADRUPOLE SHIFT ε_Q

Any nucleus with an angular momentum *I* greater than ½ usually exhibits a non-spherical shape. The measure of the deviation from the spherical shape is called the nuclear quadrupole moment. Hyperfine interaction of this moment with the gradient of electric field caused by neighbouring electrons and ions surrounding a Mössbauer nucleus results in splitting of some of the nuclear energy levels. In the case of the axial symmetry of the electric field the resulting energy of a quadrupole interaction can be expressed as:

$$W_{\mathrm{q}} = \frac{q\,e^2\,Q}{4} \cdot \frac{3m^2 - I(I+1)}{3I^2 - I(I+1)}. \qquad (5)$$

The quantity *q* characterizes the external electric field gradient, *Q* stands for the nuclear quadrupole moment, *m* is magnetic quantum number and *I* represents nuclear spin. The quantity e^2qQ is so-called constant of hyperfine quadrupole splitting.

If the energy levels of the absorber are quadrupoly split and the energy levels of the source are not (or *vice versa*) the resulting Mössbauer spectrum consists of a doublet. An example for the nucleus of ^{57}Fe (in which the spins of the ground and excited state are I = 1/2 and I = 3/2 respectively) is given in Fig. 7.

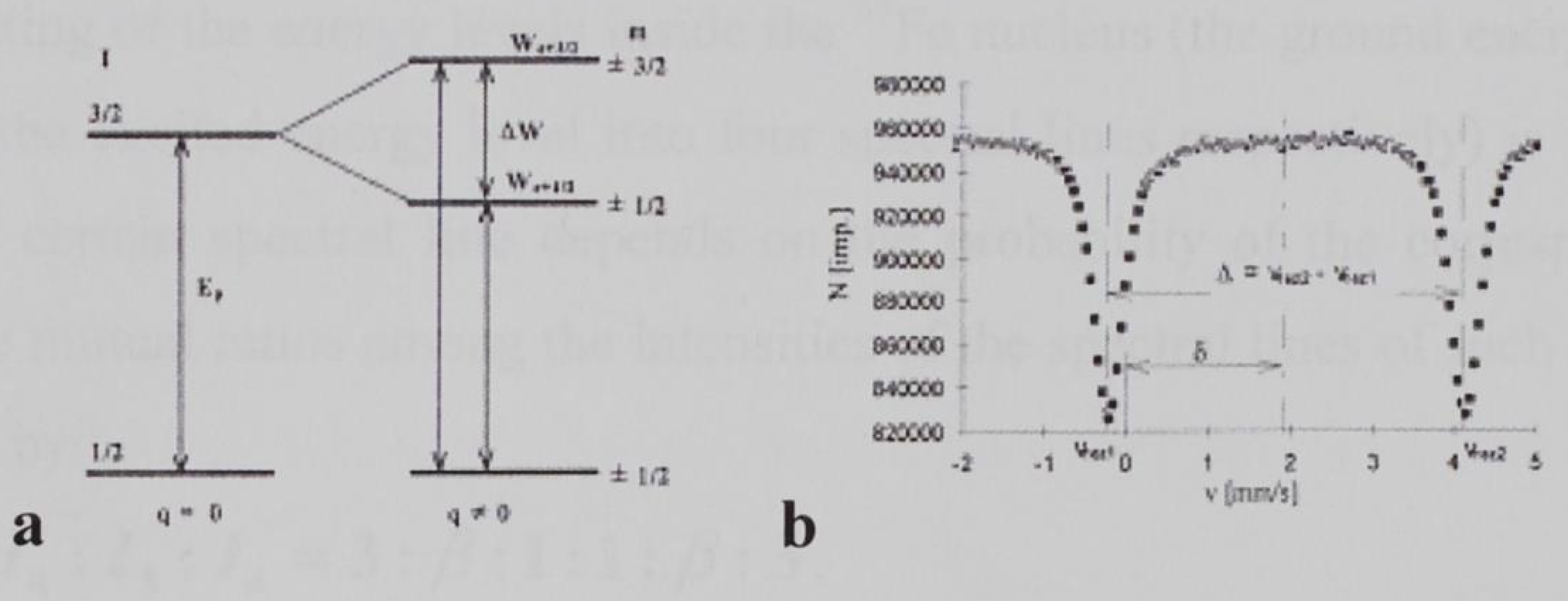

Fig. 7. The splitting of the excited energy level in the ^{57}Fe nucleus (a) resulting in the hyperfine quadrupole splitting of a Mössbauer spectrum (b).

In accordance with eqn (5) experimentally obtained value of quadrupole splitting for ^{57}Fe can be expressed as the velocity difference between the spectrum lines (Fig. 7b):

$$\Delta E_{\mathrm{Q}} = \frac{\Delta W_q \cdot c}{E_\gamma}. \qquad (6)$$

Quadrupole splitting provides information about the degree of the site distortion: ΔE_{Q} of Fe$^{\mathrm{III}}$ in iron oxides is a measure of distortion of Fe$^{\mathrm{III}}$–O polyhedra. It ranges from 0 (in the case of an ideal cubic symmetry) up to *ca.* 1.5 mm s^{-1}. Fe$^{\mathrm{II}}$ normally gives values $\Delta E_{\mathrm{Q}} > 2$ mm s^{-1}.[26]

In the case of magnetically split samples (see following section) there appears a combined effect inside the nucleus – quadrupole splitting of the excited energy level is accompanied by the simultaneous levels' shift and it is convenient to use the term quadrupole shift (ε_Q) instead of above discussed quadrupole splitting.

MAGNETIC HYPERFINE FIELD B_{HF} (H)

Magnetic dipole splitting (nuclear Zeeman effect) arises as a consequence of the interaction between a non-zero magnetic dipole moment μ of a nucleus in an energy state W_μ and a time-constant magnetic field $\vec{B}_{\text{total}}$ (a vector sum of the hyperfine field $\vec{B}_{\text{hf}}$ and any applied field). This hyperfine interaction causes the change of the energy of a nuclear state:

$$\Delta W_\mu = -(\vec{\mu}\,\vec{B}_{\text{total}}) = -\frac{\mu}{I} m\, B_{\text{total}}, \tag{7}$$

where I is a spin in a certain energy state and m stands for magnetic quantum number exhibiting $2I+1$ values. The number of spectral lines is given by the number of energy states subdued to the magnetic field restricted simultaneously by the selective rules – only those energy transitions fulfilling the condition $\Delta m = 0, \pm 1$ are allowed. The example of such a magnetic splitting of the energy levels inside the ^{57}Fe nucleus (the ground energy level is split into two and the excited energy level into four spectral lines respectively) is in Fig. 8a. The intensity of a certain spectral line depends on the probability of the corresponding energy transition. The mutual ratios among the intensities of the spectral lines of such a sextet (left to right) is given by:

$$\boldsymbol{I_1 : I_2 : I_3 : I_4 : I_5 : I_6 = 3 : \beta : 1 : 1 : \beta : 3}, \tag{8}$$

in which:

$$\beta = \frac{\mathbf{4\sin^2\theta}}{\mathbf{1+\cos^2\theta}}. \tag{9}$$

In eqn (9) θ is the angle between the direction of γ-ray photons and the direction of the magnetic field. One can easily visualize that in the case $\theta = 0°$ the second and the fifth line of the spectrum disappear. It is however worth mentioning that the full disappearance of the second and fifth lines strongly depends on the degree of crystallinity of a sample. In the case of perpendicular experimental geometry ($\theta = \pi/2$) the resulting value of the intensities of the questioned lines is $\beta = 4$. When the magnetic domains in the crystal are orientated chaotically (polycrystalline samples), $\langle \cos^2 \theta \rangle = 1/3$ and $\langle \sin^2 \theta \rangle = 2/3$ and the ratio among the intensities is 3:2:1:1:2:3 as apparently shown in Fig. 8b.

Without an external magnetic field B_{ext} the total splitting across the spectrum (the distance in mm s^{-1} between the first and the sixth spectrum line) is determined by the magnitude of the hyperfine field B_{hf}, which arises as a sum of four contributions:

$$B_{\text{hf}} = B_{\text{c}} + B_{\text{sn}} + B_{\text{ln}} + B_{\text{ce}}, \tag{10}$$

where B_{c} is the so-called Fermi contact term arising as a consequence of the interaction between the magnetic moment of *s* electrons with the nuclear magnetic moment, the next two terms B_{sn} and B_{ln} represent contributions from the dipole-dipole interaction of the spin and orbit parts of the electron magnetic moment with the nuclear magnetic moment. The final term, B_{ce} arises as a contribution of conduction electrons.

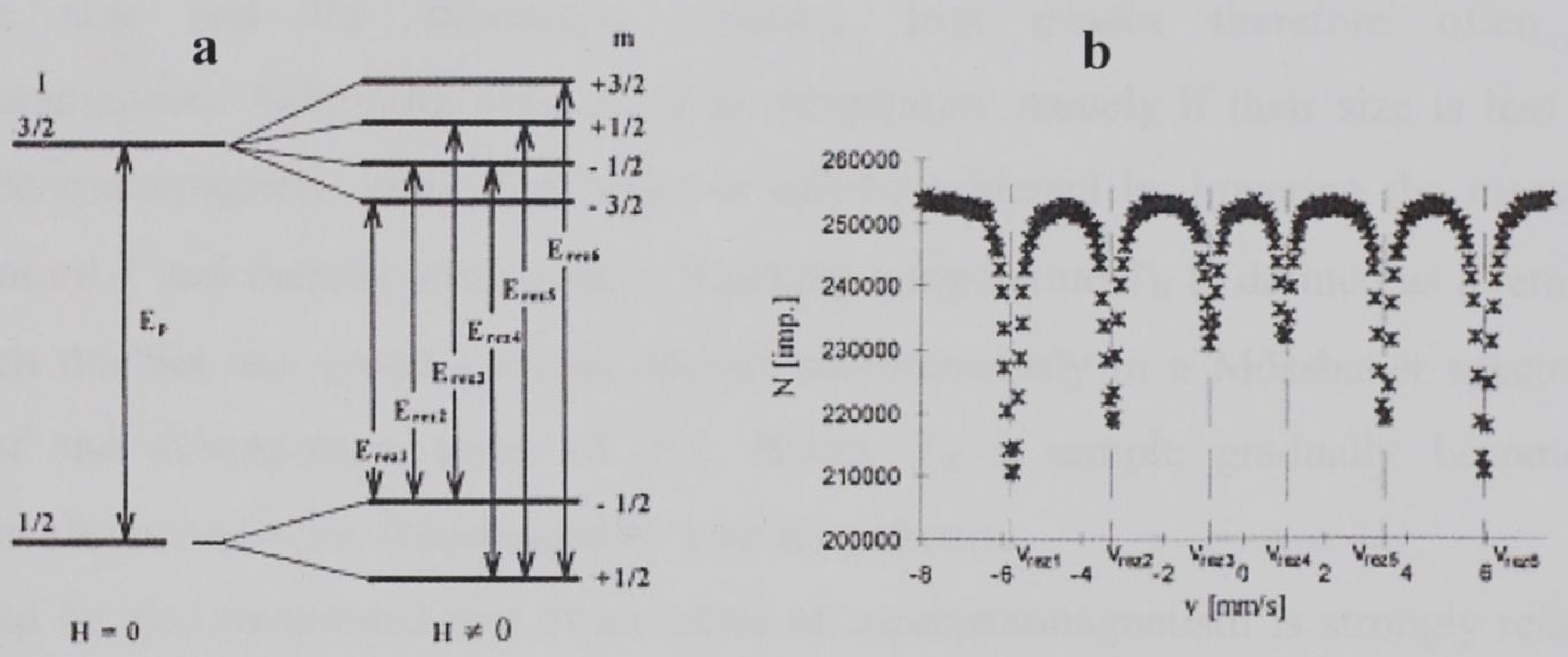

Fig. 8. The splitting of the ground and excited ^{57}Fe nucleus energy levels as a result of the magnetic dipole interaction (a) and corresponding Mössbauer spectrum (b).

The magnitude of magnetic hyperfine field B_{hf} provides information about the valence and magnetic properties of the compounds. Since the latter are also temperature dependent, Mössbauer spectra are often recorded at different temperatures.

In the following text hyperfine magnetic field is marked as *H* as it is conventional in practical use.

2.4 SUPERPARAMAGNETISM

Superparamagnetism is an effect strongly connected to the particle size. The energy required to reverse the magnetization of a particle depends directly on its volume and can be regarded as an activation energy barrier of height $K_e V$, in which K_e represents the effective magnetic anisotropy constant (as a consequence of magnetic anisotropy there exist preferred crystallographic directions along which the electron spins are most readily aligned and the substance most easily magnetized) and V is the particle volume. If sufficient energy is supplied, magnetisation can be reversed in the relaxation time τ that can be expressed as:

$$\tau \approx \exp\left(\frac{K_e V}{k_B T}\right). \tag{11}$$

As the volume V decreases, the energy barrier becomes comparable with the thermal energy $k_B T$. Superparamagnetic relaxation occurs precisely at the moment when the thermal energy exceeds the activation energy barrier between the spin states and as a consequence the spins start to fluctuate spontaneously. As a result the observed magnetic field is reduced or even absent (Mössbauer spectrum of such a sample is represented by a doublet).

It is obvious from the eqn (11) that the superparamagnetic effect depends directly on the particle size and the anisotropy constant. Iron oxides therefore often display superparamagnetic behaviour even at room temperature namely if their size is less than 10 nm. Superparamagnetic relaxation however can be achieved by lowering the measurement temperature T and thereby increasing τ. Blocking temperature T_B is defined as a temperature at which doublet and sextet patterns coexist simultaneously in a Mössbauer spectrum in a ratio of the subspectrum areas of 1:1. Below T_B a sample gradually becomes fully magnetically ordered (i.e. represented by a sextet pattern).

It should be also mentioned that observation of superparamagnetism is strongly related to a characteristic time of a used measuring method.

2.5 MÖSSBAUER SPECTROSCOPY OF IRON OXIDES

HEMATITE

α-Fe_2O_3 is thermally the most stable compound of all four existing polymorphs of Fe_2O_3. From the viewpoint of the magnetic properties, hematite shows complex behaviour within the temperature scale. At room temperature (RT) the Fe^{III} spins are aligned close to the (001) plane but slightly canted (~ 7°) which causes weakly ferromagnetic behaviour. RT Mössbauer spectrum consists of a sextet with hyperfine parameters $\delta = 0.37$ mm s^{-1}, $\varepsilon_Q = -0.21$ mm s^{-1} and $H = 51.8$ T. Below the so-called Morin transition temperature T_M (263 K for bulk particles) the spins of Fe^{III} are exactly antiparallel and hematite is antiferromagnetic. T_M decreases linearly with $1/d$ (d being the particle size) down to *ca.* 200 K for a crystal with a diameter about few tens of nm. This relationship is however strongly dependent upon the way hematite is synthesized.[1] The Morin transition is accompanied by the change of the hyperfine parameters: $\delta = 0.49$ mm s^{-1}, $\varepsilon_Q = +0.41$ mm s^{-1} and $H = 54.2$ T.

Above the Nèel transition temperature $T_N = 955$ K, α-Fe_2O_3 becomes paramagnetic and the Mössbauer spectrum consists of a doublet with $\Delta E_Q = 0.46$ mm s^{-1}.

Mössbauer spectrum of superparamagnetic hematite (< 8 nm) exhibits a doublet pattern too but due to the small particle size the value of ΔE_Q is increased up to 1 mm s^{-1}.[1]

MAGHEMITE

There are two non-equivalent positions of Fe^{III} cations in γ-Fe_2O_3 structure. Antiparallel alignment of A (tetrahedral) and B (octahedral) sublattices and their different population causes ferrimagnetic behaviour.

According to the stoichiometric formula of maghemite (see Section 1.1) the contributions of A and B sites should be represented by two sextet subspectra in the overall RT Mössbauer spectrum in the ratio A:B = 3:5 (expressed by the ratio between the areas of corresponding Mössbauer subspectra). However the Fe^{III} oxidation state is not very sensitive to its environment and as a consequence RT Mössbauer spectrum consists of only one sextet as the A and B positions remain undistinguishable, with hyperfine parameters $\delta = 0.32$ mm s^{-1}, $\varepsilon_Q = 0$ (cubic symmetry) and $H \sim 50$ T. Both non-equivalent positions can be however distinguished by the application of external magnetic field in which case the A and B site fields make parallel and antiparallel alignment to it and the resultant fields are much better separated. This situation is well demonstrated in Fig. 9. Fig. 9a shows a Mössbauer spectrum of well-crystallized (almost complete disappearance of the second and fifth lines) maghemite at 4 K in external magnetic field of 6 T. Fig. 9b displays on the other hand a spectrum of maghemite that is apparently very small; in such a case there is no perfect alignment of the magnetic moments with the external magnetic field – there is canting among them resulting in the non-zero intensity in lines 2 and 5 of a sextet pattern. The canting depends on the particle size and decreases with the simultaneous increase of the particle size.

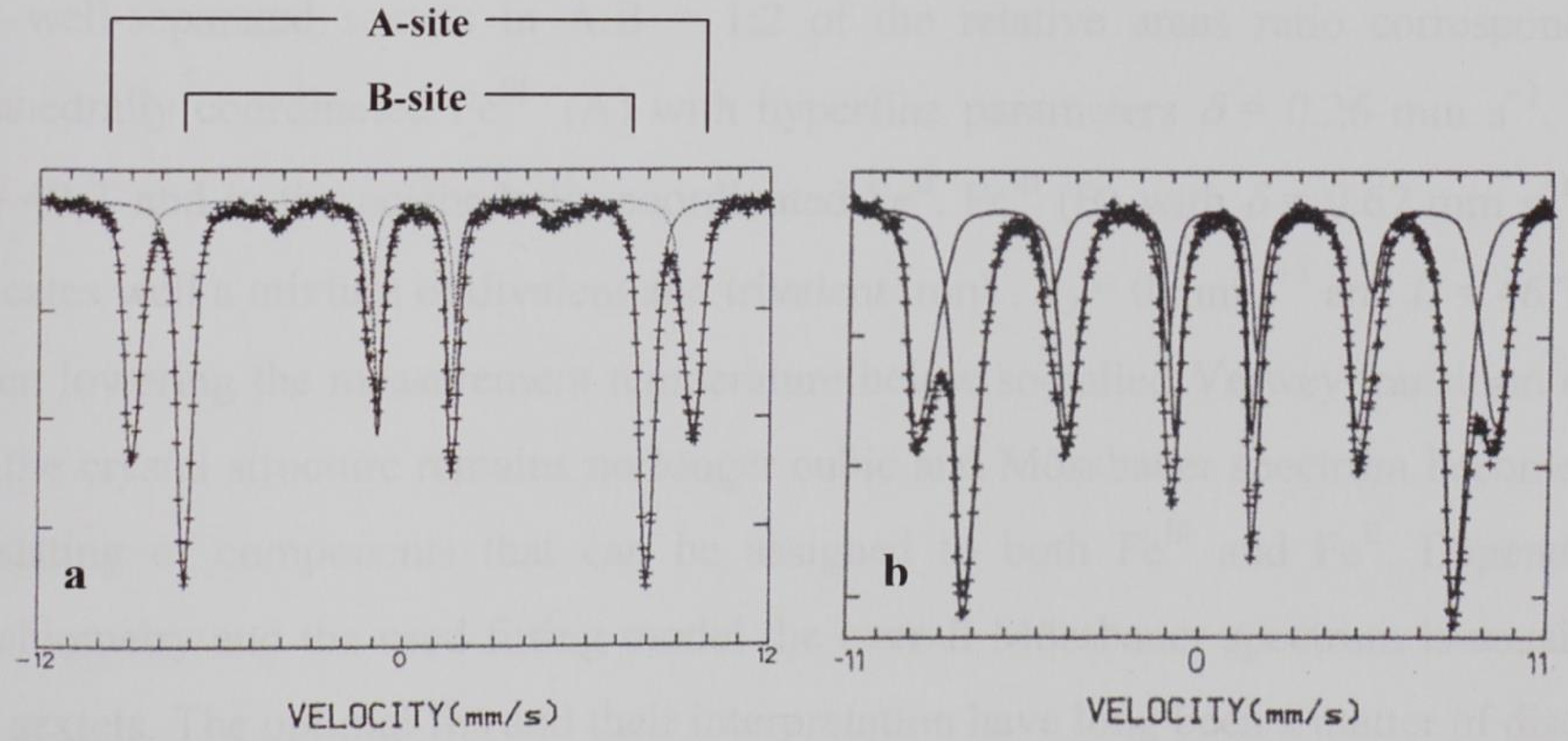

Fig. 9. Mössbauer spectra of a) well crystalline maghemite recorded at 4 K in external magnetic field of 6 T and b) of poorly crystalline maghemite recorded at 10 K in external magnetic field of 6 T.[27]

In the case of ultra small particles (< 10 nm) maghemite as well as hematite exhibit superparamagnetic behaviour and in such a case a doublet pattern is observed in RT Mössbauer spectrum. Lowering the measurement temperature leads to the obtaining of T_B (as already discussed in section Superparamagnetism) by the value of which the particle size can be determined indirectly – the lower T_B the smaller particles.

γ-Fe_2O_3 is thermally unstable and within the broad temperature interval about 370–600 °C maghemite transforms into hematite in air. The transformation temperature may quite differ depending predominantly on the origin and the size of the particles.[1] Due to the thermal instability precise determination of Curie temperature T_C of maghemite is almost unfeasible. However, on the ground of the results obtained by various experimental techniques it is reported to be about 850 K.

MAGNETITE

The structure of magnetite is similar to that of maghemite. There are two non-equivalent positions of Fe atoms in the structure but unlike in γ-Fe_2O_3 structure they are in both divalent and trivalent oxidation states. As well as hematite Fe_3O_4 exhibits threefold subdivision of magnetic properties within the temperature scale.

The unequal population of the A and B sites and antiparallel spin alignment leads as well as in maghemite to ferrimagnetic behaviour at RT. However, the two valence states in octahedral sites are not distinct and RT Mössbauer spectrum of stoichiometric magnetite consists of only two well-separated sextets in A:B = 1:2 of the relative areas ratio corresponding to the tetrahedrally coordinated Fe^{III} (A) with hyperfine parameters $\delta = 0.26$ mm s^{-1}, $\varepsilon_Q = 0$ and $H = 49$ T and to the octahedrally coordinated Fe^{II}, Fe^{III} (B) with $\delta = 0.67$ mm s^{-1} (this value indicates well a mixture of divalent and trivalent iron) , $\varepsilon_Q = 0$ mm s^{-1} and $H = 46$ T.

When lowering the measurement temperature below so-called Verwey transition temperature T_V, the crystal structure remains no longer cubic and Mössbauer spectrum becomes complex, consisting of components that can be assigned to both Fe^{III} and Fe^{II}. Depending on the stoichiometry and the used fitting model the overall Mössbauer spectrum is usually fitted by 3–9 sextets. The optimal fits and their interpretation have long been a matter of discussion and there does not exist a unified attitude.

It is becoming apparent that stoichiometry of Fe_3O_4 plays the most important role when interpreting its Mössbauer spectra as clearly demonstrated in Fig. 10. Fig. 10a shows a RT

Mössbauer spectrum of a near-stoichiometric magnetite (A:B $\cong$ 1:2) and Fig. 10b shows a Mössbauer spectrum of the same sample taken at 4.2 K (far below T_V) fitted with five sextets. Fig. 10c however exhibits a Mössbauer spectrum of a non-stoichiometric magnetite, as obvious from the broken ratio A:B, taken at 160 K. Under the applied longitudinal magnetic field (6 T), the unequal positions of Fe^{III}, Fe^{II} and Fe$^{III/II}$ become well resolved (Fig. 10d). Above T_C (~ 850 K) magnetite becomes paramagnetic and its Mössbauer spectrum consists of a singlet ($\delta \approx 0$ mm s^{-1}) and a doublet with the hyperfine parameters: $\delta \approx 0.22$ mm s^{-1} and $\Delta E_Q \approx 0.14$ mm s^{-1} that can be assigned to the A and B sites respectively.[25]

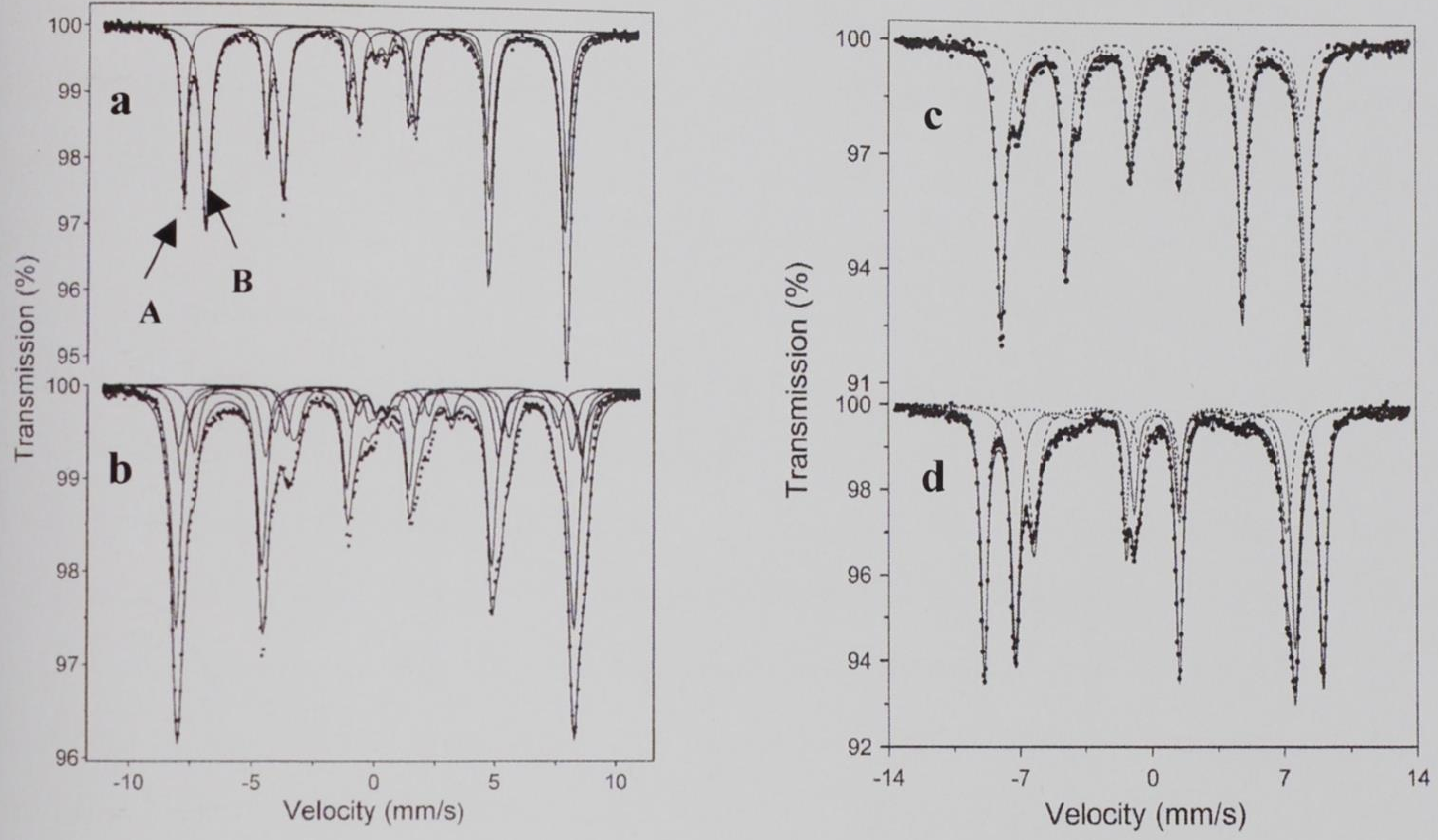

Fig. 10. Mössbauer spectra of magnetite of a) near-stoichiometric magnetite (RT), b) the same sample taken at 4.2 K, c) non-stoichiometric magnetite (160 K) and d) the same sample taken at 160 K under the magnetic field of 6 T.[25]

WÜSTITE

Wüstite is paramagnetic at RT. When lowering the measurement temperature, however, it becomes antiferromagnetic below T_N (203–211 K) with the electron spins orientated antiparallel in neighbouring (111) planes. T_N depends to some extent on the concentration of defects in the structure, which are very common for this compound.

As one would expect from a paramagnetic compound with a cubic structure, RT Mössbauer spectrum of stoichiometric FeO consists of a single line. The spectrum of non-stoichiometric $Fe_{1-x}O$ however shows an asymmetrically broadened doublet with contribution from Fe^{III}

resonance and from two quadrupoly split Fe^{II} doublets. The component peaks contributing to this spectrum have not been fully resolved as the Fe^{II} and vacancy level in the structure strongly vary. Two doublet components with hyperfine parameters of $\delta = 0.95$ mm s^{-1}, $\Delta E_Q = 0.44$ mm s^{-1} and $\delta = 0.90$ mm s^{-1}, $\Delta E_Q = 0.79$ mm s^{-1} respectively are stated by Cornell and Schwertmann.[1]

3 UP TO DATE KNOWLEDGE OF THE THERMAL DECOMPOSITION OF $FeC_2O_4{\cdot}2H_2O$

Metal oxalates represent an important group of compounds employed in solid-state chemistry as precursors for thermally induced syntheses of various nanocrystalline metal oxides.[28–42]

In recent years many studies on the thermal behaviour of ferrous oxalate dihydrate ($FeC_2O_4{\cdot}2H_2O$) in various reaction atmospheres have been published.[43–57] Depending on the experimental conditions, a diversified scale of reactions resulting in solid products varying in composition and valence state of iron has been reported. From the point of view of the basic research, the mechanism of these solid-state reactions is the key experimental issue as the published data are very controversial. The practical reason of interest in $FeC_2O_4{\cdot}2H_2O$ is its easy thermal decomposability yielding various nanocrystalline phases (α-Fe, various iron carbides or iron nitrides) including iron oxides (especially γ-Fe_2O_3 and Fe_3O_4) with great application potential.[1–4]

Obviously one can easily come across many experimental conditions that influence transformation routes, their intermediates and the final products, but the reaction atmosphere represents the most important one. With respect to the reaction atmosphere, the decomposition process seems to be the most straightforward under *oxidative conditions* (air, O_2). It is generally agreed that the transformation process occurs in two steps including dehydration followed immediately by oxidative decomposition resulting in α-Fe_2O_3 (hematite) as the final decomposition product.[43–48] There are however some uncertainties concerning possible intermediates. Thus, FeO [43–45] and Fe_3O_4 [46] were suggested to be the primary decomposition products in oxygen or dry air, while γ-Fe_2O_3 (maghemite) was stabilized when a significant amount of water vapour (assumption of the authors) was present in the reaction atmosphere.[43,45,49,50]

The conversion process in an *inert atmosphere* (N_2, Ar) or vacuum proceeds in two steps too but, unlike in oxidative conditions, the individual steps are much better separated and the composition of the reaction products seems to be more controversial. Most authors identify FeO as the primary conversion phase that subsequently decomposes to Fe_3O_4 and α-Fe due to its instability below 570 °C.[44,51,52] The uncertainties however concern the following conversion steps and the composition of the final transformation products. Thus, α-Fe_2O_3 along with FeO and Fe_3O_4 were identified in the XRD pattern of a sample isothermally treated in dry nitrogen at 440 °C.[53] Primary creation of FeO in dry nitrogen was also observed by *Rane et al.*,[45] who suggest the subsequent reaction of FeO with FeC_2O_4 yielding Fe_3O_4 as the final decomposition product. In the case of a nitrogen atmosphere containing water vapour, Fe_3O_4 as a single phase was detected,[43] as well as in an argon atmosphere.[53,54] Despite the same reaction atmosphere (Ar), a completely different phase composition of the samples including Fe_4C, Fe_3O_4 and Fe is reported,[55] evidently due to the participation of the conversion gas in the reaction system.

Thermal decomposition of $FeC_2O_4 \cdot 2H_2O$ carried out in a *reducing atmosphere* of H_2 proceeds again in two steps taking place at quite separate temperatures, attributed to primary dehydration followed by reductive decomposition. Among the solid reaction products, FeO, Fe_3O_4, α-Fe and Fe_3C were detected depending on the temperature conditions. As expected, FeO as the primary product consequently decomposed into Fe_3O_4 and α-Fe.[54,56] In the next reaction steps magnetite and iron carbide were transformed to α-Fe, although the intermediate formation of Fe_3C is marginally discussed. In addition to pure hydrogen, its mixture with NH_3 in a ratio of 1:1 was used as a reduction atmosphere to monitor the decomposition mechanism of $FeC_2O_4 \cdot 2H_2O$. Mössbauer spectra revealed a mixture of FeO with superparamagnetic Fe_3O_4 at the very beginning of the conversion. At higher temperatures reduction of Fe_3O_4 to α-Fe and its nitridation towards various iron nitrides took place simultaneously.[57]

To sum the published data up, when comparing some of the results obtained in oxidative and inert atmospheres with those obtained under reducing conditions it seems to be highly probable that gaseous conversion products (especially reducing carbon monoxide) more or less participated in the formation of solid phases through the solid-gas reactions. This can be related to the experimental arrangement, especially to insufficient draining of the decomposition gases by passing through the used atmosphere. Surprisingly, there are no literature data on the thermal decomposition of ferrous oxalate dihydrate in the atmosphere of the conversion gases.

Thus, being aware of the literature discrepancies concerning a) the compounds observed under oxidative and inert conditions and b) the not sufficiently cleared up conditions leading towards the presence of application-attractive maghemite (γ-Fe_2O_3), I have decided to a) study a system in which the decomposition gaseous products have the full possibility to participate in the decomposition process (Section 4) and b) to clarify the possibility of the formation of nanocrystalline maghemite nanoparticles in air (Section 5).

4 THERMAL DECOMPOSITION OF $FeC_2O_4 \cdot 2H_2O$ IN THE ATMOSPHERE OF CONVERSION GASES

4.1 SAMPLE PREPARATION AND EXPERIMENTAL ARRANGEMENT

Before the thermal treatment, $FeC_2O_4 \cdot 2H_2O$ powder (Sigma Aldrich) was finely homogenized in an agate mortar. A certain amount of material (5.7 mg) was encased inside an aluminium capsule with an interior diameter of 5.45 mm (depth 1.6 mm) and sealed by an aluminium cover (Fig. 11). Dynamic calcinations were carried out in the furnace of a thermogravimetric analysis (TGA) device (TGA XP–10, THASS GmbH) – the drawing of the overall experimental arrangement is given in Fig. 12. The samples were dynamically heated up to chosen temperatures (max. 640 °C) with a heating rate of 5 °C min^{-1} and then quickly (−20–−25 °C min^{-1}) cooled down. To prevent the access of oxygen from the air into the reaction system the furnace was permanently (during both heating and cooling processes) supplied with a continuous flow of nitrogen (50 ml min^{-1}).

Fig. 11. Aluminium capsule with cover.

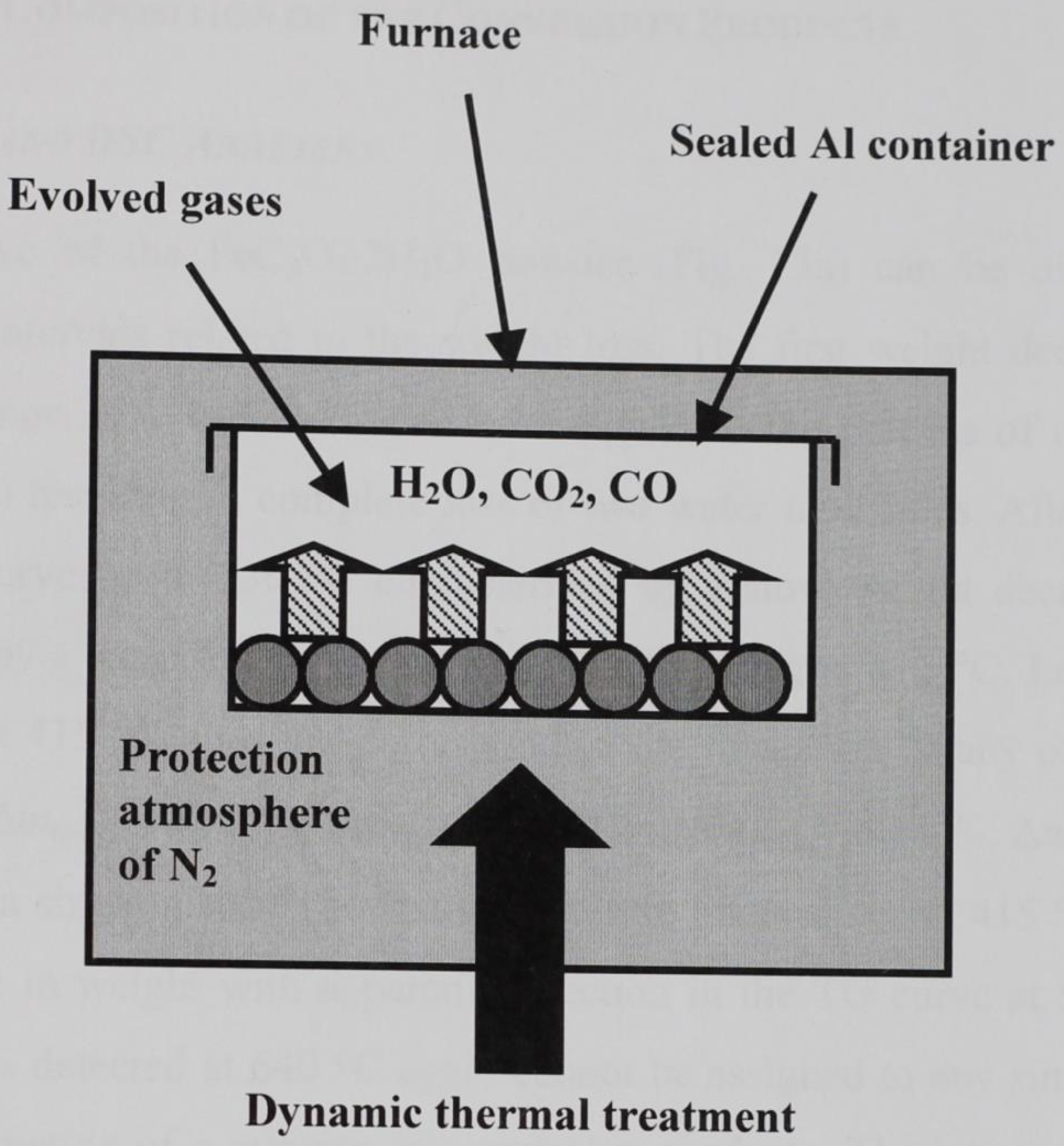

Fig. 12. Experimental arrangement of the system used to the study of the thermal decomposition of $FeC_2O_4{\cdot}2H_2O$ in the atmosphere of the conversion gases.

4.2 EXPERIMENTAL METHODS

The dynamics of the decomposition process was checked by differential scanning calorimetry (DSC) measurement (DSC XP–10, THASS GmbH) within the range of 25–400 °C with a heating rate of 1 °C min^{-1}.

Solid decomposition products were identified *ex-situ* by Mössbauer spectroscopy and X-ray powder diffraction (XRD). Transmission ^{57}Fe Mössbauer spectra of 512 channels were collected using a Mössbauer spectrometer in constant acceleration mode with a ^{57}Co(Rh) source. Measurements were carried out at 300 and 5 K using a cryomagnetic system from Oxford Instruments. XRD patterns were recorded using a Philips X'Pert MPD device with CoK_α radiation and equipped with primary monochromator and X'Celerator detector. Powdered samples were spread on silicon slides and step-scanned within the angular range 10–120° (in conventional 2Θ geometry) with a step of 0.008°.

4.3 PHASE COMPOSITION OF THE CONVERSION PRODUCTS

4.3.1 TGA AND DSC ANALYSES

The TG curve of the $FeC_2O_4{\cdot}2H_2O$ powder (Fig. 13a) can be divided into three main temperature intervals related to the weight loss. The first weight decrease of about 20.1 % within the range of 170–230 °C can be assigned to the process of dehydration (theoretical value 20.0 %) resulting in complete loss of two water molecules. Afterwards, there is a long part of the curve up to 330 °C characterized by a slow weight decrease (1.2 %) followed immediately by a steep fall in weight (39.2 %) finishing at 415 °C. Let's notice that the total weight loss at 415 °C does not correspond to the formation of any of the possibly expected compounds ($\Delta m_{\alpha\text{-Fe}}$ = 62.0 %, Δm_{Fe3O4} = 57.1 %, Δm_{FeO} = 60.1 %, Δm_{Fe2O3} = 55.6 %, Δm_{Fe3C} = 66.7 %) as a single phase. The last temperature interval above 415 °C is accompanied by a slow decrease in weight with apparent inflection in the TG curve at 535 °C. The total mass loss of 62.3 % detected at 640 °C again cannot be assigned to any single phase and indicates rather the formation of a mixture of conversion products. The letters (A–G) in the TG curve indicate the temperatures at which the dynamic heating was stopped and the phase composition of samples consequently analysed by Mössbauer spectroscopy (see Section 4.3.2) and XRD (see Section 4.3.3).

DSC analysis (Fig. 13b) was performed with a slower heating rate allowing better resolution of the overlapped processes as indicated in the TG curve. Generally, the curve shows two endothermic effects. The first one, narrower and more intensive, with a minimum at 168 °C stands obviously for the process of dehydration. The second one, much broader, irregular in its shape, and apparently weaker in intensity with a local minimum at 376 °C, reflects a more complex process embodying several steps proceeding either simultaneously and/or consequently within a relatively short temperature range (285–395 °C). The slight temperature shift between the heat effects observed in DSC and the corresponding weight losses in TG have obviously been caused by the different heating rates.

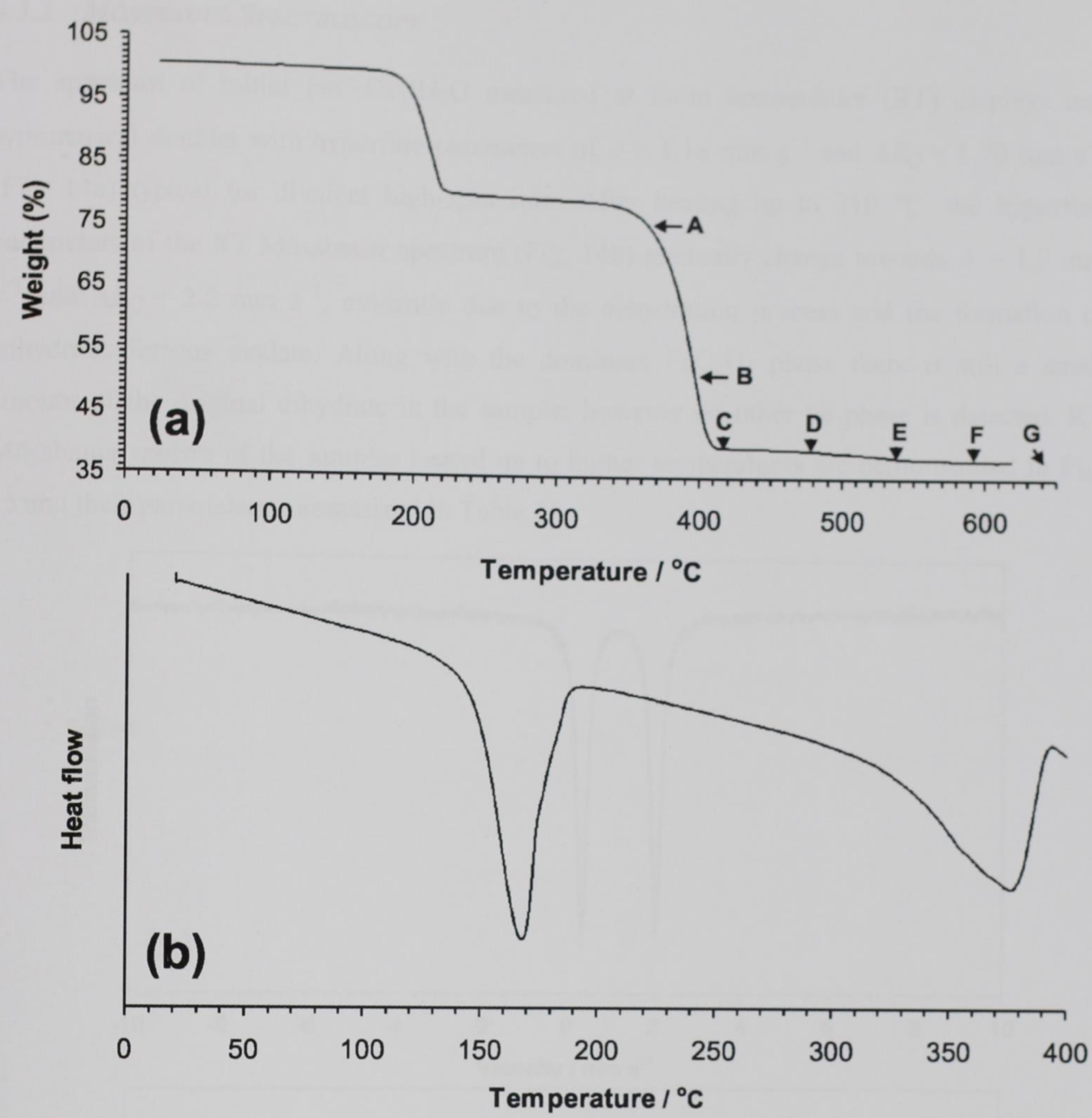

Fig. 13. TGA (a) and DSC (b) curves of $FeC_2O_4 \cdot 2H_2O$ dynamically heated in atmosphere of own decomposition gaseous products. Heating rates: 5 °C min^{-1} (TG), 1 °C min^{-1} (DSC).

4.3.2 Mössbauer Spectroscopy

The spectrum of initial $FeC_2O_4{\cdot}2H_2O$ measured at room temperature (RT) displays one symmetrical doublet with hyperfine parameters of $\delta = 1.18$ mm s^{-1} and $\Delta E_Q = 1.70$ mm s^{-1} (Fig. 14a) typical for divalent high-spin iron. After heating up to 210 °C, the hyperfine parameters of the RT Mössbauer spectrum (Fig. 14b) gradually change towards $\delta = 1.2$ mm s^{-1} and $\Delta E_Q = 2.2$ mm s^{-1}, evidently due to the dehydration process and the formation of anhydrous ferrous oxalate. Along with the dominant FeC_2O_4 phase there is still a small amount of the original dihydrate in the sample; however no other Fe-phase is detected. RT Mössbauer spectra of the samples heated up to higher temperatures are demonstrated in Fig. 15 and their parameters summarized in Table 1.

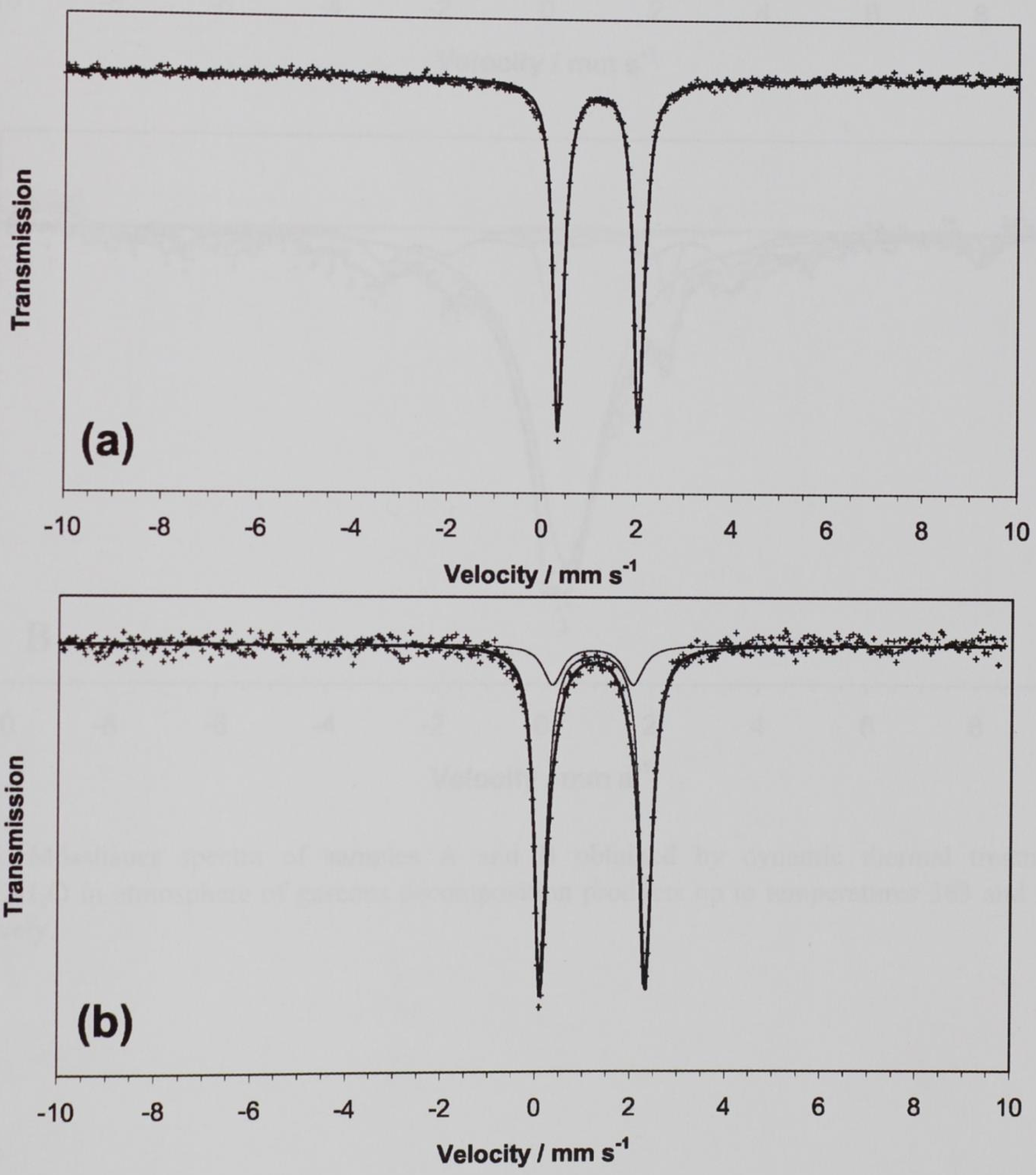

Fig. 14. RT Mössbauer spectra of non-treated $FeC_2O_4{\cdot}2H_2O$ (a) and of the sample heated up to 210 °C (b).

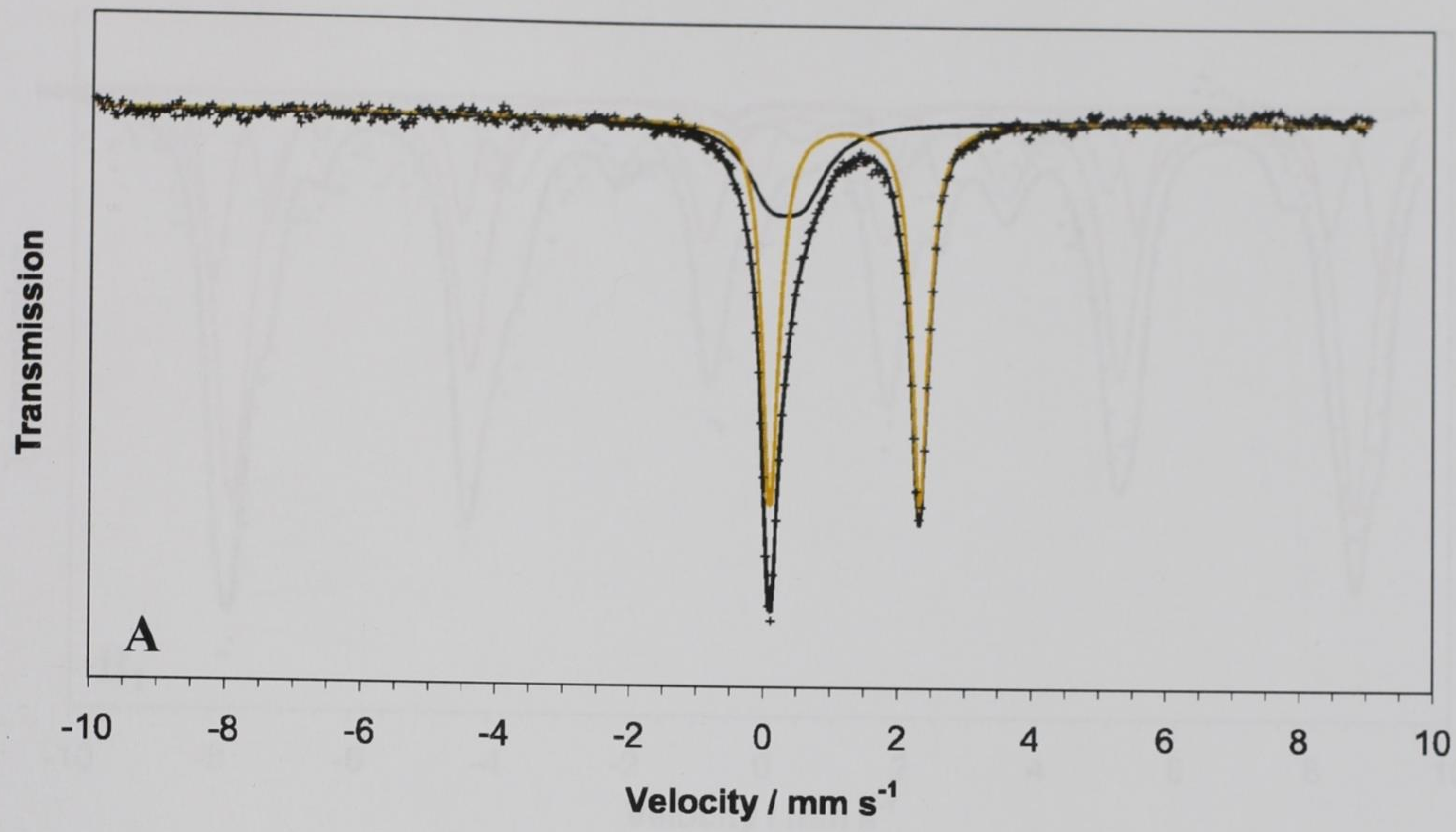

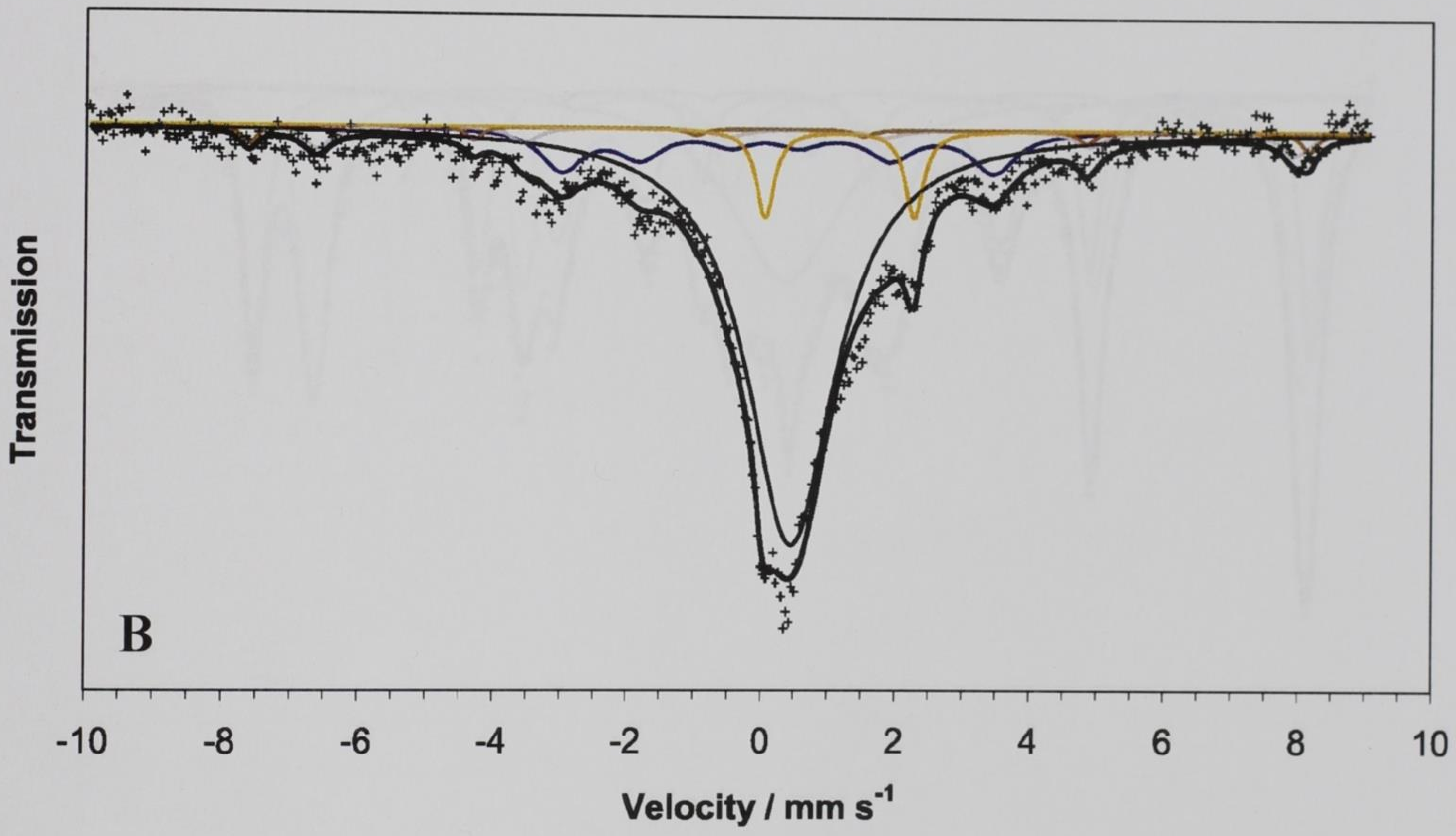

Fig. 15. Mössbauer spectra of samples A and B obtained by dynamic thermal treatment of $FeC_2O_4 \cdot 2H_2O$ in atmosphere of gaseous decomposition products up to temperatures 363 and 395 °C respectively.

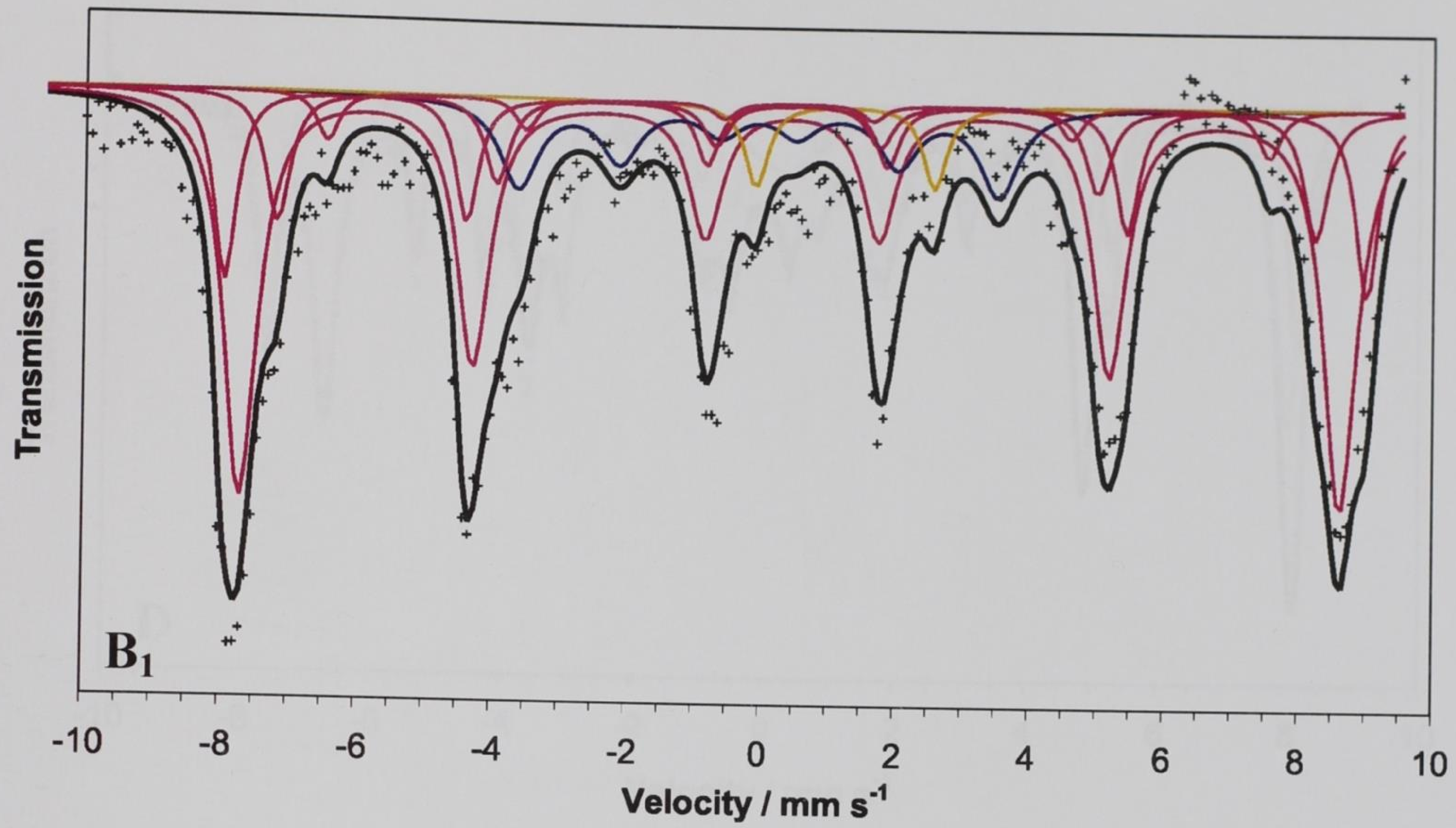

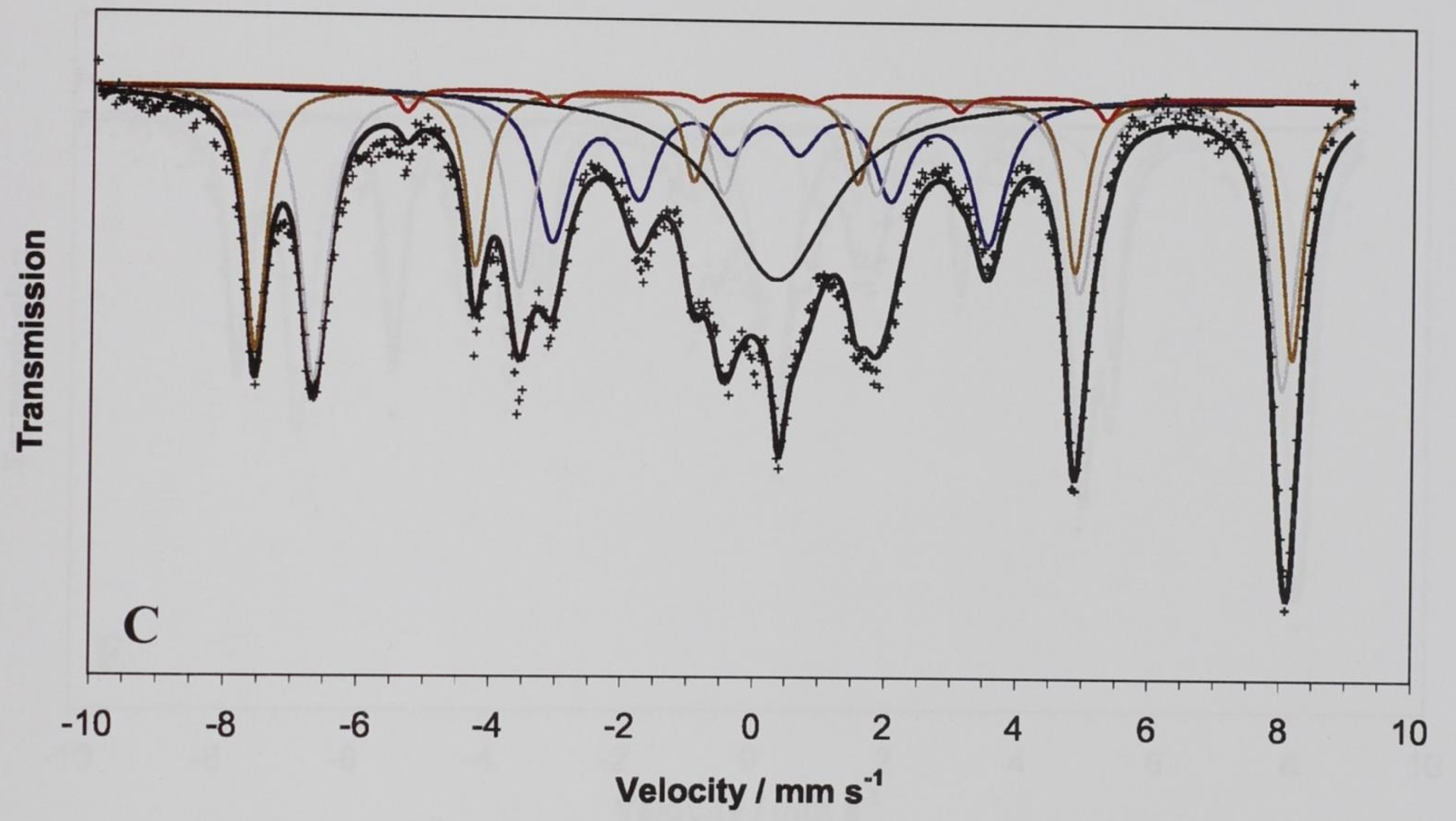

Fig. 15. Mössbauer spectra of samples B$_1$ and C. B$_1$ – LT Mössbauer spectrum (5 K) of sample B. Sample C obtained by dynamic thermal treatment of $FeC_2O_4{\cdot}2H_2O$ in atmosphere of gaseous decomposition products up to 415 °C.

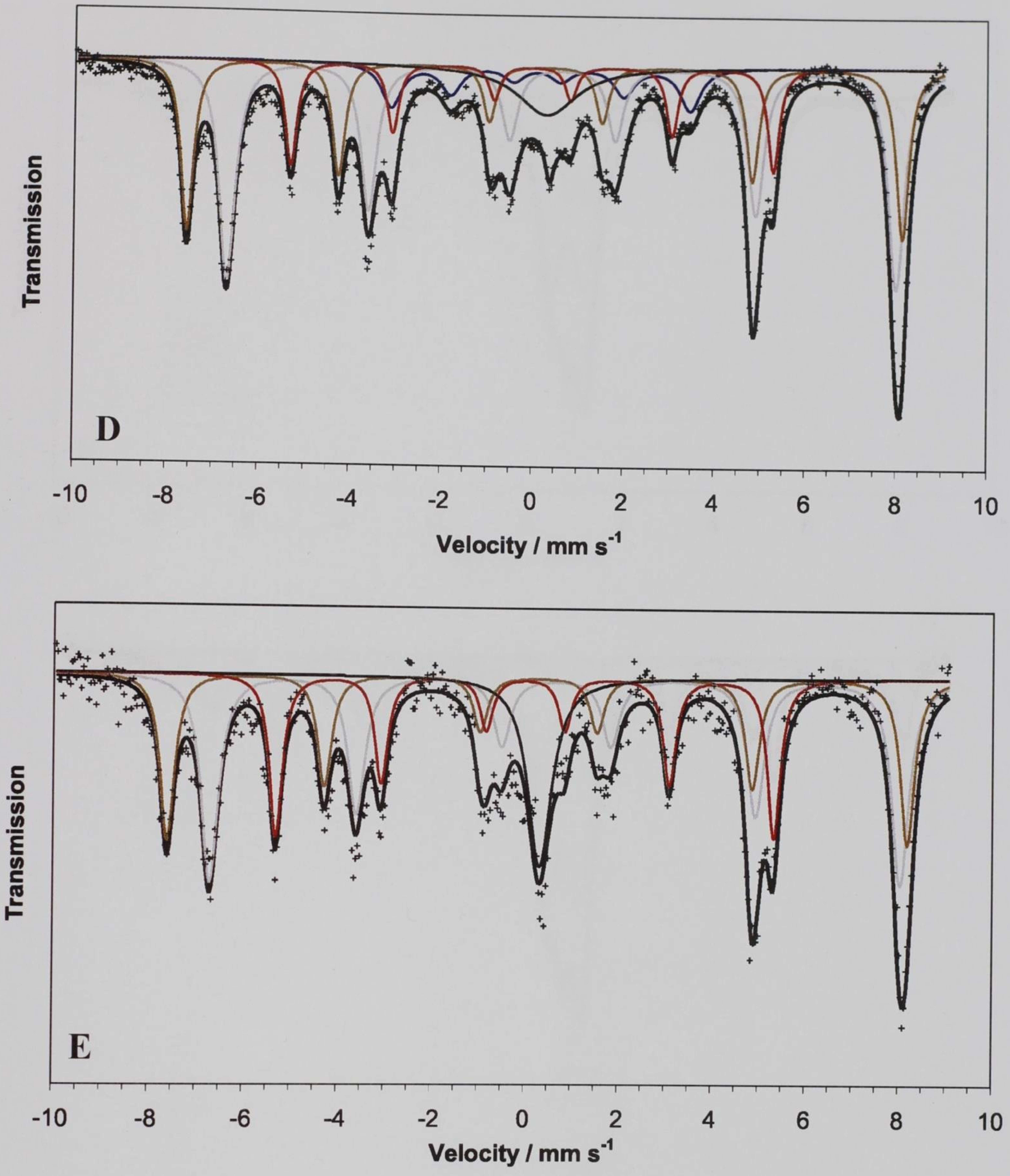

Fig. 15. Mössbauer spectra of samples D and E obtained by dynamic thermal treatment of $FeC_2O_4{\cdot}2H_2O$ in atmosphere of gaseous decomposition products up to temperatures 475 and 535 °C respectively.

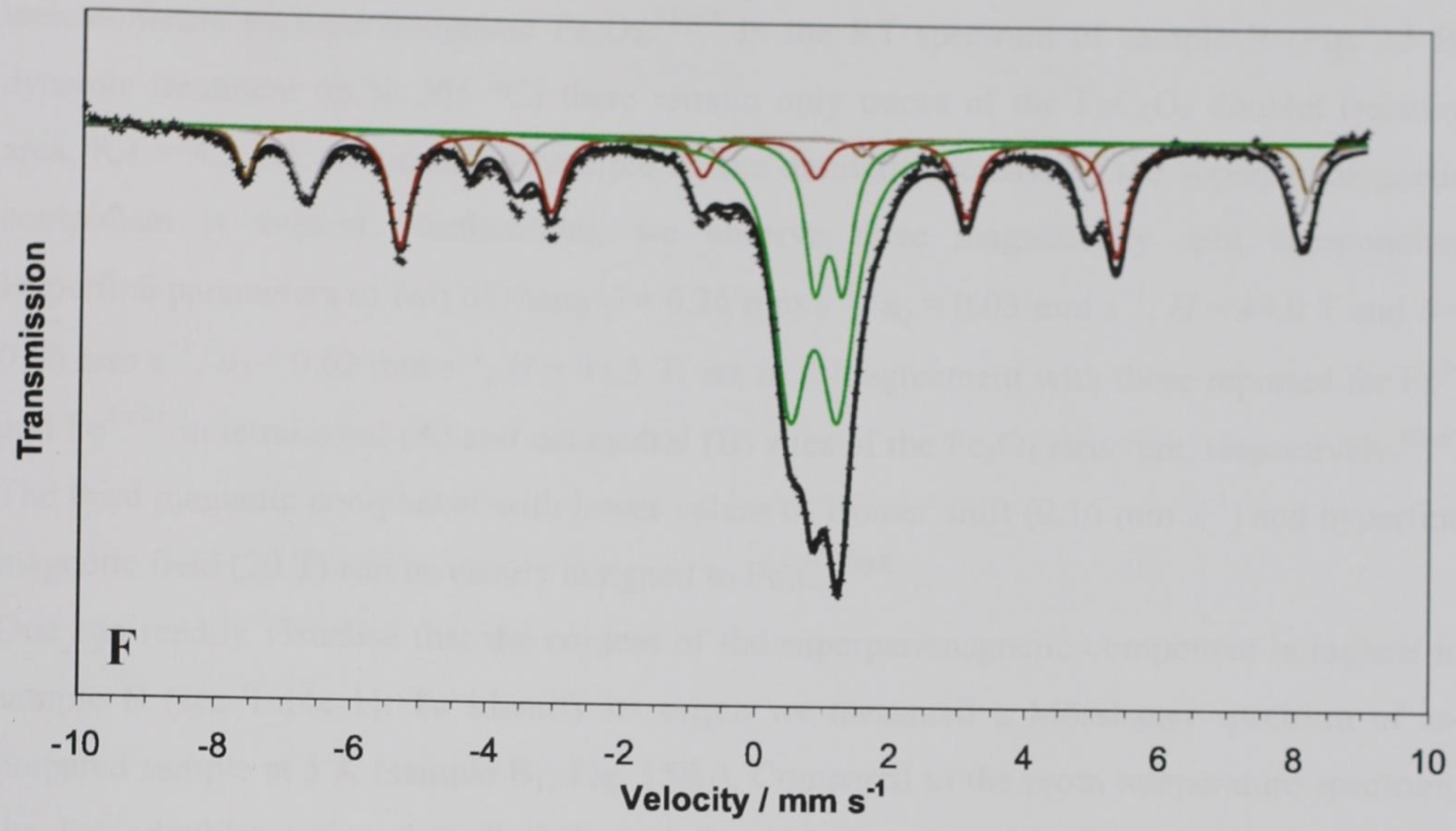

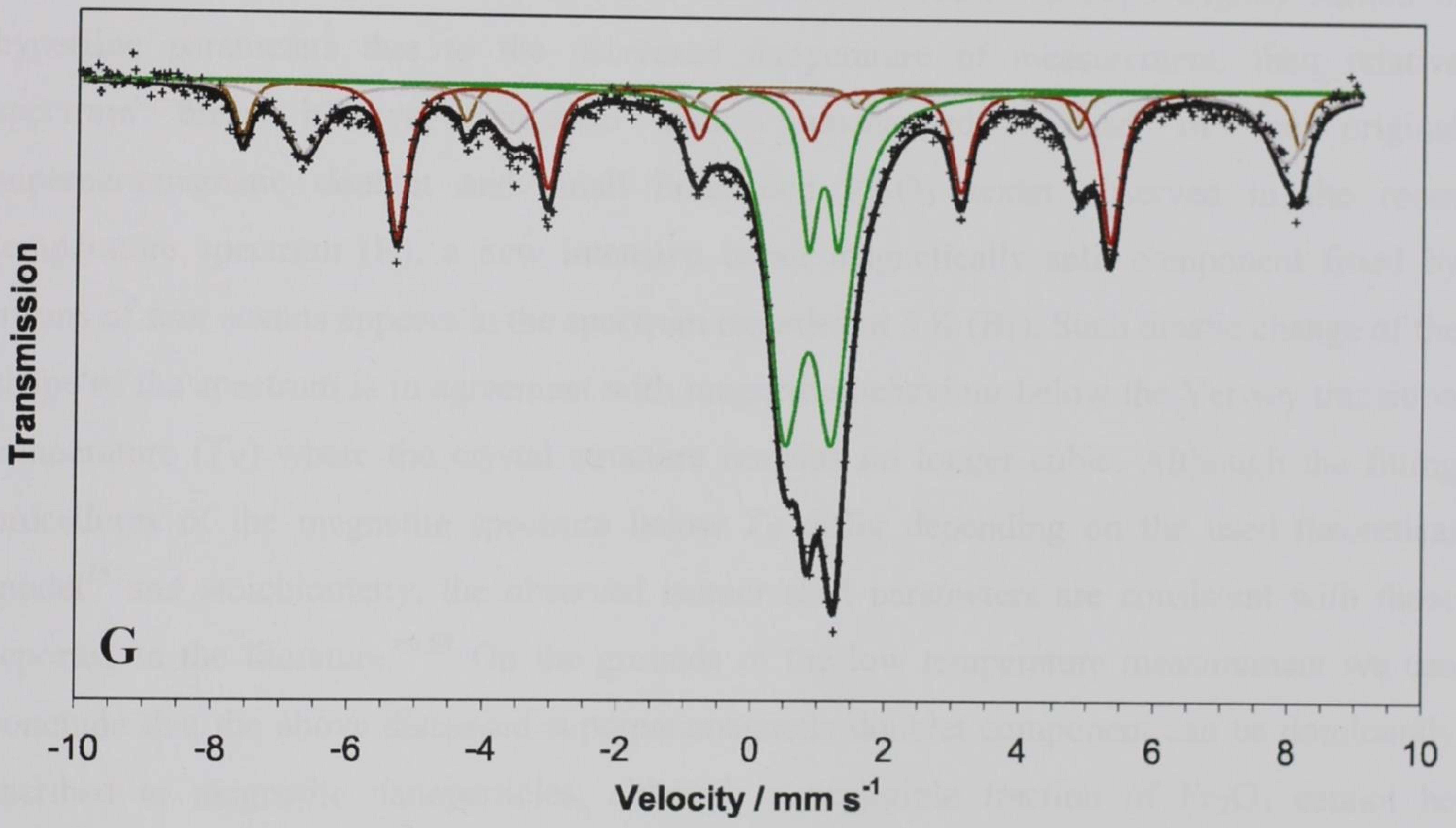

Fig. 15. Mössbauer spectra of samples F and G obtained by dynamic thermal treatment of $FeC_2O_4 \cdot 2H_2O$ in atmosphere of gaseous decomposition products up to temperatures 590 and 640 °C respectively.

The initial stage of decomposition of anhydrous FeC_2O_4 (up to 363 °C) is well characterized by the RT Mössbauer spectrum of sample A (Fig. 15A), which can be fitted with two doublets. Following the hyperfine parameters (see Table 1), the first one can be attributed to remaining FeC_2O_4. Isomer shift of the second broad component ($\delta = 0.36$ mm s^{-1}) is typical for superparamagnetic iron(III) oxides[48,58–60], however it also corresponds well to more or less stoichiometric superparamagnetic Fe_3O_4.[61–64] In the RT spectrum of sample B (Fig. 15 B; dynamic treatment up to 395 °C) there remain only traces of the FeC_2O_4 doublet (relative area, RA = 4.3 %). Compared to sample A, the dramatic increase of the superparamagnetic component is evident. Furthermore, we observe three magnetically split components. Hyperfine parameters of two of them, $\delta = 0.26$ mm s^{-1}, $\varepsilon_Q = 0.03$ mm s^{-1}, $H = 49.0$ T and $\delta = 0.66$ mm s^{-1}, $\varepsilon_Q = 0.02$ mm s^{-1}, $H = 45.3$ T, are in full agreement with those reported for Fe^{3+} and $Fe^{3+/2+}$ in tetrahedral (A) and octahedral (B) sites of the Fe_3O_4 structure, respectively.[65–67] The third magnetic component with lower values of isomer shift (0.16 mm s^{-1}) and hyperfine magnetic field (20 T) can be clearly assigned to Fe_3C.[60,68]

One can readily visualise that the content of the superparamagnetic component is highest in sample B (see Table 1). To identify its origin we measured a Mössbauer spectrum of as-prepared sample at 5 K (sample B_1, Fig. 15B_1). Compared to the room temperature spectrum, the Fe^{2+} doublet assigned to FeC_2O_4 and the sextet attributed to Fe_3C slightly shifted in hyperfine parameters due to the decreased temperature of measurement, their relative spectrum areas however remained almost unchanged. Instead of the original superparamagnetic doublet and small broadened Fe_3O_4 sextet observed in the room temperature spectrum (B), a new intensive broad magnetically split component fitted by means of four sextets appears in the spectrum recorded at 5 K (B_1). Such drastic change of the shape of the spectrum is in agreement with magnetite behaviour below the Verwey transition temperature (T_V) where the crystal structure remains no longer cubic. Although the fitting procedures of the magnetite spectrum below T_V differ depending on the used theoretical model[25] and stoichiometry, the observed isomer shift parameters are consistent with those reported in the literature.[66,69] On the grounds of the low temperature measurement we can conclude that the above discussed superparamagnetic doublet component can be dominantly ascribed to magnetite nanoparticles, although a negligible fraction of Fe_2O_3 cannot be excluded.

Compared to sample B, the RT Mössbauer spectrum of sample C (Fig. 15C; thermal treatment up to 415 °C) reveals a decrease of the spectrum area of the superparamagnetic component accompanied by a simultaneous increase of the ferrimagnetic Fe_3O_4 fractions, obviously as a result of the thermally induced crystallization process of magnetite. Hyperfine parameters of Fe_3C evidence better crystallinity and a more ordered structure as demonstrated by a slight change of the hyperfine magnetic field ($H = 20.5$ T). As the last phase a tiny amount (1.6 % of the total spectrum area) of α-Fe represented by a magnetically split component with a zero value of isomer shift and a hyperfine magnetic field of 33 T was identified in the spectrum of sample C.

The qualitative phase composition found in the Mössbauer spectrum of sample D (Fig. 15D) is identical to that observed in the previous case (sample C). From the quantitative point of view, there is a significant increase of the spectrum area of α-Fe (13.9 *vs.* 1.6 %) while the area of the Fe_3C sextet is clearly reduced (10.1 *vs.* 20.5 %). Such comparison therefore indicates the progressive decomposition of iron carbide to alpha-iron at temperatures between 415 and 475 °C. The Mössbauer spectrum of the sample dynamically heated up to 535 °C (E, Fig. 15E) does not reveal any presence of Fe_3C. The total content of magnetite including superparamagnetic and ferrimagnetic fractions (*ca.* 77 %) remains almost the same as in samples C and D. This fact reflects the thermal stability of the magnetite phase up to 535 °C. The Mössbauer spectra of samples F and G (thermal treatment up to 590 and 640 °C respectively) are very similar and exhibit the presence of magnetite, α-Fe and new Fe^{2+} doublets with parameters of $\delta = 1.02–1.05$ mm s^{-1}, $\Delta E_Q = 0.41–0.44$ mm s^{-1} and $\delta = 0.83–0.84$ mm s^{-1}, $\Delta E_Q = 0.70–0.71$ mm s^{-1}. The hyperfine parameters of the Fe^{2+} doublets match well with those reported for FeO (wüstite).[70,71] The spectrum area of Fe^{2+} doublets in sample F (*ca.* 52 %) corresponds to the decrease of the magnetite content between 535 °C and 590 °C (77 *vs.* 24 %), evidently due to the proceeding reduction of Fe_3O_4 to FeO within this temperature range. Above 590 °C, no final conversion products including Fe_3O_4, FeO and α-Fe undergo any other thermally induced reactions as evidenced by the constant phase composition of samples F and G (see Figs. 15F and 15G).

Table 1 Mössbauer parameters of samples A, B, B_1, C, D, E, F, G.

Sample	T_{max}/°C[a]	T_{meas}/K[b]	δ/mm s^{-1}[d]	ΔE_Q/mm s^{-1}[e]	ε_Q/mm s^{-1}[f]	H/T[g]	R*A* (%)[h]	Site assignment
A	363	RT[c]	1.21	2.23	–	–	70.1	Ferrous oxalate
			0.36	0.49	–	–	29.9	SP magnetite
B	395	RT	1.15	2.22	–	–	4.3	Ferrous oxalate
			0.35	0.21	–	–	73.7	SP magnetite
			0.26	–	0.03	49.0	2.5	Magnetite (site A)
			0.66	–	0.02	45.3	5.2	Magnetite (site B)
			0.16	–	0.07	20.0	14.3	Cementite
B_1	395	5	1.24	1.98	–	–	3.7	Ferrous oxalate
			0.28	–	0.09	25.0	13.3	Cementite
			0.53	–	−0.02	52.7	16.1	Magnetite below T_V
			0.46	–	−0.02	50.7	50.7	
			0.54	–	−0.02	48.0	12.1	
			0.68	–	0.17	44.3	4.0	
C	415	RT	0.32	0.05	–	–	22.7	SP magnetite
			0.29	–	0.02	48.8	22.5	Magnetite (site A)
			0.66	–	0.02	45.6	32.7	Magnetite (site B)
			0.15	–	0.09	20.5	20.5	Cementite
			0.01	–	0	33.0	1.6	Alpha-iron
D	475	RT	0.32	0.08	–	–	9.9	SP magnetite
			0.29	–	0.01	48.8	24.9	Magnetite (site A)
			0.66	–	0.02	45.6	41.2	Magnetite (site B)
			0.14	–	0.08	20.4	10.1	Cementite
			0.02	–	−0.01	32.9	13.9	Alpha-iron
E	535	RT	0.32	0	–	–	12.5	SP magnetite
			0.28	–	0.03	49.0	25.8	Magnetite (site A)
			0.66	–	0.02	45.7	38.8	Magnetite (site B)
			0.0	–	0	33.0	22.9	Alpha-iron
F	590	RT	0.28	–	0.02	49.0	7.6	Magnetite (site A)
			0.66	–	0.01	45.8	16.3	Magnetite (site B)
			0.02	–	0.01	33.1	23.2	Alpha-iron
			1.02	0.41	–	–	13.0	Wüstite
			0.84	0.71	–	–	39.9	
G	640	RT	0.27	–	0.02	48.9	7.5	Magnetite (site A)
			0.63	–	0.01	45.5	20.0	Magnetite (site B)
			0.01	–	0.01	33.0	22.6	Alpha-iron
			1.05	0.44	–	–	9.9	Wüstite
			0.83	0.70	–	–	40.0	

[a] T_{max} = temperature up to which the decomposition proceeded (see text), [b] T_{meas} = temperature at which the Mössbauer spectrum was recorded, [c] RT = room temperature, [d] δ = isomer shift (with respect to metallic iron, ±0.01), [e] ΔE_Q = quadrupole splitting (±0.01), [f] ε_Q = quadrupole shift (±0.01), [g] H = hyperfine magnetic field (±0.1), [h] RA = relative spectrum area (±0.2).

4.3.3 XRD Data

Generally, the results obtained by X-ray powder diffraction agree well with the phase composition of the heated samples determined by Mössbauer spectroscopy. The representative diffraction patterns well demonstrating the decomposition process are shown in Fig. 16.

The XRD pattern of sample A (not shown) reveals the diffraction lines corresponding to anhydrous ferrous oxalate as the only crystalline phase in the system. Moreover, slight indications of diffraction peaks, which can be ascribed to the nanocrystalline spinel structure either of maghemite or magnetite, were detected.

Sample B (Fig. 16B) represents a mixture of ferrous oxalate, iron carbide and magnetite, as the presence of maghemite, which has the spinel structure of the same type and therefore an almost identical diffraction pattern, was excluded on the grounds of the Mössbauer measurement. Following the XRD pattern of sample B, magnetite is a prevailing component in the primary stage of the decomposition of ferrous oxalate; the broad diffraction lines however reflect its nanocrystalline character, which matches well with the Mössbauer data.

In sample C (Fig. 16C) there is no longer evidence of ferrous oxalate. Its absence indicates that the oxalate transformation finished after heating up to 415 °C. The diffraction lines of magnetite are much narrower and more intensive than in sample B, clearly due to its progressive crystallization above 395 °C. One should object at this point, how is it possible that while Mössbauer spectroscopy shows a fraction of superparamagnetic nanoparticles at temperatures above 400 °C, the quite narrow XRD lines indicate rather larger particles? This represents a relevant objection, which can be however easily explained: The intensive and narrow diffraction lines observed in XRD reflect the contribution of the larger particles with higher coherent length, while the contribution of the smaller (superparamagnetic) particles is in this sense suppressed. In accordance with the Mössbauer spectrum of sample C, a trace admixture of α-Fe was identified.

The qualitative phase composition found from the XRD pattern of sample D (not shown) is the same as that in sample C, however the line intensities indicate the increasing content of iron at the expense of iron carbide. The XRD pattern of sample E (Fig. 16E) exhibits a mixture of only two phases – magnetite and metallic iron. While the lines belonging to Fe_3C completely disappeared, more intensive diffraction lines of α-Fe evidence that its content in the sample increases with temperature. It is worth pointing out that the line intensities belonging to magnetite remain almost unchanged in the XRD patterns of samples C, D and E.

The constant content of the magnetite phase supports the quantitative Mössbauer analysis and reflects its thermal stability up to 535 °C.

Above 535 °C, a distinct fall of magnetite content accompanied by new diffraction peaks belonging to non-stoichiometric FeO was recorded in the XRD patterns of samples F (not shown) and G (Fig. 16G).

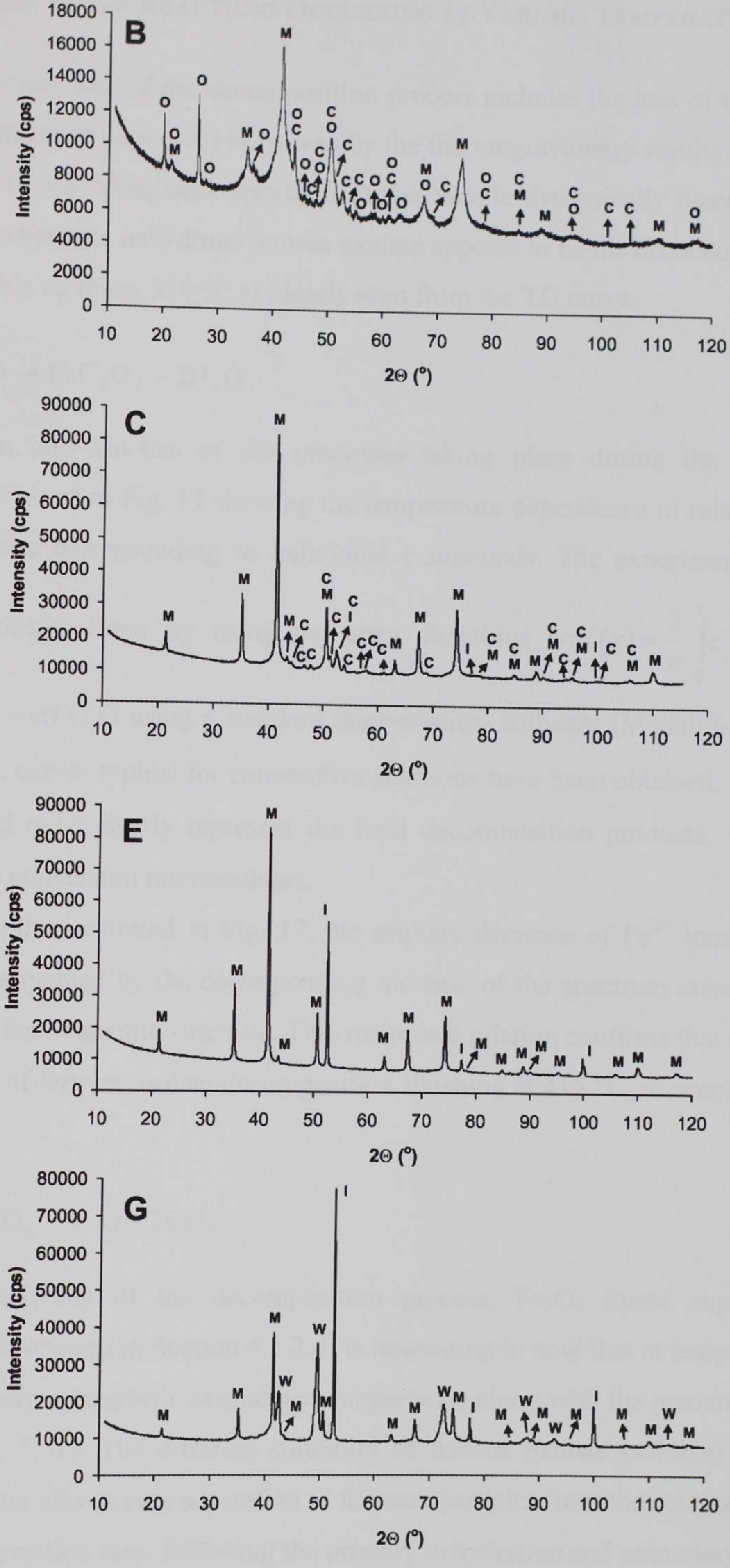

Fig. 16. XRD patterns of representative samples B, C, E and G. Assignment of individual phases: O - ferrous oxalate, FeC_2O_4, C - cementite, Fe_3C, M - magnetite, Fe_3O_4, I - iron, α-Fe, W - wüstite, FeO

4.4 Discussion of the Reactions Occurring at Various Temperatures

Apparently, the first step of the decomposition process includes the loss of two molecules of water of crystallization (eqn (12)) as proved by the thermogravimetry results (see Section 4.1) and confirmed by the Mössbauer spectrum of the sample dynamically heated up to 210 °C (see Fig. 14b), where the anhydrous ferrous oxalate appears to be the dominant phase. FeC_2O_4 is thermally stable up to *ca.* 350 °C as clearly seen from the TG curve.

$$FeC_2O_4 \cdot 2H_2O \rightarrow FeC_2O_4 + 2H_2O \qquad (12)$$

The mechanism and kinetics of the processes taking place during the further thermal treatment are reflected in Fig. 17 showing the temperature dependence of relative areas of the Mössbauer spectra corresponding to individual compounds. The experimental points have been mathematically fitted by using the error functions ($\mathrm{erf}(x) = \frac{2}{\pi} \int_0^x \mathrm{e}^{-t^2} \mathrm{d}t$) and their complements ($1 - \mathrm{erf}(x)$) using a standard mathematical software (Matlab 6.5.0, release 13) and as expected, curves typical for consecutive reactions have been obtained. Following these curves, FeO and α-Fe clearly represent the final decomposition products, while Fe_3C and Fe_3O_4 behave as conversion intermediates.

As transparently demonstrated in Fig. 17, the primary decrease of Fe^{2+} ions of the FeC_2O_4 structure is accompanied by the corresponding increase of the spectrum areas corresponding to iron atoms in the magnetite structure. This reciprocal relation confirms that magnetite is the primary product of ferrous oxalate decomposition finishing at 415 °C, in accordance with eqn (13).

$$3FeC_2O_4 \rightarrow Fe_3O_4 + 4CO + 2CO_2 \qquad (13)$$

At the very beginning of the decomposition process, Fe_3O_4 forms superparamagnetic nanoparticles as discussed in Section 4.3.2. It is interesting to note that at temperatures around 360 °C, only superparamagnetic magnetite nanoparticles along with the precursor occur in the sample (see Fig. 15A). The different solubility of ferrous oxalate (soluble) and magnetite (insoluble) in water allows easy separation of the nanoparticles from the reaction mixture.

The third decomposition step, following the primary dehydration and secondary conversion of FeC_2O_4 into magnetite, includes the formation of Fe_3C at temperatures above 363 °C. Generally, there are two possible routes of its formation: either by the reduction of ferrous oxalate (eqn (14a)) or magnetite (eqn (14b)) by carbon monoxide evolved during the previous step (eqn (13)):

$$3FeC_2O_4 + 2CO \rightarrow Fe_3C + 7CO_2, \tag{14a}$$

$$Fe_3O_4 + 6CO \rightarrow Fe_3C + 5CO_2. \tag{14b}$$

With respect to the amount of carbon monoxide necessary for the reduction of one mol of the solid reactant, the reaction (14b) is evidently less probable as the yield of CO by reaction (13) is much lower than theoretically required. Moreover, based on the quantitative Mössbauer data in Fig. 17, there is no evidence to suggest that there has been a link between magnetite and iron carbide. Hence, it is obvious, that iron carbide is formed in the third decomposition step (at temperatures above *ca.* 360 °C) as a result of the reduction of FeC_2O_4 by gaseous CO (eqn (14a)), whereas the reaction mechanism (14b) can be almost excluded.

Taking into account reactions 12, 13 and 14a and following the quantitative phase composition of sample C determined by Mössbauer spectroscopy, the overall decomposition process proceeding up to 415 °C can be expressed by the general equation:

$$\begin{gathered} FeC_2O_4 \cdot 2H_2O + 2b/3\,CO \rightarrow \\ a/3\,Fe_3O_4 + 4a/3\,CO + 2a/3\,CO_2 + b/3\,Fe_3C + 7b/3\,CO_2 + 2H_2O. \end{gathered} \tag{15}$$

The letters *a* and *b* (*a* + *b* = 1) in the stoichiometry coefficients represent the relative spectrum areas in the Mössbauer spectrum of sample C. For the sake of simplicity, the negligible contribution of α-Fe has been ascribed to Fe_3C as alpha-iron is formed exclusively at the expense of iron carbide.

After insertion of the variables *a* and *b,* the equation can be evaluated:

$$\begin{gathered} FeC_2O_4 \cdot 2H_2O + 0.15CO \rightarrow \\ 0.26Fe_3O_4 + 0.07Fe_3C + 1.04CO + 1.03CO_2 + 2H_2O. \end{gathered} \tag{16}$$

The theoretical mass loss accompanying this reaction can be easily calculated as 59.2 %, which correlates with the mass loss obtained experimentally from the TG measurement (59.7 %).

Within the temperature region of 475–535 °C (samples D, E), iron carbide is gradually decomposed as manifested by its decreasing spectrum area from 20.5 % to zero, while magnetite, as the second decomposition intermediate, remains stable (Fig. 17). This fall in the iron carbide content is accompanied by a corresponding increase of the content of metallic iron (1.6–23 % of the spectrum area). As no other compounds were observed either by Mössbauer spectroscopy or XRD, we can conclude that α-Fe is formed from iron carbide by its thermal conversion at temperatures 415–535 °C, in accordance with eqn (17):

$$Fe_3C \rightarrow 3Fe + C\,. \tag{17}$$

The fact that carbon was not detected in any of the samples C–E by XRD can be easily explained by its very low weight contribution (less than 1.5 wt % following the Mössbauer data) and probable XRD amorphous character. Within the temperature region of 535–590 °C (samples E, F) a massive decrease in magnetite content compensated by a simultaneous increase of the wüstite content was registered. These trends reflect that there is a direct reaction relation between Fe_3O_4 and FeO in the system. The reach of sufficiently high temperature (535 °C) acts as a trigger for the reduction of magnetite to wüstite as Fe_3O_4 remained stable in a broad temperature interval below it. Concerning the reduction mechanism, there are two possible routes with participation of either carbon monoxide (eqn (18a)) or solid carbon (eqn (18b)) as reducing agents formed in previous reaction steps:

$$Fe_3O_4 + CO \rightarrow 3FeO + CO_2\,, \tag{18a}$$

$$Fe_3O_4 + C \rightarrow 3FeO + CO\,. \tag{18b}$$

Nevertheless, the reduction route (18b) seems to be very improbable or negligible because of the very low content of carbon in the system as mentioned above. On the other hand, the initial molar ratio of carbon monoxide to magnetite (4:1), which are the products of reaction (13) at low temperatures, is much higher than that (1:1) necessary for the high-temperature reduction route (18a). Thus, the amount of CO should be sufficient for the initiation and the course of reaction (18a), although its certain fraction was consumed during the reduction of ferrous oxalate to iron carbide (eqn (14a)). Moreover, it is highly probable that a certain amount of carbon monoxide is oxidized to carbon dioxide (eqn (19)) by air-oxygen trapped inside the capsule during the sample preparation. This hypothesis is supported by the fact that magnetite reduction is not fully completed up to the final temperature of 640 °C, evidently due to the absence of a reducing agent.

$$CO + 1/2\,O_2 \Leftrightarrow CO_2 \tag{19}$$

It is also worth mentioning that there are no indications of the disproportionation of FeO (eqn (20)), as one would expect due to the well-known instability of wüstite below 570 °C. [1,72]

$$4\mathrm{FeO} \Leftrightarrow \mathrm{Fe_3O_4} + \alpha\,\mathrm{Fe} \tag{20}$$

This should be accompanied by a change of the α-Fe content above 535 °C, which has not been observed (see Fig. 17). The reasons behind the presence of FeO in the samples at room temperature could be related to its stabilization by CO_2 that was evolved during the reaction (18a).

4.5 CONCLUSION – TEMPERATURE DEPENDENT REACTION MODEL

Following the obtained experimental results, a unique five-step decomposition mechanism of $FeC_2O_4{\cdot}2H_2O$ in the atmosphere of its conversion gases has been suggested:

I. Release of crystal water proceeding within the temperature range of 170–230 °C:

$$\mathrm{FeC_2O_4 \cdot 2H_2O \rightarrow FeC_2O_4 + 2H_2O}$$

II. Thermally induced conversion of FeC_2O_4 to Fe_3O_4 and carbon oxides at temperatures above 230 °C:

$$\mathrm{3FeC_2O_4 \rightarrow Fe_3O_4 + 4CO + 2CO_2}$$

III. Reduction of ferrous oxalate by carbon monoxide to Fe_3C (above 360 °C):

$$\mathrm{3FeC_2O_4 + 2CO \rightarrow Fe_3C + 7CO_2}$$

IV. Thermal conversion of Fe_3C (415–535 °C):

$$\mathrm{Fe_3C \rightarrow 3Fe + C}$$

V. Thermally induced reduction of magnetite to FeO by carbon monoxide (above 535 °C):

$$\mathrm{Fe_3O_4 + CO \rightarrow 3FeO + CO_2}$$

It should be emphasized that reactions II, III and IV could serve as the guides for thermally induced solid-state syntheses of magnetic Fe_3O_4, Fe_3C and α-Fe nanoparticles.

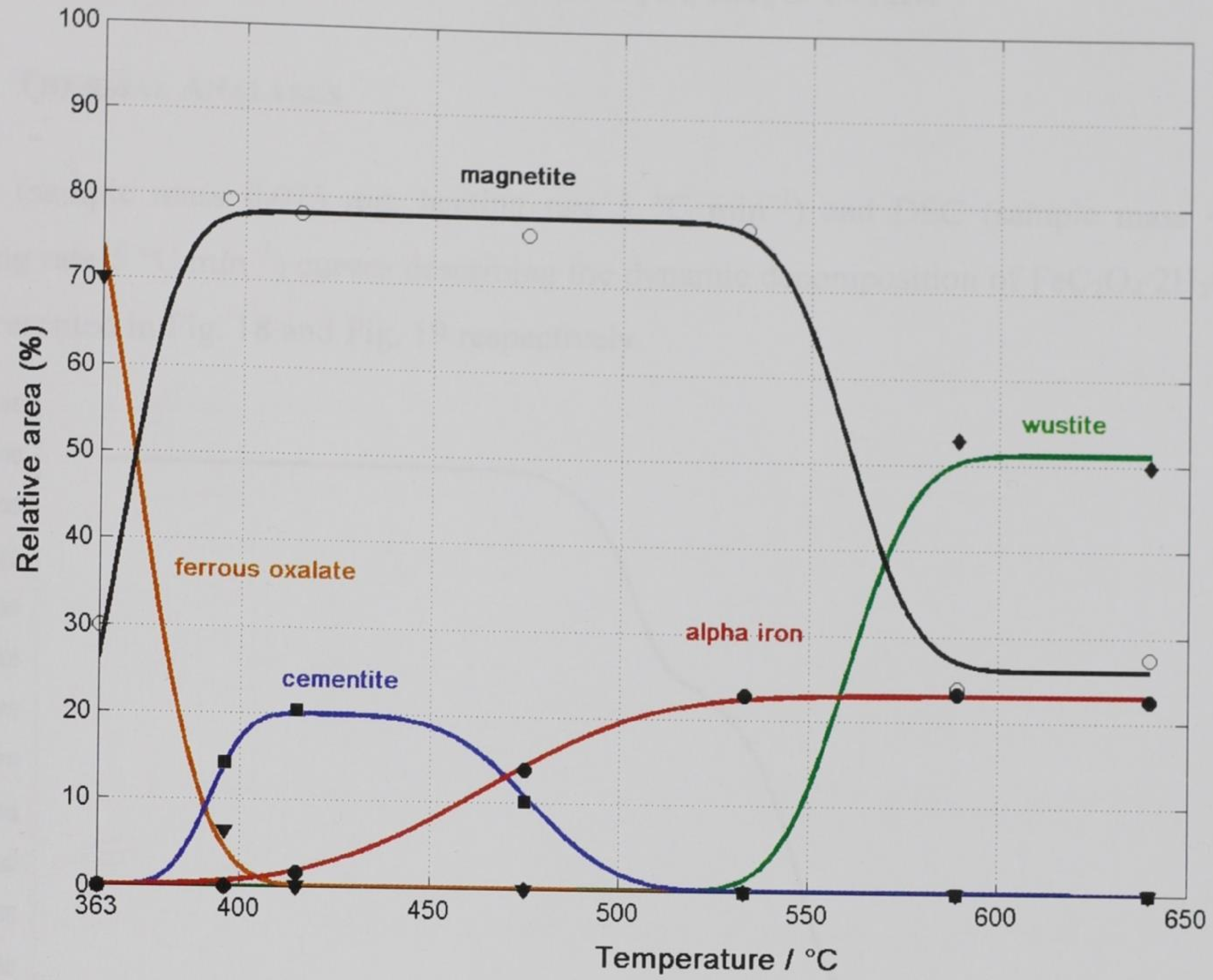

Fig. 17. Temperature dependence of the relative spectrum areas as obtained from Mössbauer spectra of the samples heated between 363 and 640 °C.

5 THERMAL DECOMPOSITION OF $FeC_2O_4 \cdot 2H_2O$ IN AIR

5.1 THERMAL ANALYSES

TGA (sample mass 6.075 mg, heating rate 5 °C min^{-1}) and DSC (sample mass 4.5 mg, heating rate 5 °C min^{-1}) curves describing the dynamic decomposition of $FeC_2O_4 \cdot 2H_2O$ in air are presented in Fig. 18 and Fig. 19 respectively.

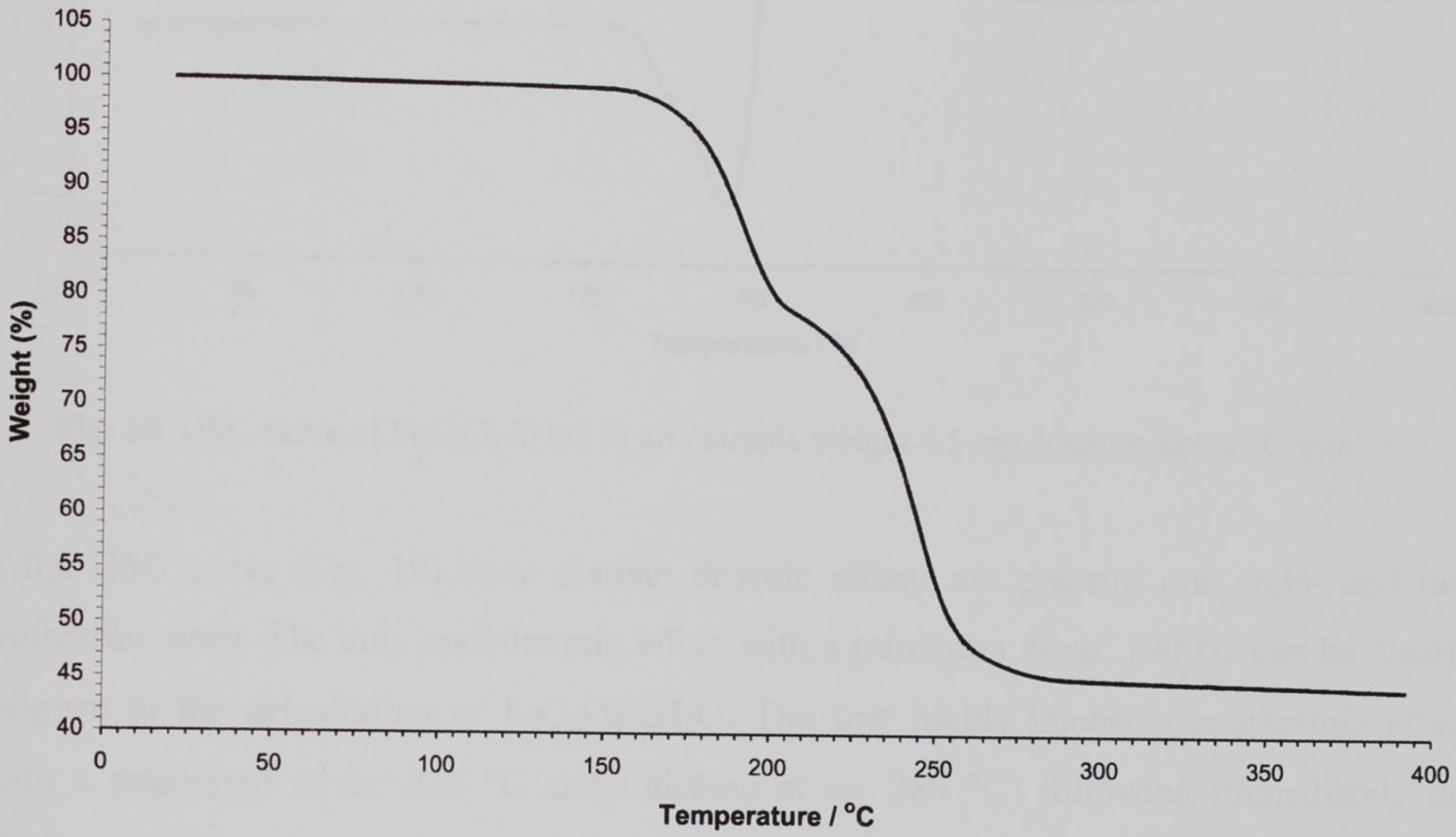

Fig. 18. TGA curve of $FeC_2O_4 \cdot 2H_2O$ in air (sample weight 6.075 mg, heating rate 5 °C min^{-1}).

TGA curve (Fig. 18) shows a continuous mass loss within the temperature interval 153–290 °C with an apparent inflection at about 210 °C. Such character convincingly demonstrates two immediately following processes.

The overall weight loss of 55.6 % matches precisely with the theoretical value of the formation of Fe_2O_3 as the only decomposition product. The weight loss up to the inflection point is 20.1 %, which is in a good agreement with the supposed formation of anhydrous ferrous oxalate as an intermediate decomposition product after the loss of the two water molecules of crystallization (theoretical weight loss 20.0 %).

On the grounds of the TGA results it can be stated that the thermal decomposition of ferrous oxalate dihydrate under air conditions proceeds in two straightforward steps: dehydration (153–208 °C) followed immediately by oxidative decomposition of FeC_2O_4 into Fe_2O_3 (208–290 °C).

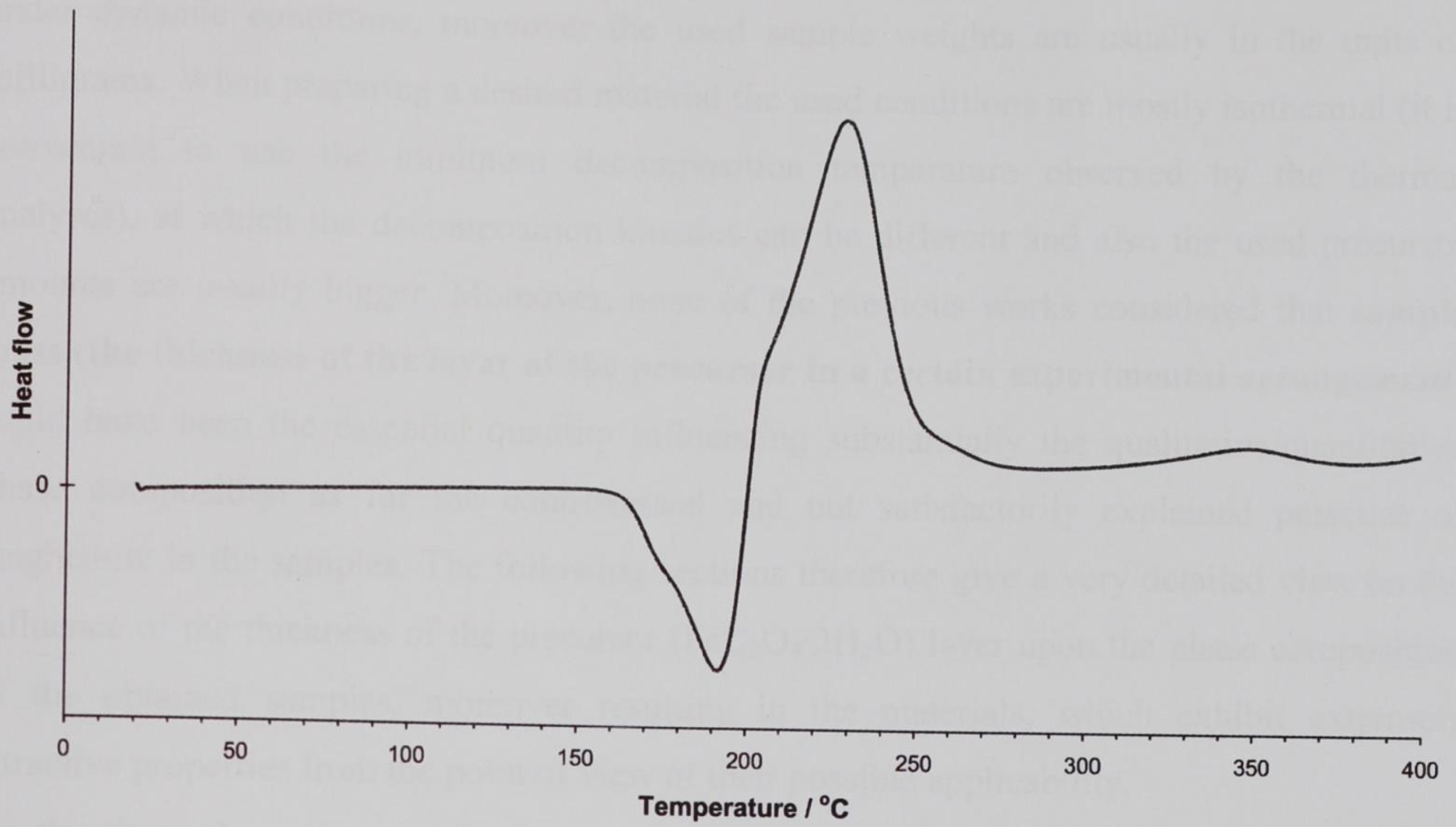

Fig. 19. DSC curve of $FeC_2O_4{\cdot}2H_2O$ in air (sample weight 4.5 mg, heating rate 5 °C min^{-1}).

In the DSC curve (Fig. 19) three distinct thermic effects are present: one endo- and two exothermic ones. The only endothermic effect with a minimum at *ca.* 190 °C can be clearly assigned to the dehydration of $FeC_2O_4{\cdot}2H_2O$. The first highly intensive exothermic effect (with a maximum at *ca.* 230 °C and finishing at *ca.* 280 °C) following immediately the previous endothermic one stands obviously for the oxidative decomposition $FeC_2O_4 \rightarrow Fe_2O_3$. As the nanocrystalline character of primarily formed Fe_2O_3 particles could be expected the second broad (290–380 °C) and far less intensive exothermic effect with a maximum at *ca.* 350 °C could be with a high probability assigned to the gradual crystallization of Fe_2O_3. Such a hypothesis is well supported by the fact that there is no corresponding change in weight in the TGA curve around 350 °C present.

One can easily visualise that the TGA and DSC results corresponds well to each other and indicate that $\mathbf{Fe_2O_3}$ is the only product of the thermal decomposition of $FeC_2O_4{\cdot}2H_2O$ in air. However, one should be aware that the temperature intervals and points ascribed to the mentioned effects could substantially vary with a change of any of the experimental conditions (especially sample weight and heating rate).

The obtained thermal analyses results are so far in a good agreement with those published in the literature and already discussed in Section 3. It should be mentioned, however, that thermal analyses methods give primarily a detailed view on the thermal stability of a material under dynamic conditions, moreover the used sample weights are usually in the units of milligrams. When preparing a desired material the used conditions are mostly isothermal (it is convenient to use the minimum decomposition temperature observed by the thermal analyses), at which the decomposition kinetics can be different and also the used precursor amounts are usually bigger. Moreover, none of the previous works considered that **sample mass (the thickness of the layer of the precursor in a certain experimental arrangement)** could have been the essential quantity influencing substantially the qualitative/quantitative phase composition as for the controversial and not satisfactorily explained presence of maghemite in the samples. The following sections therefore give a very detailed view on the influence of the thickness of the precursor ($FeC_2O_4{\cdot}2H_2O$) layer upon the phase composition of the obtained samples, moreover resulting in the materials, which exhibit extremely attractive properties from the point of view of their possible applicability.

As the thermal analyses methods proved that the decomposition process under dynamic conditions starts slightly above 200 °C, one should ask the question why the further described isothermal experiments were already carried out at 175 °C, ergo rather far below it? The reason is very clear – it is well known fact that the lower the set temperature is the slower the process proceeds and the smaller particles of the nascent solid phases are. As this research has been primarily focused on the preparation of nanoparticles of iron oxides, the set of such a low decomposition temperature seems to be very logic.

5.2 SAMPLE PREPARATION AND EXPERIMENTAL ARRANGEMENT

Before the thermal treatment, $FeC_2O_4{\cdot}2H_2O$ powder (Sigma Aldrich) was finely homogenized in an agate mortar. Samples of different weights were isothermally treated in a ceramic crucible (bottom diameter *ca.* 23 mm, capacity 7.26 ml) inside a laboratory muffle furnace (LM 112.07, Linn High Therm GmbH) at a set temperature of 175 °C. Sample temperature was continually monitored by a Ni-Cr-Ni thermocouple (GTT101000, Greisinger electronic GmbH), which was in direct contact with the underside of the crucible, and recorded using a digital multimeter (M−3850D, Metex Instruments) connected to a PC (Fig. 20).

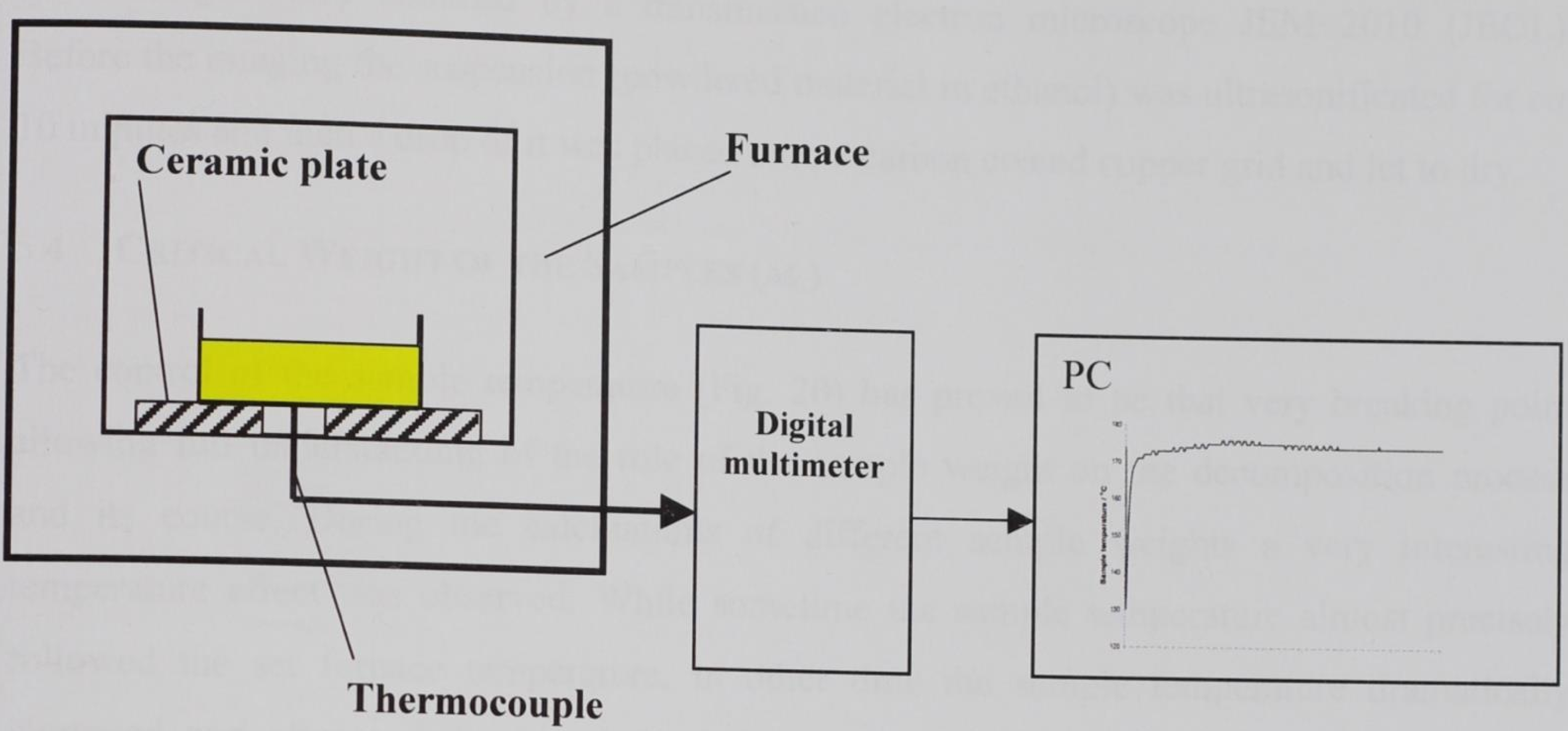

Fig. 20. Experimental arrangement of the system used to the study of the thermal decomposition of $FeC_2O_4{\cdot}2H_2O$ in air.

5.3 Experimental Methods

Solid decomposition products of as-treated samples were identified by Mössbauer spectroscopy and X-ray powder diffraction (XRD). Transmission ^{57}Fe Mössbauer spectra were collected using a Mössbauer spectrometer in constant acceleration mode with a ^{57}Co(Rh) source. The measurements were carried out at 300 and 5 K using a cryomagnetic system of Oxford Instruments. XRD patterns were recorded using a Philips X'Pert MPD device with CoKα radiation and equipped with primary monochromator and X'Celerator detector. Powdered samples were spread on silicon slides and step-scanned within the angular range 10–120° (in conventional 2Θ geometry) with a step of 0.008°. Particle size (height in *z*-axis) of the samples was evaluated from AFM images obtained by using an atomic force microscope (Explorer, ThermoMicroscopes). AFM analyses were performed at room temperature in air in a non-contact mode with silicon tips (1650-00 type). Before the AFM measurement the powder samples were ultrasonificated in distilled water at *ca.* 40 °C for 30 min and then dripped onto a mica slide (1.5 × 1.5 cm) and dried at 45 °C for another 30 min. Specific surface areas of the samples were measured by the BET method using a Sorptomatic 1990 (ThermoFinnigan). Before the actual measurement the samples were pre-evacuated for *ca.* 20 hrs at RT at a pressure less than 0.1 Pa.

TEM images were obtained by a transmission electron microscope JEM–2010 (JEOL). Before the imaging the suspension (powdered material in ethanol) was ultrasonificated for *ca.* 10 minutes and then a drop of it was placed onto a carbon coated copper grid and let to dry.

5.4 CRITICAL WEIGHT OF THE SAMPLES (m_C)

The control of the sample temperature (Fig. 20) has proved to be that very breaking point allowing full understanding of the role of the sample weight on the decomposition process and its course. During the calcinations of different sample weights a very interesting temperature effect was observed. While sometime the sample temperature almost precisely followed the set furnace temperature, in other time the sample temperature dramatically increased and after a distinct period of time decreased back to the temperature baseline (furnace temperature of 175 °C). Such effects appeared to be precisely dependent upon the sample weight and in our experimental arrangement (the shape and volume of the ceramic crucible) the critical sample weight m_c, below which no distinct temperature increase was observed, appeared to be *ca.* 1600 mg. The situation is well demonstrated in Fig. 21 showing the temperature record of two representative samples, one below m_c (blue curve) and the other above m_c (red curve) of $FeC_2O_4{\cdot}2H_2O$.

On the grounds of such controversial temperature records one could be naturally curious about how as-prepared samples differ from each other and by what factor the temperature effect has been caused. Hence, in the following sections the phase composition, some interesting properties and possible applicability of the low- and high-layer samples are discussed in detail.

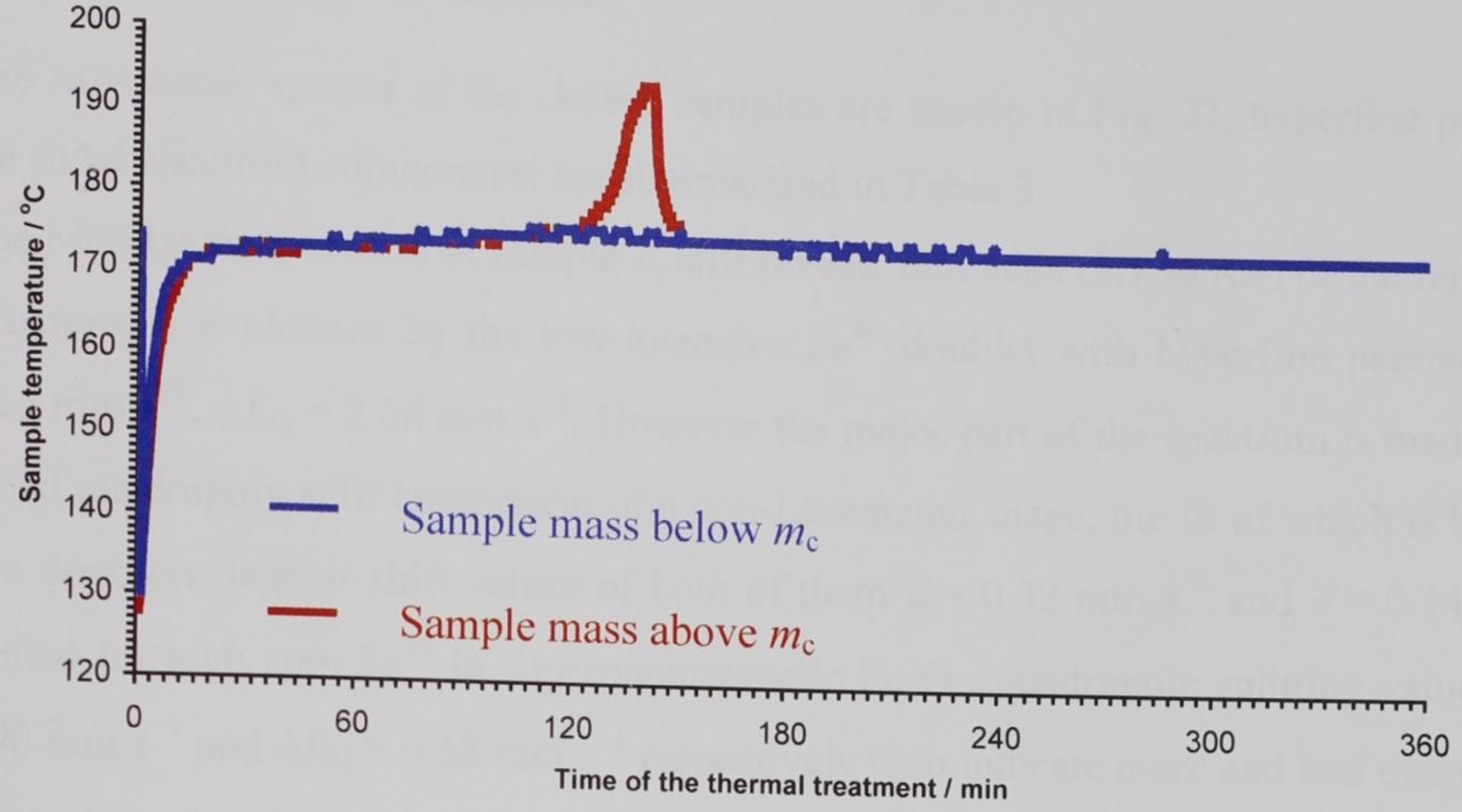

Fig. 21. Temperature records of a sample below and above a critical weight m_c taken during the isothermal treatment of $FeC_2O_4{\cdot}2H_2O$ at 175 °C.

5.5 LOW-LAYER SAMPLES

It is apparent that in the case of the low-layer sample (Fig. 21, below m_c) the sample temperature almost precisely follows the set furnace temperature (the short-time temperature growths and falls relate to the temperature regulation). There is, however, a long-time (within *ca.* 100–250 min of the calcination time) but very low (1 °C) temperature increase visible.

To investigate what happens with the low-layer sample during the time, a set of isothermal calcinations for different periods of time (4.5, 6, 8, 10, 12, 17, 30, 48, 64 and 100 hrs) at 175 °C was carried out. As it has been already mentioned that the critical weight of the precursor proved to be *ca.* 1600 mg, a weight of 1000 mg of ferrous oxalate dihydrate representing low-layer samples has been chosen. The phase composition of as-prepared samples was investigated by Mössbauer spectroscopy and XRD and is discussed in the following sections. Marking of the samples and the conditions at which the samples were isothermally treated are summarized in Table 2.

Table 2 The conditions at which low-layer (below m_c) samples A–J were calcined.

$FeC_2O_4{\cdot}2H_2O$, sample mass 1000 mg, furnace temperature 175 °C										
Sample	**A**	**B**	**C**	**D**	**E**	**F**	**G**	**H**	**I**	**J**
Calcination time	4.5	6	8	10	12	17	30	48	64	100

5.5.1 *MÖSSBAUER SPECTROSCOPY*

The Mössbauer spectra of the chosen samples are shown in Fig. 22, hyperfine parameters of the fitted spectrum components are summarized in Table 3.

The Mössbauer spectrum of sample A still reveals remnants (5.1 % R*A*) of the ferrous oxalate structure as evidenced by the low-intensive Fe^{2+} doublet with hyperfine parameters of δ = 1.16 mm s^{-1}, ΔE_Q = 2.06 mm s^{-1}. However the major part of the spectrum is made of a rather broad quadrupoly split component of a non-Lorentzian shape, the fit of which is best made of two doublets. Isomer shift values of both of them δ = 0.32 mm s^{-1} and δ = 0.34 mm s^{-1} are typical for high spin Fe^{3+} in superparamagnetic Fe_2O_3, quadrupole splitting values of ΔE_Q = 1.90 mm s^{-1} and ΔE_Q = 0.68 mm s^{-1} respectively then indicate more and less distorted oxygen octahedrons (environments of Fe atoms) respectively.

The Mössbauer spectra of samples B–F are almost the same in their shape (rather broad non-Lorentzian doublets) and phase composition; they do not reveal presence of FeC_2O_4 any more and are fitted by two Fe^{3+} doublets exhibiting substantially different values of quadrupole splitting similarly as in sample A. The Mössbauer spectrum of sample D in Fig. 22 serves as a representative spectrum illustrating the phase composition of samples B–F.

The Mössbauer spectrum of sample G reveals besides the central superparamagnetic component, which is now fitted by only one Fe^{3+} doublet, a magnetically split pattern fitted by two sextets. The magnetically more split one with hyperfine parameters of δ = 0.37 mm s^{-1}, ε_Q = −0.21 mm s^{-1}, H = 46.8 T can be clearly assigned to the not fully crystalline bulk parts of α-Fe_2O_3. Just the table values of isomer and quadrupole shifts allow to identify a hematite structure, substantially reduced value of hyperfine magnetic field and rather broad linewidths indicate then low degree of crystallinity. The second, rather broad magnetically split component reveals hyperfine parameters of δ = 0.32 mm s^{-1}, ε_Q = −0.17 mm s^{-1} and H = 41.1 T. It can be clearly seen that some of those parameters are close but fairly shift to the lower values when compared to the previous ones typical for bulk hematite; such behaviour is characteristic for surface parts of very small particles and the sextet component can be therefore assigned to the surface of ultrafine hematite particles.

The Mössbauer spectra of samples H, I and J reveal qualitatively the same phase composition as the previous sample (G), there is however apparent a gradual change in the relative proportions of individual components. One can readily visualise that the relative content of the mid superparamagnetic Fe_2O_3 gradually decreases with increasing calcination time in favour of both surface and bulk parts of hematite particles (28.3 % in sample H *vs.* 93.4 % in sample J). There is also obvious gradual crystallization and growing of hematite particles as evidenced by the increasing values of hyperfine magnetic fields of both sextets, simultaneous mutual approach of the corresponding lines and narrowing of the linewidths.

It is worth mentioning that no Mössbauer spectrum gives any evidence for crystalline γ-Fe_2O_3.

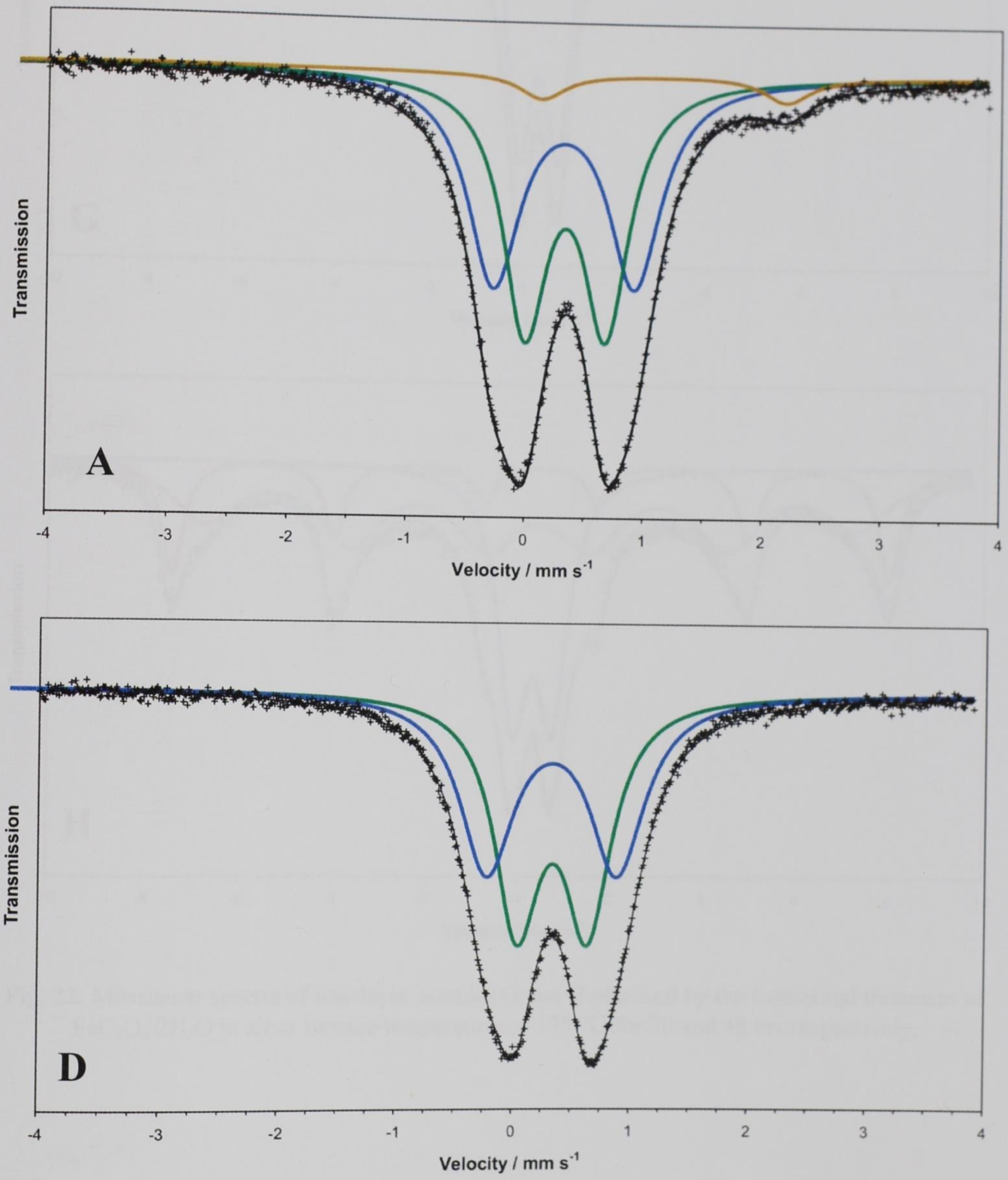

Fig. 22. Mössbauer spectra of low-layer samples A and D obtained by the isothermal treatment of $FeC_2O_4 \cdot 2H_2O$ in air at furnace temperature of 175 °C for 4.5 and 10 hrs respectively.

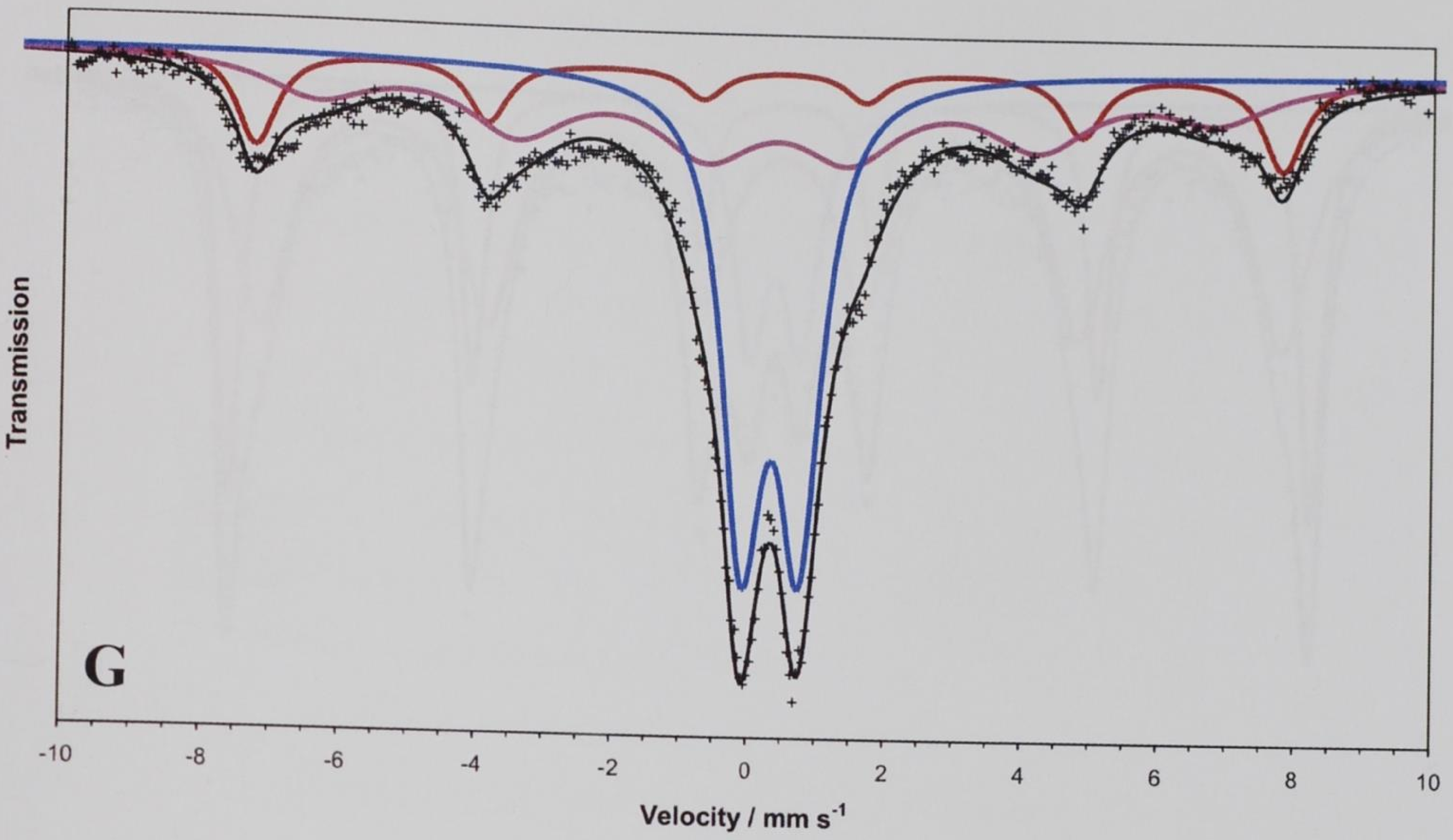

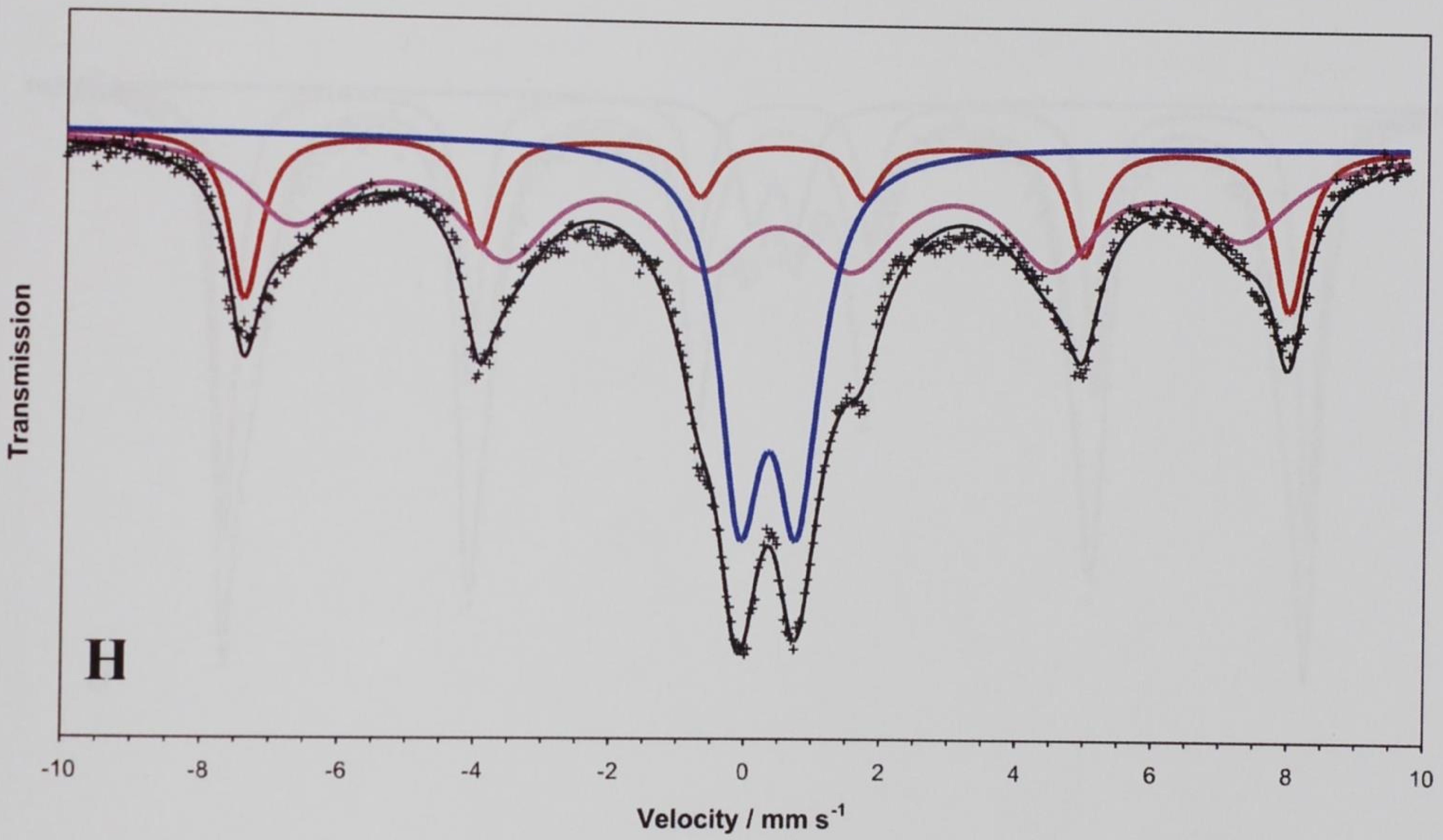

Fig. 22. Mössbauer spectra of low-layer samples G and H obtained by the isothermal treatment of $FeC_2O_4{\cdot}2H_2O$ in air at furnace temperature of 175 °C for 30 and 48 hrs respectively.

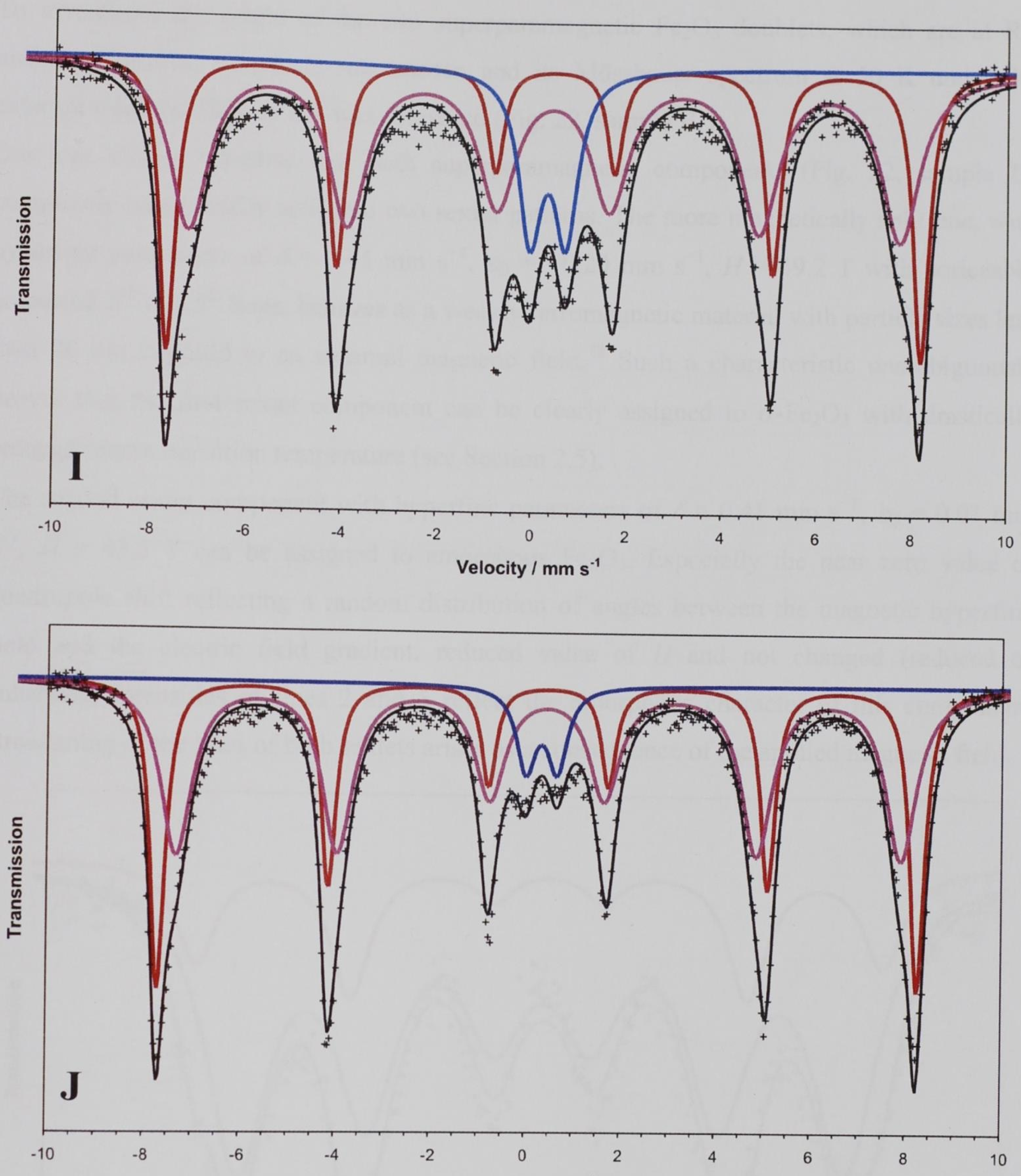

Fig. 22. Mössbauer spectra of low-layer samples I and J obtained by the isothermal treatment of $FeC_2O_4 \cdot 2H_2O$ in air at furnace temperature of 175 °C for 64 and 100 hrs respectively.

To investigate the origin of the two superparamagnetic Fe_2O_3 doublets, which are at RT undistinguishable, sample E was chosen and its Mössbauer spectrum at 50 K under the external magnetic field of 6 T was measured (Fig. 22, sample E_1).

One can clearly visualise that both superparamagnetic components (Fig. 22, sample D) completely magnetically split into two sextet patterns. The more magnetically split one, with hyperfine parameters of $\delta = 0.45$ mm s^{-1}, $\varepsilon_Q = -0.20$ mm s^{-1}, $H = 49.2$ T with noticeably enhanced 2nd and 5th lines, behaves as a weakly ferromagnetic material with particle sizes less than 20 nm exposed to an external magnetic field.[73] Such a characteristic unambiguously proves that the first sextet component can be clearly assigned to α-Fe_2O_3 with drastically reduced Morin transition temperature (see Section 2.5).

The second sextet component with hyperfine parameters of $\delta = 0.41$ mm s^{-1}, $\varepsilon_Q = 0.01$ mm s^{-1}, $H = 43.5$ T can be assigned to amorphous Fe_2O_3. Especially the near zero value of quadrupole shift reflecting a random distribution of angles between the magnetic hyperfine field and the electric field gradient, reduced value of H and not changed (reduced or enhanced) intensities of lines 2 and 5 reflect the amorphous character of this component. Broadening of the lines of both sextets arises as a consequence of the applied magnetic field.

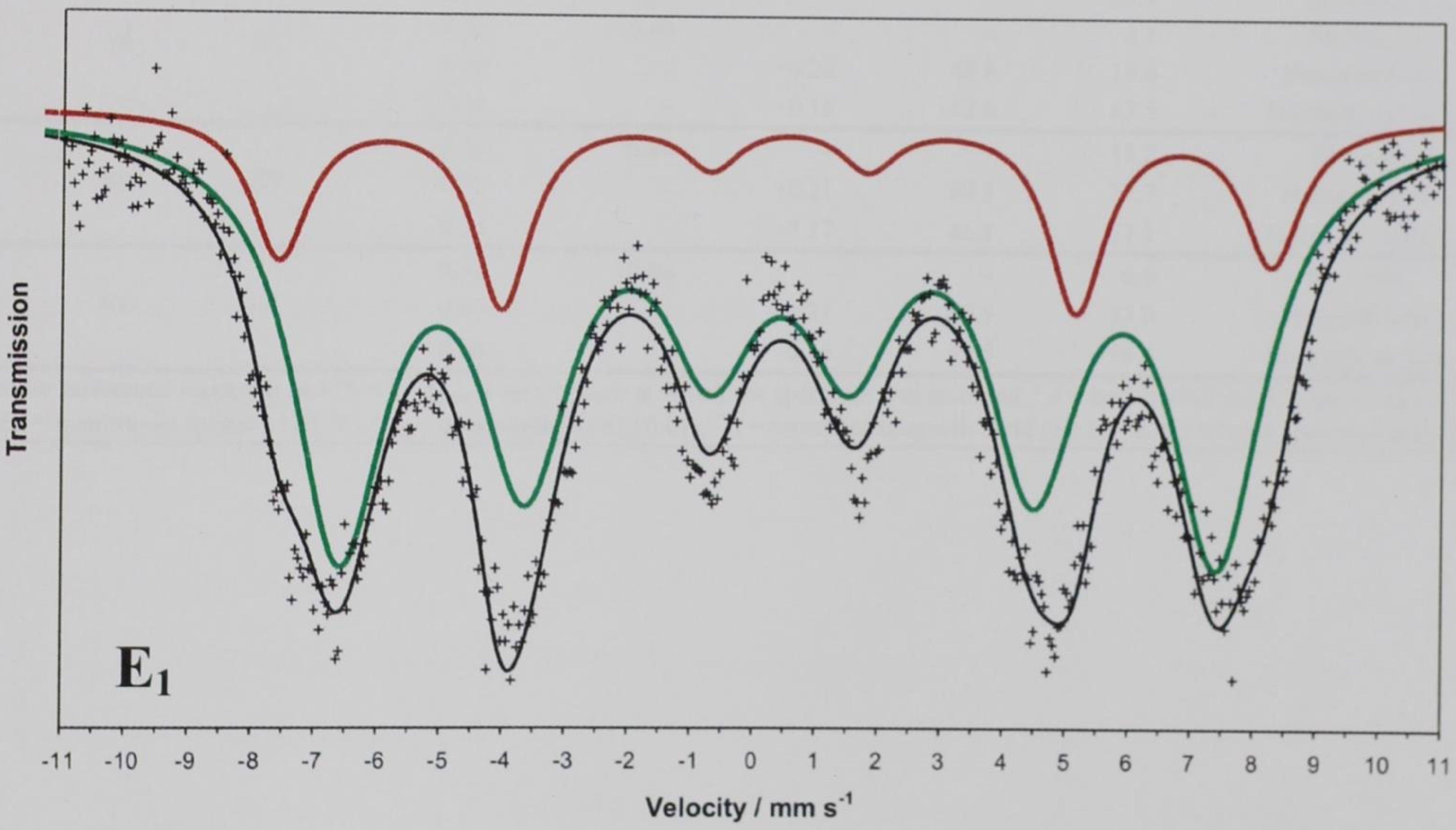

Fig. 22. Mössbauer spectrum of sample E_1 (low-layer sample E measured at 50 K under the external magnetic field of 6 T).

Table 3 Mössbauer parameters of samples A, B, C, D, E, E_1, F, G, H, I and J.

Sample	t/min[a]	T_{samp}/°C[b]	δ/mm s^{-1}[c]	ΔE_Q/mm s^{-1}[d]	ε_Q/mm s^{-1}[e]	H/T[f]	RA (%)[g]	Site assignment
A	4.5	RT	1.16	2.06	–	–	5.1	Ferrous oxalate dihydrate
			0.32	1.19	–	–	47.0	SP Fe_2O_3
			0.34	0.68			47.9	SP Fe_2O_3
B	6	RT	0.32	1.14	–	–	52.3	SP Fe_2O_3
			0.34	0.63	–	–	47.7	SP Fe_2O_3
C	8	RT	0.34	1.14	–	–	44.8	SP Fe_2O_3
			0.34	0.64	–	–	55.2	SP Fe_2O_3
D	10	RT	0.33	1.11	–	–	48.0	SP Fe_2O_3
			0.33	0.60	–	–	52.0	SP Fe_2O_3
E	12	RT	0.32	1.16	–	–	41.9	SP Fe_2O_3
			0.33	0.64	–	–	58.1	SP Fe_2O_3
E_1	12	50 K / 6 T	0.45	–	−0.20	49.2	21.6	α-Fe_2O_3
			0.41	–	0.01	43.5	78.4	am-Fe_2O_3
F	17	RT	0.31	1.13	–	–	46.5	SP Fe_2O_3
			0.33	0.63	–	–	53.5	SP Fe_2O_3
G	30	RT	0.32	1.02	–	–	30.8	SP Fe_2O_3
			0.34	0.62	–	–	11.7	SP Fe_2O_3
			0.37	–	−0.21	46.8	16.6	Hematite bulk
			0.32	–	−0.17	41.1	40.9	Hematite surface
H	48	RT	0.33	0.93	–	–	25.9	SP Fe_2O_3
			0.35	0.60	–	–	3.1	SP Fe_2O_3
			0.38	–	−0.20	47.8	19.6	Hematite bulk
			0.35	–	−0.16	42.6	43.5	Hematite surface
I	64	RT	0.32	0.80	–	–	15.2	SP Fe_2O_3
			0.37	–	−0.21	49.3	27.7	Hematite bulk
			0.35	–	−0.17	46.8	57.1	Hematite surface
J	100	RT	0.32	0.66	–	–	6.6	SP Fe_2O_3
			0.37	–	−0.21	49.5	37.0	Hematite bulk
			0.36	–	−0.16	47.3	56.4	Hematite surface

[a] t = time of the isothermal treatment at 175 °C, [b] T_{meas} = temperature at which the spectrum was recorded, [c] δ = isomer shift (with respect to metallic iron, ±0.01), [d] ΔE_Q = quadrupole splitting (±0.01), [e] ε_Q = quadrupole shift (±0.01), [f] H = hyperfine magnetic field (±0.1), [g] RA = relative spectrum area (±0.2).

5.5.2 ***XRD DATA***

XRD data only confirm the phase composition observed by Mössbauer spectroscopy. The patterns of chosen samples are presented in Fig. 23.

Samples A, B and C reveal almost the same character – they represent a mixture of the amorphous/XRD-amorphous material with remnants of the not completely decomposed oxalate structure, which are represented by four distinct diffraction lines (marked O in Fig. 23) of the highest relative intensities I/I_0 of 90, 100, 80 and 90 % respectively. It is apparent that with increasing calcination time the contribution of FeC_2O_4 is lower and one can also visualize the gradual beginning of the crystallization process of the amorphous material, the pattern of which starts to be gradually more resolved and gives impression of separated although very broad diffraction lines. The fact that only the most intensive diffraction peaks of ferrous oxalate are present in predominantly amorphous pattern indicates that the content of undecomposed FeC_2O_4 in the samples is extremely low, which is in a good agreement with the Mössbauer spectra discussed in the previous section.

The XRD pattern of sample D shows that FeC_2O_4 is no more present in the sample. All extremely broad diffraction lines can be assigned exclusively to the α-Fe_2O_3 structure in the very beginning of its formation.

The XRD patterns of samples E (not shown), F, G and H (not shown) exhibit the gradual crystallization of the hematite structure, the diffraction lines of which are better resolved, narrower and more intensive with increasing calcination time.

The XRD patterns of the samples isothermally treated for 64 (I, not shown) and 100 hrs (J) are already typical for rather crystalline samples; the broadened lines suggest however not yet perfectly developed crystal structure, which can be naturally expected due to a very low calcination temperature (175 °C).

It is worth mentioning that similarly to the Mössbauer data neither of the above-mentioned samples revealed any presence of γ-Fe_2O_3. Especially the absence of a diffraction line at 35.301 2Θ representing an independently standing (without any overlap with hematite diffraction lines) diffraction line of an intensity 30 % (I/I_0) of maghemite unambiguously excludes its presence in a sample.

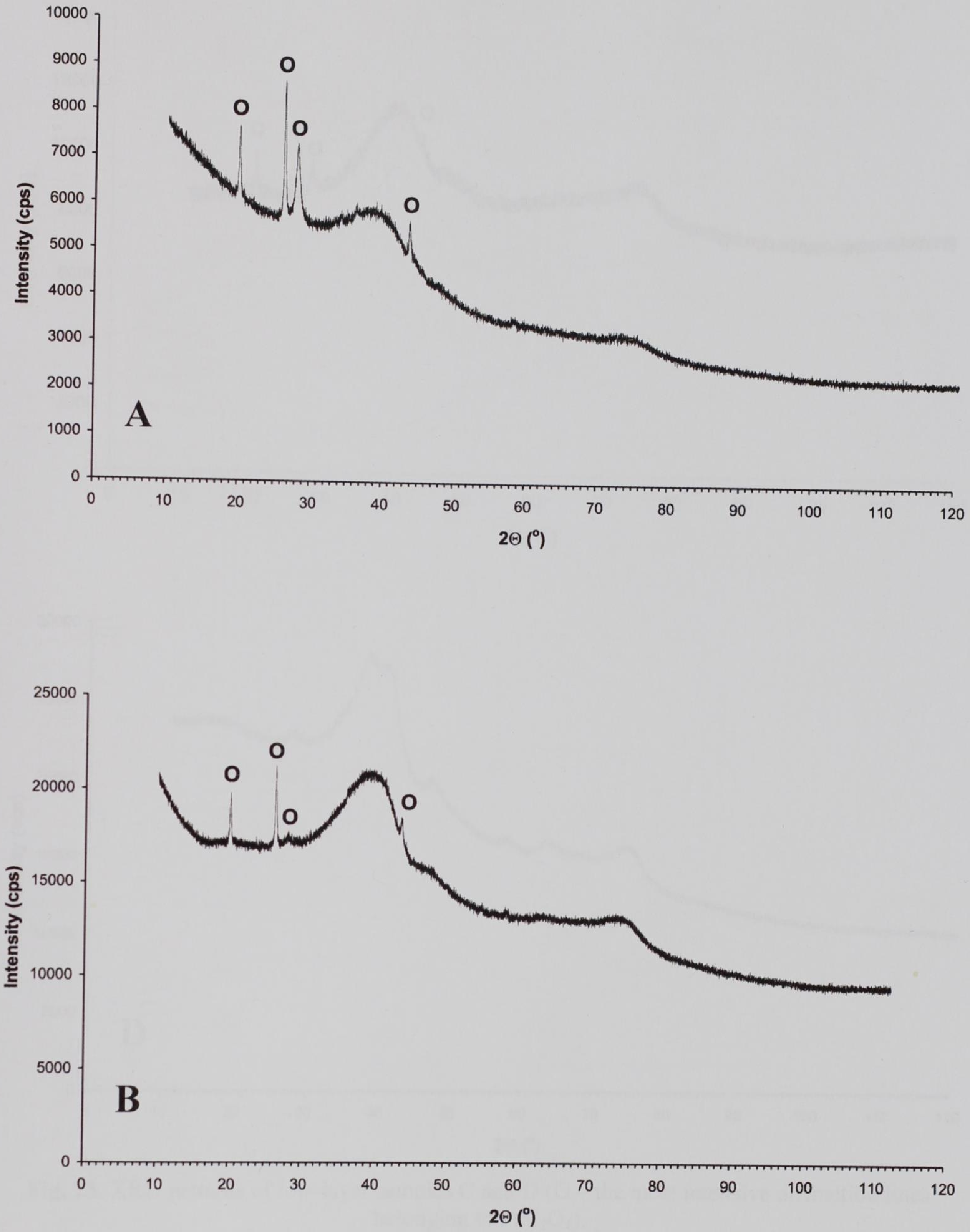

Fig. 23. XRD patterns of low-layer samples A and B (O – the most intensive diffraction lines belonging to FeC_2O_4).

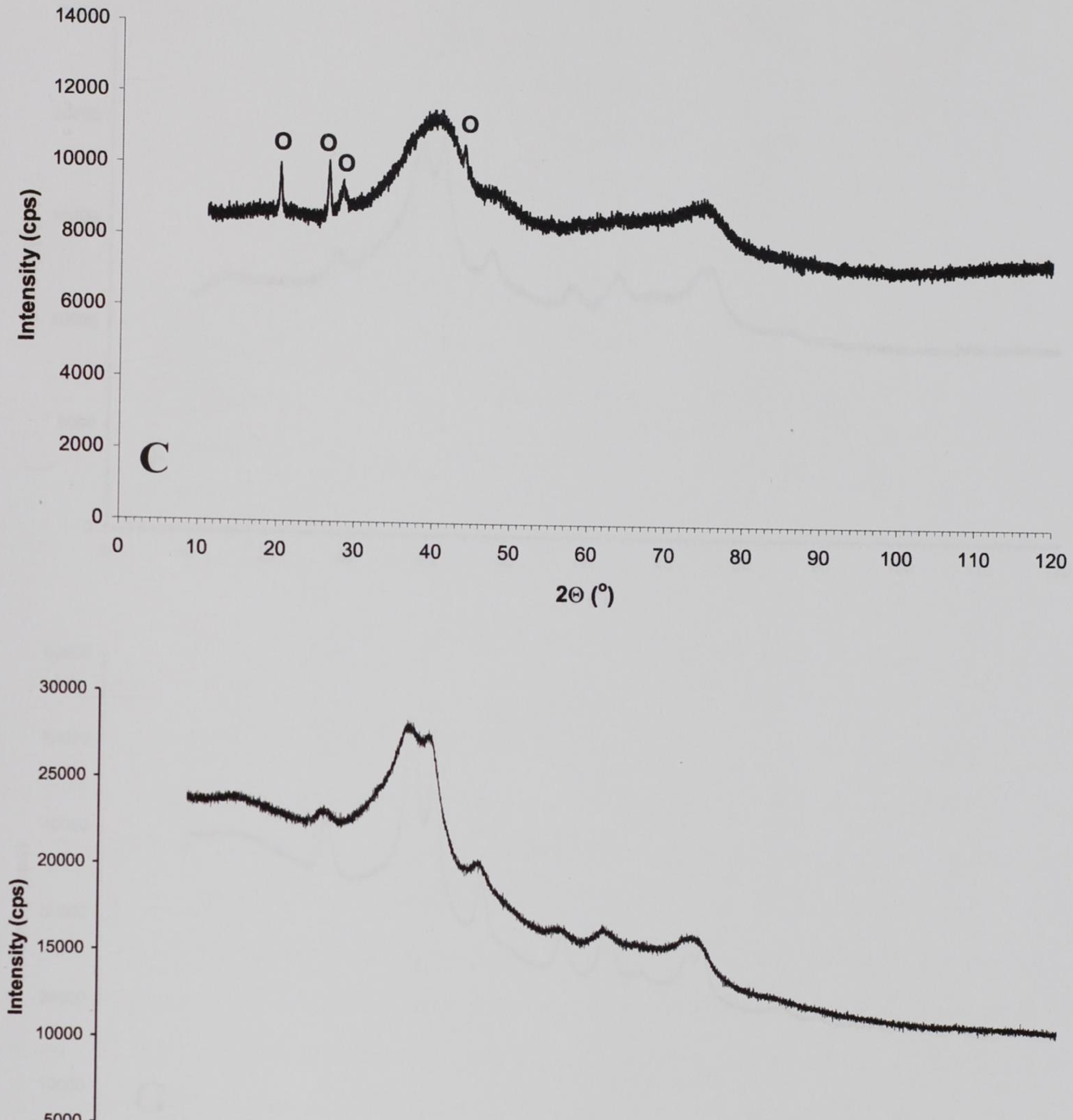

Fig. 23. XRD patterns of low-layer samples C and D (O – the most intensive diffraction lines belonging to FeC_2O_4).

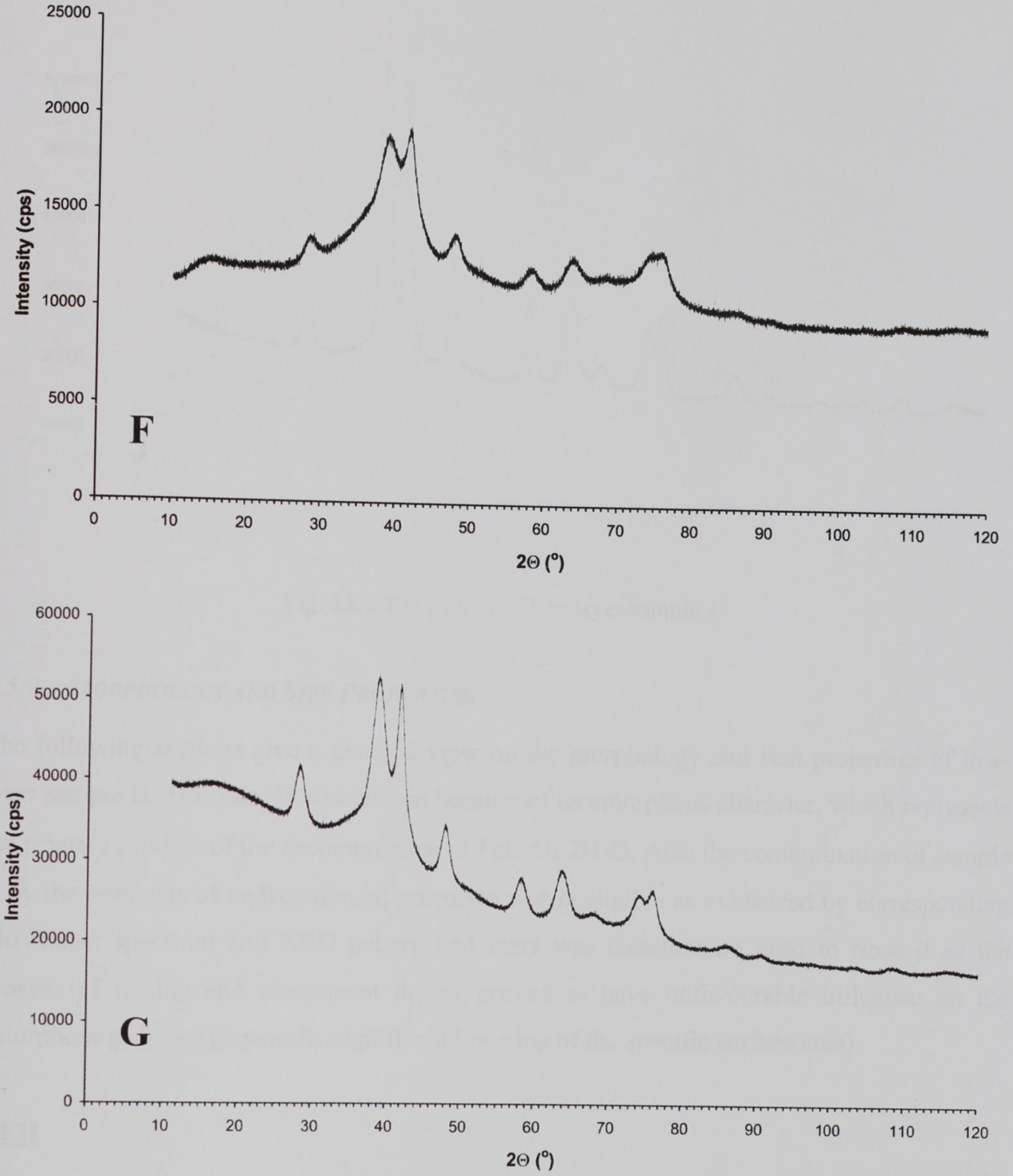

Fig. 23. XRD patterns of low-layer samples F and G.

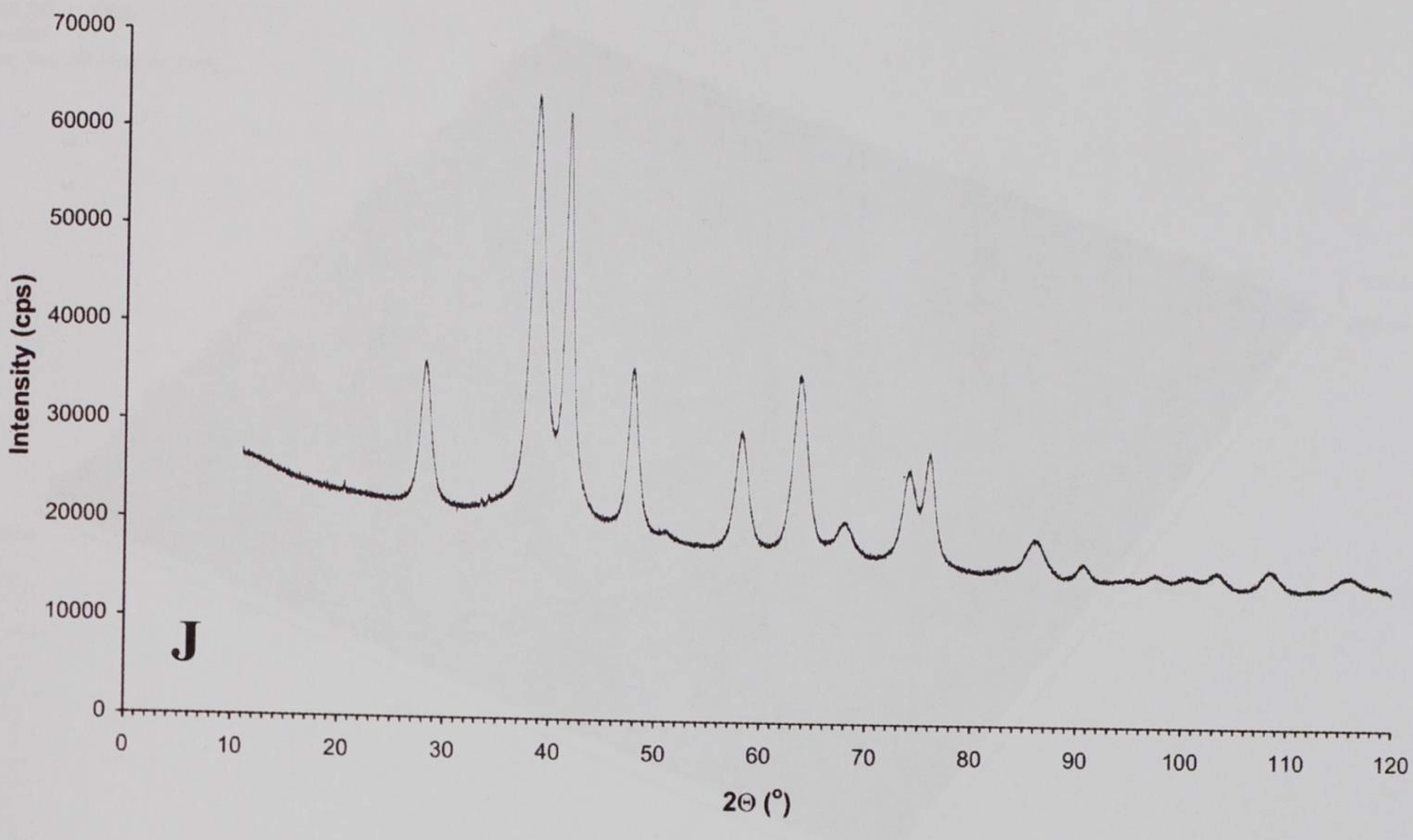

Fig. 23. XRD pattern of low-layer sample J.

5.5.3 *MORPHOLOGY AND SIZE PROPERTIES*

The following sections give a detailed view on the morphology and size properties of low-layer sample B. This sample was chosen because of its amorphous character, which represents the primary product of the decomposition of $FeC_2O_4{\cdot}2H_2O$. Also the contamination of sample B by the remnants of undecomposed precursor was negligible as evidenced by corresponding Mössbauer spectrum and XRD pattern and there was therefore no need to rinse it as the process of rinsing and consequent drying proved to have unfavourable influence on the amorphous particles (especially significant lowering of the specific surface area).

AFM

AFM image of sample B is presented in Fig. 24. The image displays a large number of very small particles of almost uniform size in *z*-axis ranging within 1.5–2 nm. This result corresponds closely with the Mössbauer and XRD data and suggests the very beginning of the creation of amorphous Fe_2O_3 nanoparticles from the FeC_2O_4 structure.

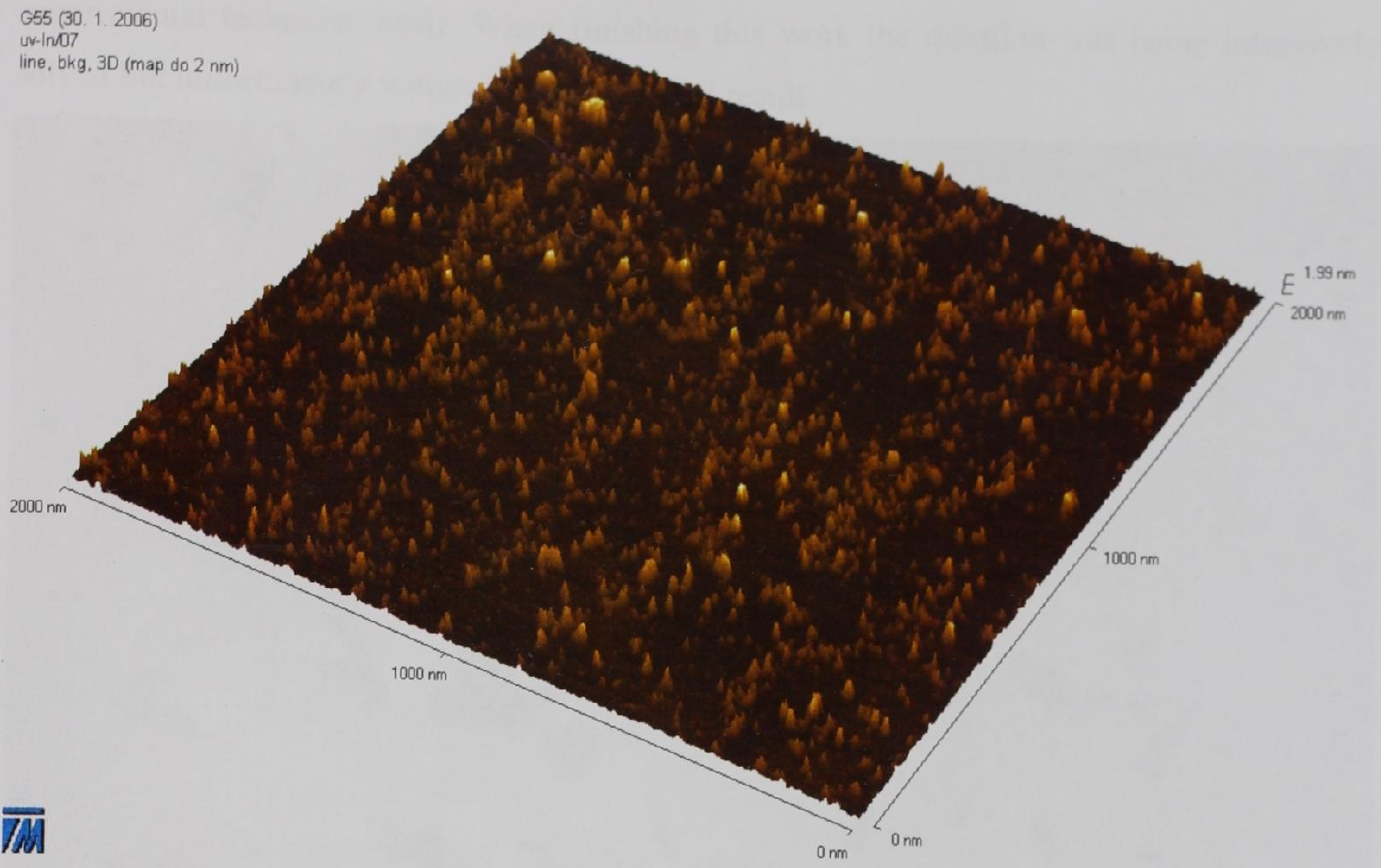

Fig. 24. AFM image of sample B.

TEM

First it should be noted that TEM results rather differ from those obtained by AFM especially from the viewpoint of the whole character of the investigated sample. While AFM image shows well separated particles (Fig. 24), TEM image on the other hand exhibits large objects of ferrous oxalate morphology (sticks, flakes of various sizes; see Fig. 25) the surface of which is covered by a texture as obvious in Fig. 26. When magnified the texture proves to be made of very small predominantly ***spherical*** particles (Fig. 27) with uniform dimensions of about 3 nm in diameter. This result supports well the **dimensions** observed by AFM and indirectly agrees well with the Mössbauer and XRD data, which evidence a predominant proportion of superparamagnetic and amorphous material in sample B respectively. For comparison, Fig. 28 shows a TEM image of sample I, the whole character of which proves to be the same as that of sample B (Figs. 25 and 26). Only the sizes of spherical particles making the texture of the large objects are bigger (*ca.* 10 nm) well confirming the observed process of crystallization within the whole volume of these ferrous oxalate-like-shape objects.

The question is what causes such a dramatic difference between AFM and TEM results concerning the sample character, whether different sample preparation or the principle of the experimental technique itself. When finishing this work the question was being intensively solved but unfortunately without an unequivocal result.

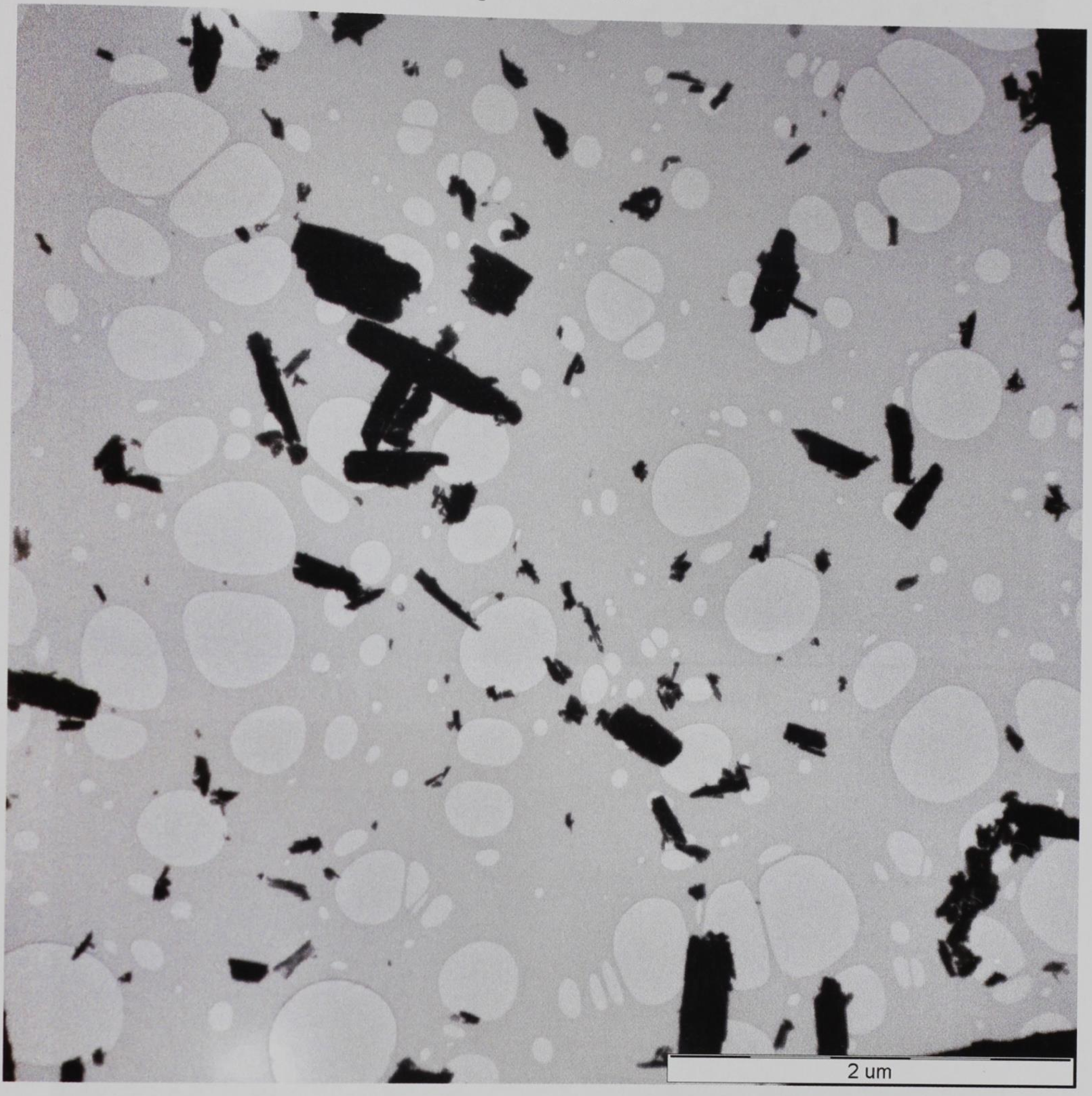

Fig. 25. TEM image of low-layer sample B. An overall view.

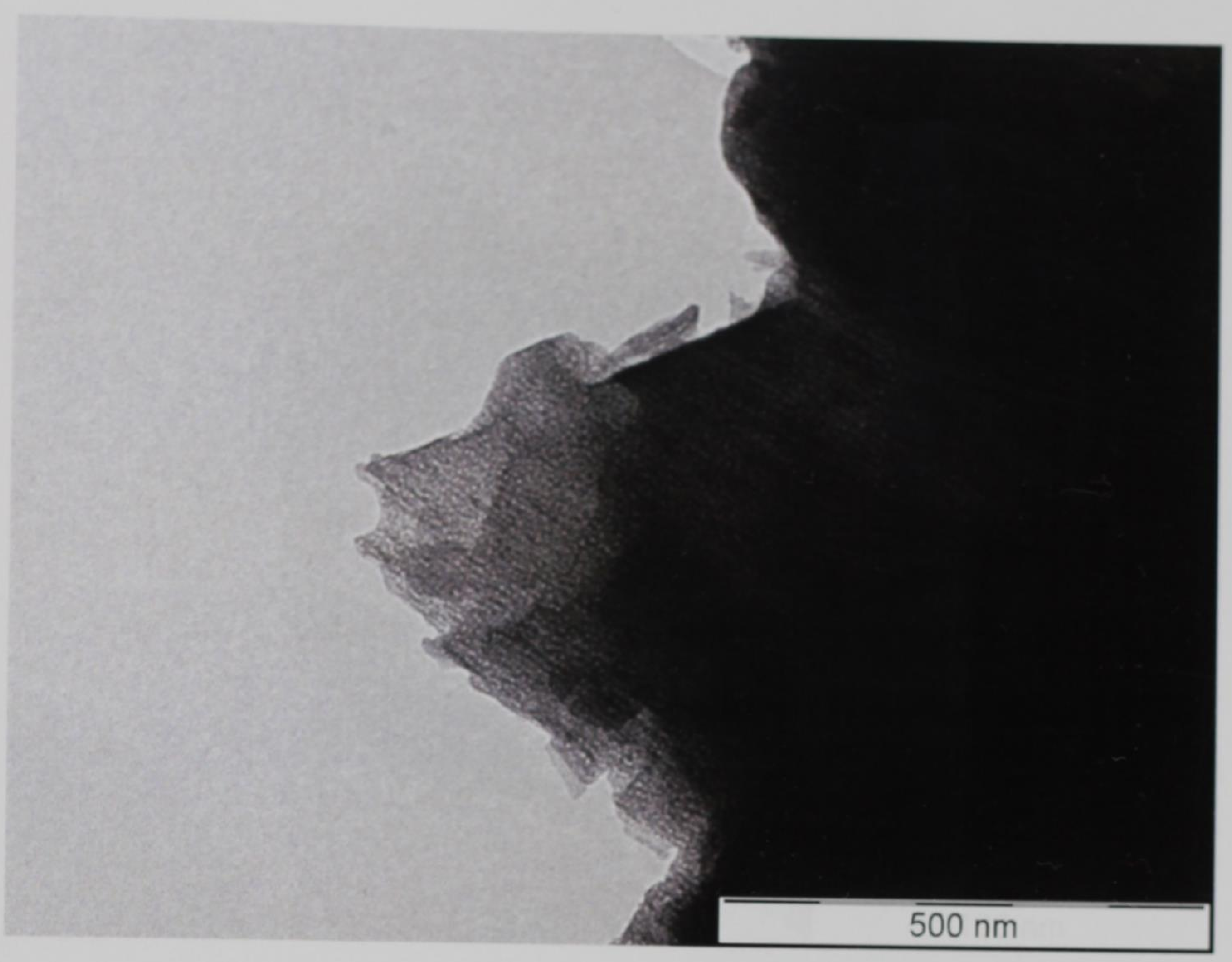

Fig. 26. TEM image of low-layer sample B.

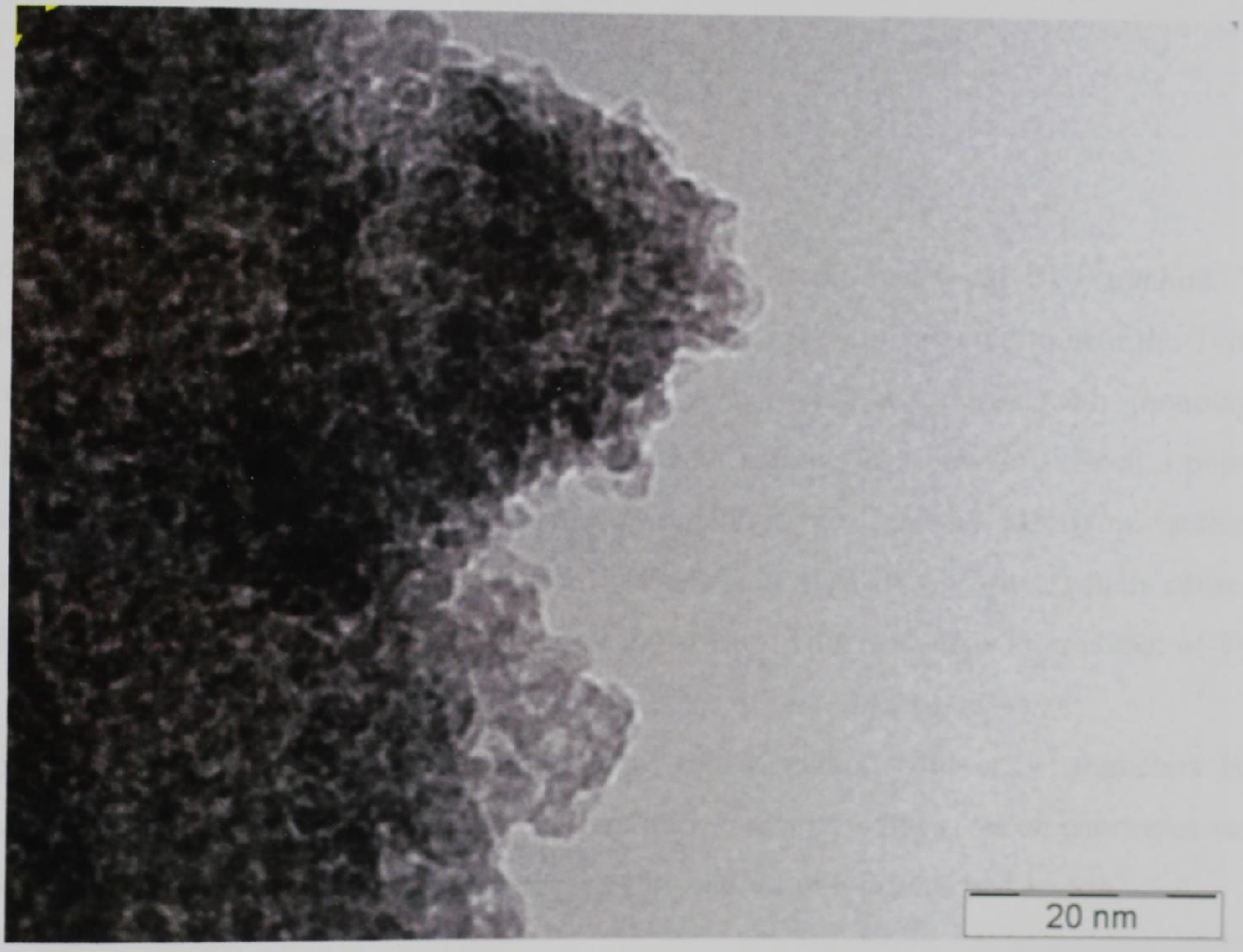

Fig. 27. TEM image of low-layer sample B. Maximum magnitude.

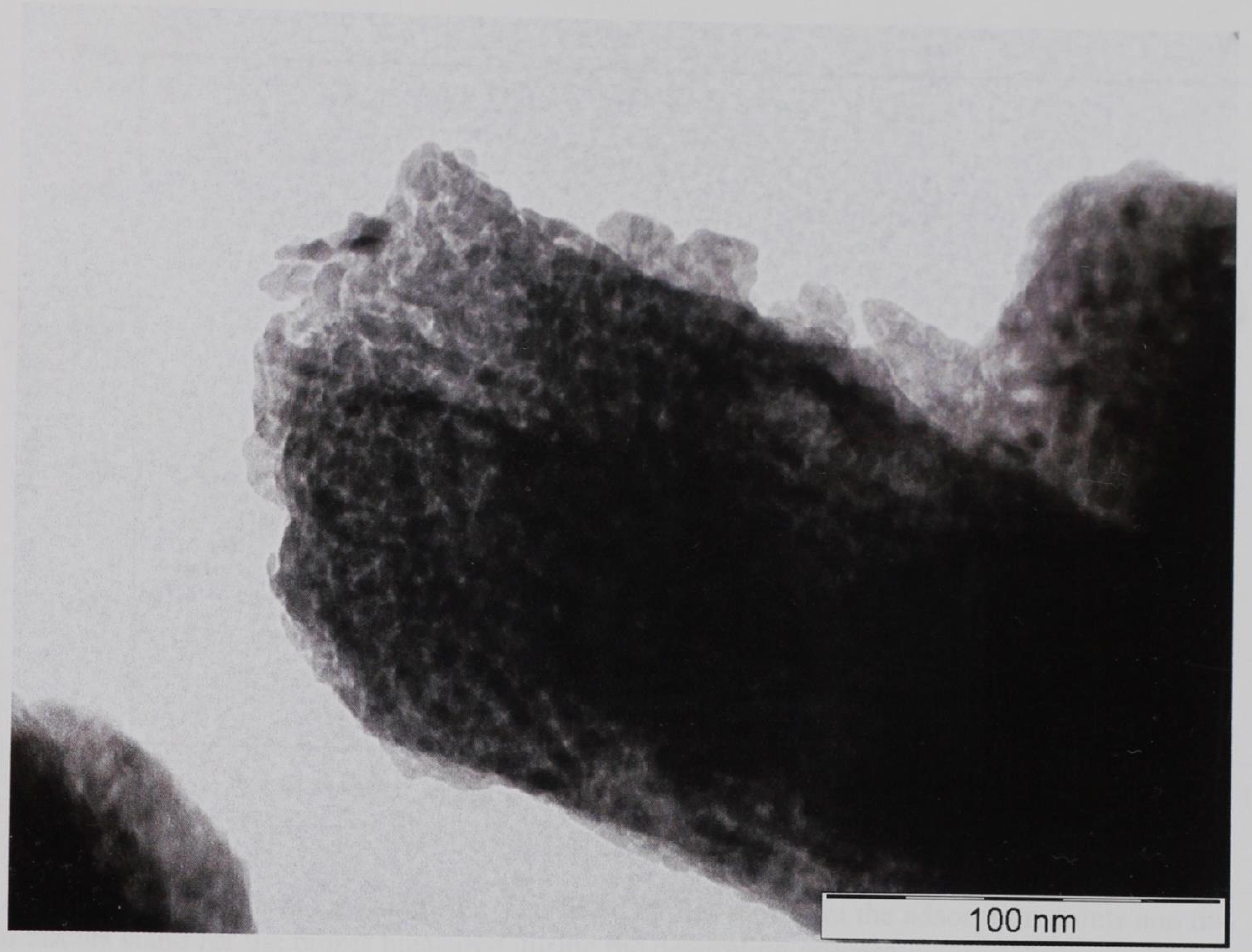

Fig. 28. TEM image of low-layer sample I.

SPECIFIC SURFACE AREA

The specific surface area of sample B was measured by conventional BET method. The adsorption/desorption isotherm is given in Fig. 29. The shape of the isotherm is of the Type II according to the IUPAC classification, which is normally associated with monolayer-multilayer adsorption on an open and stable external surface of a powder.[74] Such a powder consists of aggregated non-porous particles giving this Type II of the adsorption isotherm, although the isotherm in Fig. 29 exhibits hysteresis (a sign of porosity, which causes a difference between adsorption and desorption processes). This hysteresis loop is that of Type H3 (IUPAC), which usually corresponds to aggregates of *plate-like* particles.

The specific surface area was calculated using BET3 method (full or 3-parameters BET equation) within the interval of the relative pressures 0–0.5 p/p_0 and gives an enormous value of 401 $m^2\ g^{-1}$ (one of the greatest values ever published for non-porous particles).

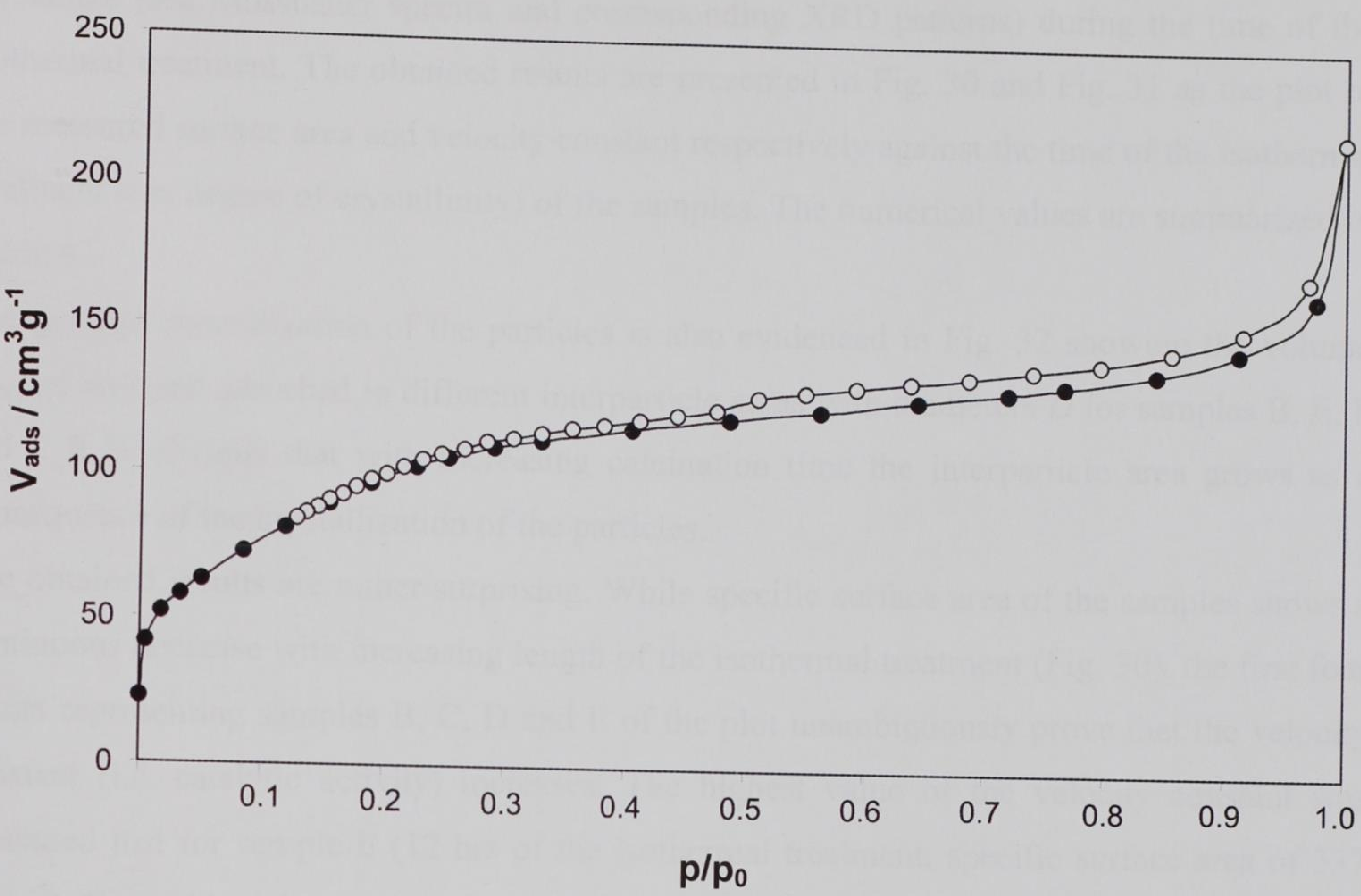

Fig. 29. Nitrogen isotherm for sample A. The filled circles represent the adsorption points and the open circles stand for the points measured during the desorption process.

5.5.4 CATALYTIC ACTIVITY OF THE LOW-LAYER SAMPLES

One would certainly expect that such a huge value of specific surface area (*ca.* 400 m^2 g^{-1} for sample B) determins such a material for a use in catalysis. That is why low-layer sample B was tested in catalytic decomposition of hydrogen peroxide H_2O_2. Surprisingly, the measured velocity constant turned to be extremely low when compared to those obtained for other materials with far lower values of specific surface area. Hence, the question was whether the catalytic properties were not bound to yet another property of a sample than only to the surface area. The first idea crossing our mind was that due to a high surface energy the surface of the particles might have been occupied by adsorbed gases decreasing consequently the catallytic activity. Sample B was therefore evacuated for 24 hrs and tested in the catalysis again. The obtained result however appeared to be almost the same as in the previous case – the achieved velocity constant turned to be extremely low.

The complete amorphous chatracter of sample B raised yet another question: wheather the missing quality (in spite of the enormous value of specific surface area) of the catalytic activity should not have been a degree of crystallinity of a sample? To investigate this idea we measured specific surface areas and velocity constants of samples C–J, which proved to crystallize (see Mössbauer spectra and corresponding XRD patterns) during the time of the isothermal treatment. The obtained results are presented in Fig. 30 and Fig. 31 as the plot of the measured surface area and velocity constant respectively against the time of the isothermal treatment (i.e. degree of crystallinity) of the samples. The numerical values are summarized in Table 4.

The gradual crystallization of the particles is also evidenced in Fig. 32 showing the volume V_{pore} of nitrogen adsorbed in different interparticle areas with diameters D for samples B, E, F and I. It is obvious that with increasing calcination time the interparticle area grows as a consequence of the crystallization of the particles.

The obtained results are rather surprising. While specific surface area of the samples shows a continuous decrease with increasing length of the isothermal treatment (Fig. 30), the first four points representing samples B, C, D and E of the plot unambiguously prove that the velocity constant (i.e. catalytic activity) increases. The highest value of the velocity constant was measured just for sample E (12 hrs of the isothermal treatment, specific surface area of 337 $m^2\ g^{-1}$). From this point onward the velocity constant gradually decreases (samples F, G, H, I and J) following a simultaneous decrease of the specific surface area (Fig. 31) as one would naturally expect. Hence it is obvious that an achievement of the ***best catalytic activity of a material is strongly conditioned by an advantageous combination of a degree of crystallinity with a sufficiently high value of the specific surface area.***

Table 4. The values of specific surface areas and velocity constants of samples B–J.

Sample	**Time of the thermal treatment** (hrs)	**Specific surface area** ($m^2\ g^{-1}$)	**Velocity constant**
B	6	401	0.00338
C	8	386	0.01605
D	10	340	0.02200
E	12	337	0.02641
F	17	288	0.01923
G	30	245	0.01388
H	48	235	0.00958
I	64	186	0.00520
J	100	154	0.00362

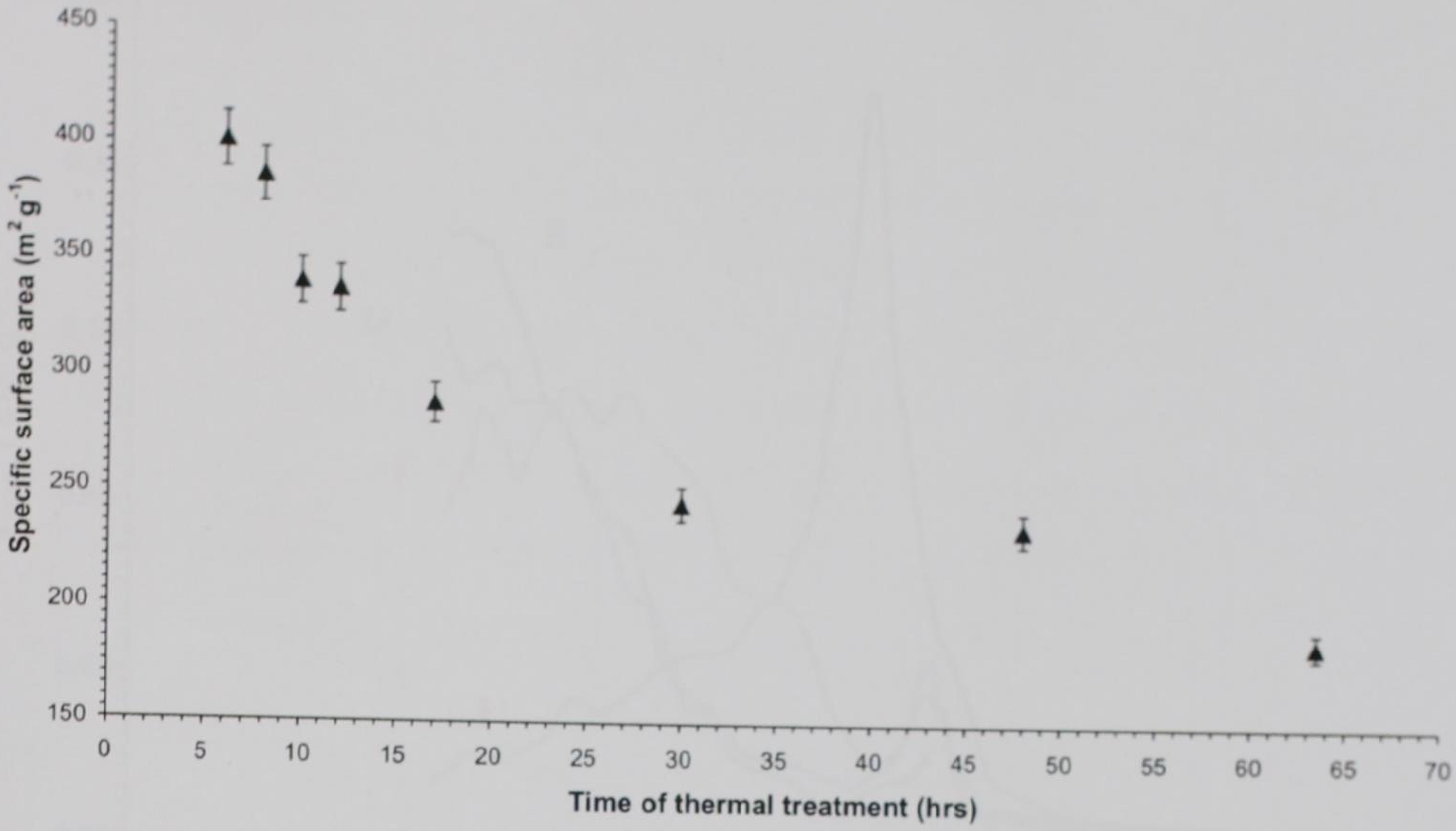

Fig. 30. Specific surface areas (± 3 %) of low-layer samples B–J prepared by an isothermal decomposition of $FeC_2O_4 \cdot 2H_2O$ at furnace temperature of 175 °C.

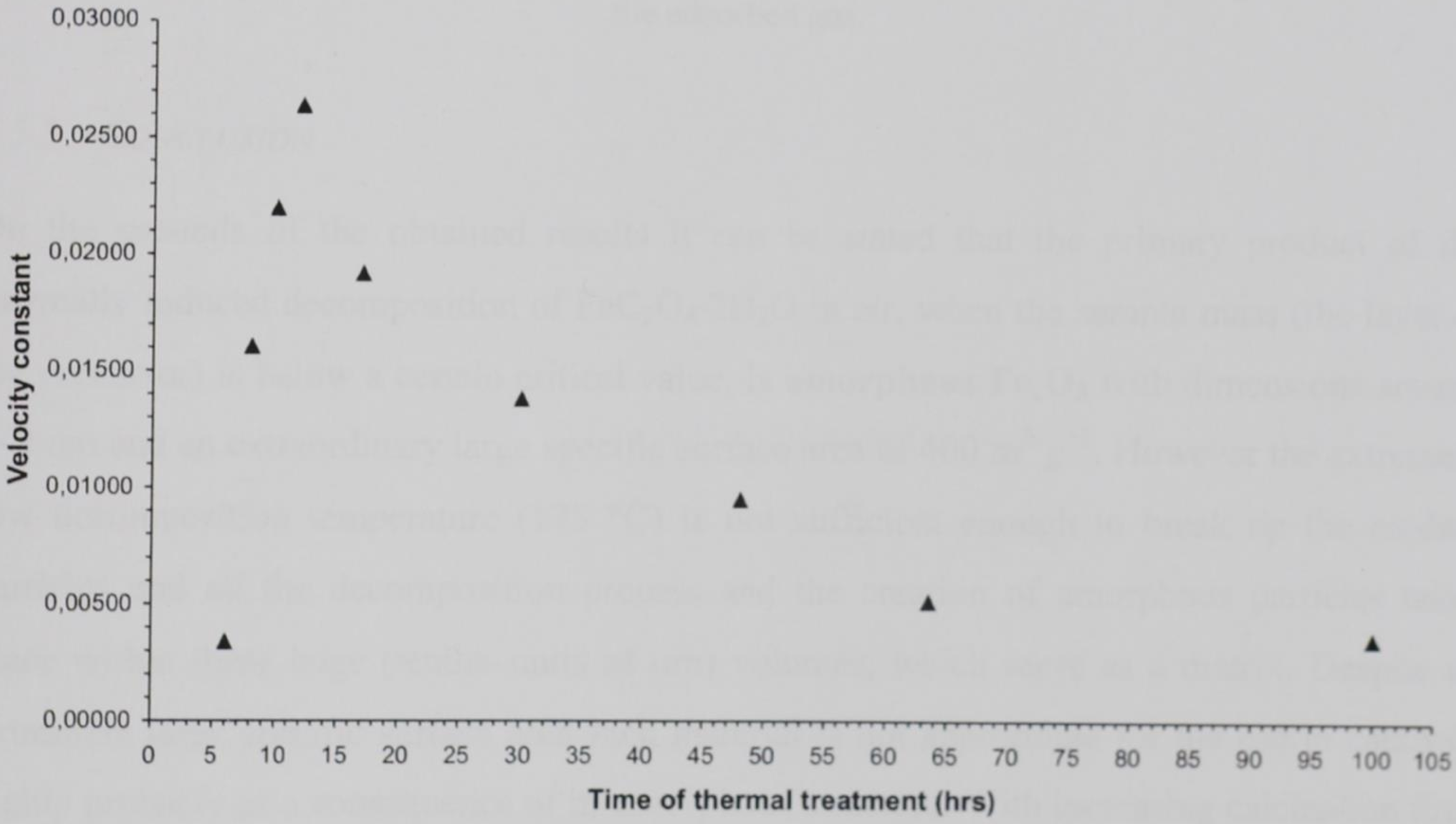

Fig. 31. Velocity constants of low-layer samples B–J prepared by an isothermal decomposition of $FeC_2O_4 \cdot 2H_2O$ at furnace temperature of 175 °C.

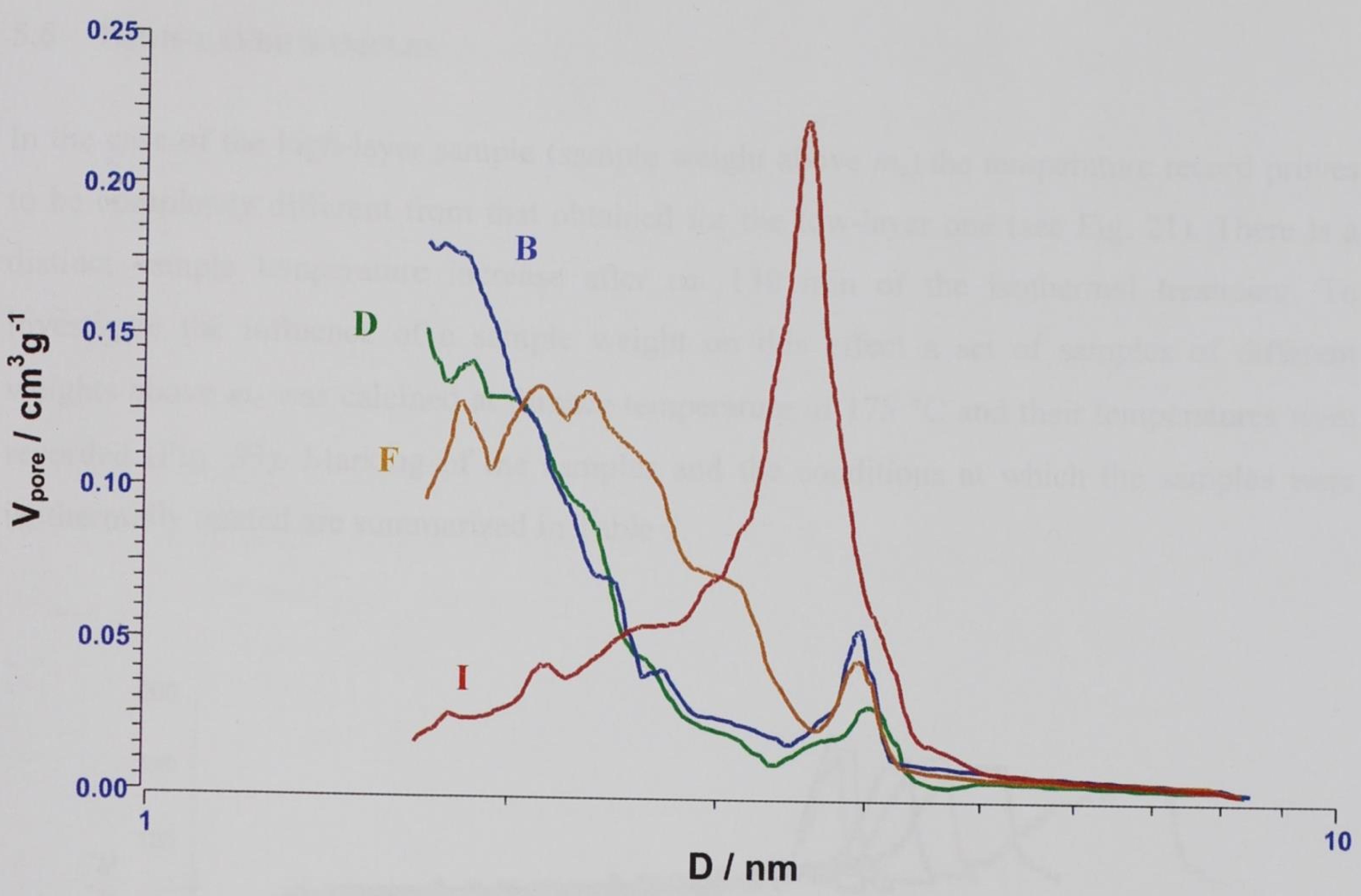

Fig. 32. The interparticle area distribution in samples B, D, F and I expressed through the amount of the adsorbed gas.

5.5.5 CONCLUSION

On the grounds of the obtained results it can be stated that the primary product of the thermally induced decomposition of $FeC_2O_4 \cdot 2H_2O$ in air, when the sample mass (the layer of the precursor) is below a certain critical value, is **amorphous Fe_2O_3** with dimensions around 1–2 nm and an extraordinary large specific surface area of 400 m^2 g^{-1}. However the extremely low decomposition temperature (175 °C) is not sufficient enough to break up the oxalate particles and all the decomposition process and the creation of amorphous particles takes place within these huge (tenths–units of μm) volumes, which serve as a matrix. Despite an extremely large specific surface area such material is not appropriate for the use in catalysis highly probably as a consequence of its amorphous structure. With increasing calcination time amorphous Fe_2O_3 gradually crystallizes and nanocrystalline α-Fe_2O_3 with dimensions around 10 nm is formed. As a consequence of the crystallization process specific surface area naturally decreases. Nevertheless it was demonstrated that an advantageous combination of a degree of crystallinity of a sample with sufficient surface area leads to unprecedented catalytic properties. From the viewpoint of the phase composition any presence of γ-Fe_2O_3 can be excluded.

5.6 HIGH-LAYER SAMPLES

In the case of the high-layer sample (sample weight above m_c) the temperature record proves to be completely different from that obtained for the low-layer one (see Fig. 21). There is a distinct sample temperature increase after *ca.* 130 min of the isothermal treatment. To investigate the influence of a sample weight on this effect a set of samples of different weights above m_c was calcined at furnace temperature of 175 °C and their temperatures were recorded (Fig. 33). Marking of the samples and the conditions at which the samples were isothermally treated are summarized in Table 5.

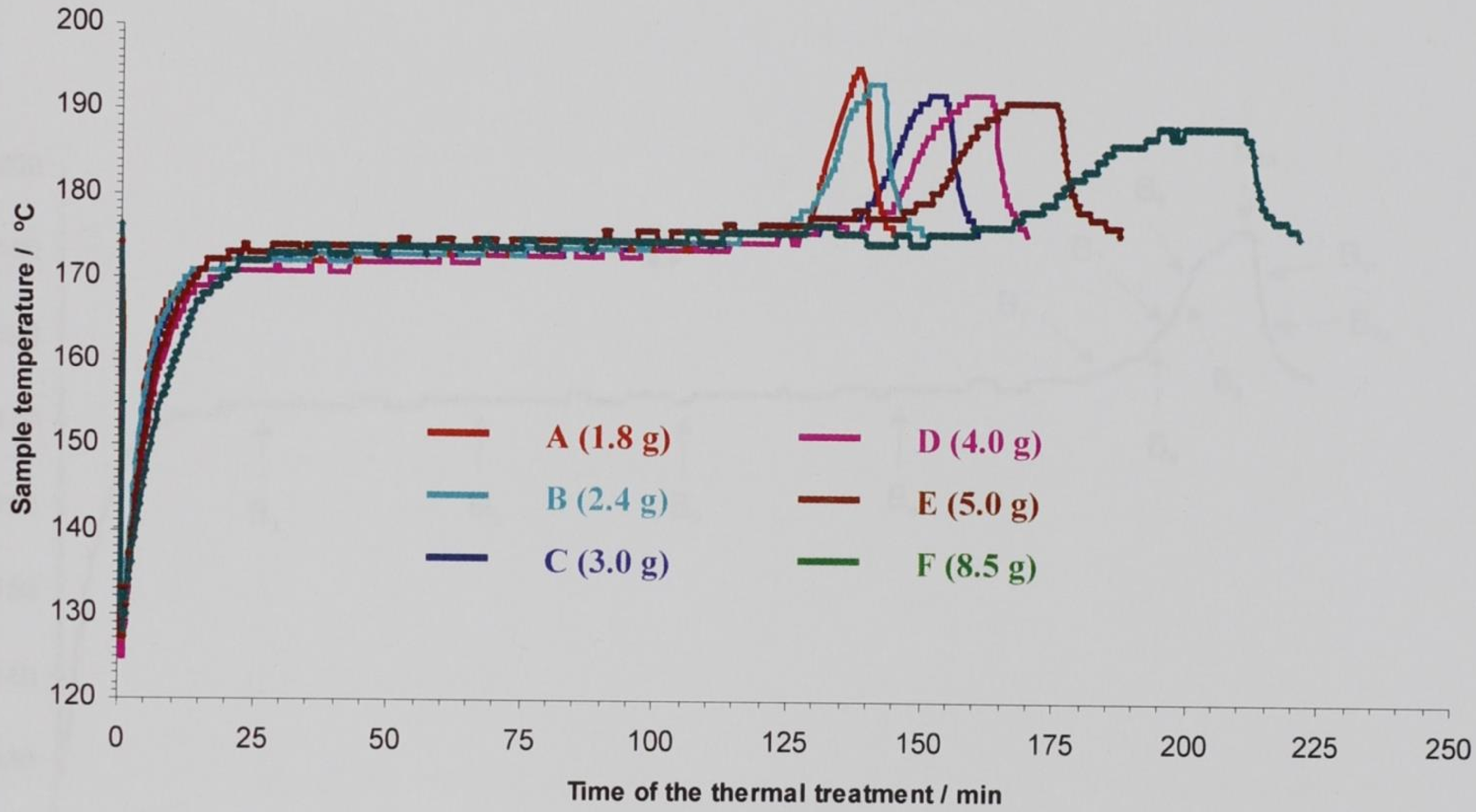

Fig. 33. Temperature records of the samples A, B, C, D, E and F taken during the isothermal treatment of $FeC_2O_4 \cdot 2H_2O$ at 175 °C.

Table 5 The conditions at which the high-layer samples A–F were prepared.

$FeC_2O_4 \cdot 2H_2O$, furnace temperature 175 °C, thermal treatment behind the temperature effect						
Sample	**A**	**B**	**C**	**D**	**E**	**F**
Weight/ mg	1800	2400	3000	4000	5000	8500

One can readily visualise from Fig. 33 that there is an unequivocal relationship between the sample mass and the arising temperature effect – with increasing sample weight the temperature effect starts later in time, becomes broader, its maximum shifts towards longer calcination times and reaches lower maximum temperature values.

To investigate the origin of the above discussed temperature effect itself a phase composition of a chosen sample (B) was investigated in different experimental points B_1–B_{12} as illustratively demonstrated in Fig. 34 and summarized in Table 6. It should be mentioned however that the time axis in Fig. 34 is only illustrative, as the temperature effect did not start exactly at the same time when preparing samples B_5–B_{12}. The conditions at which samples B_5–B_{12} were prepared are therefore presented in the sample temperatures (Table 6), which unlike the calcination times appeared to be very reproducible and led to the very same phase composition of the samples.

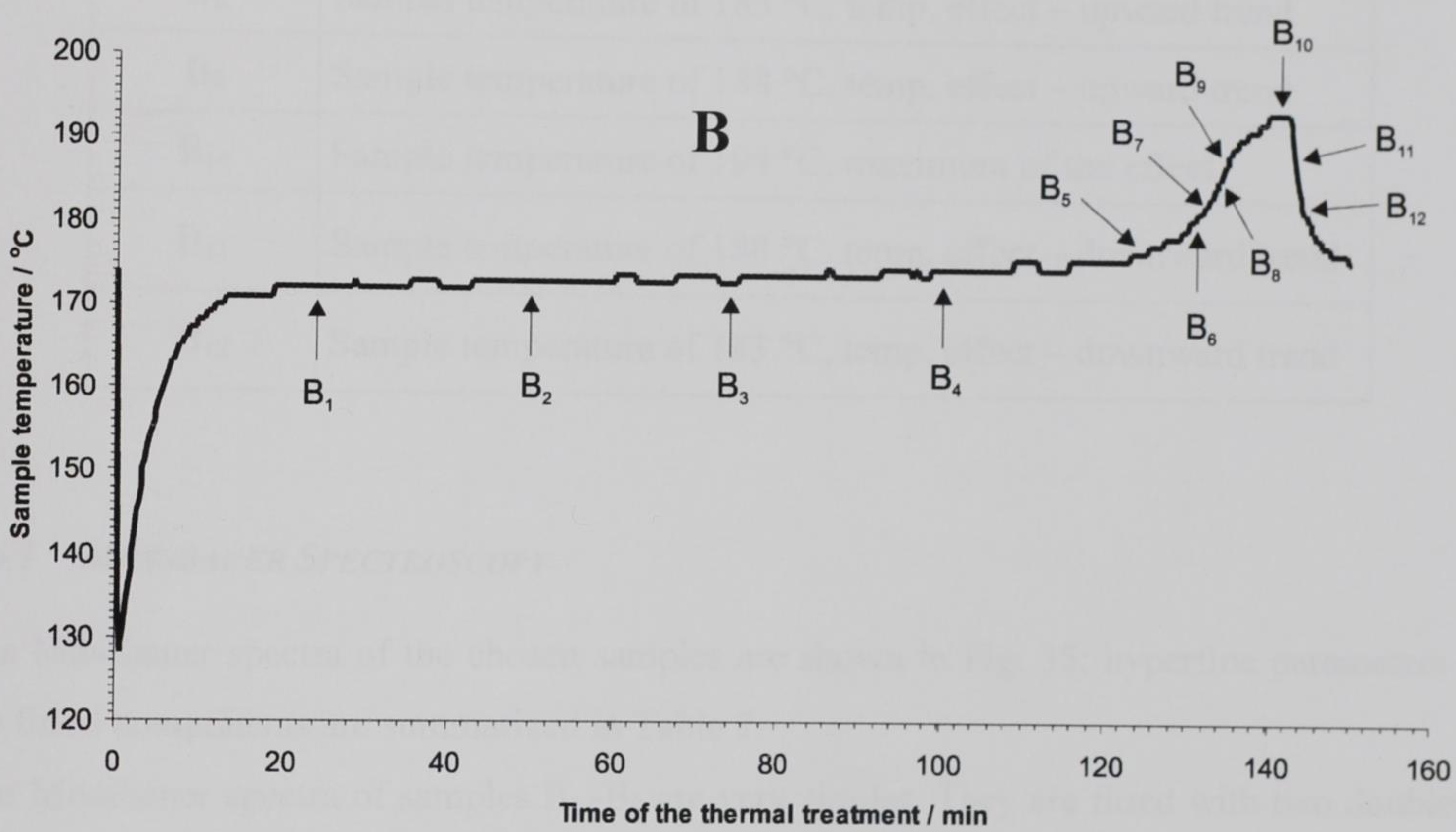

Fig. 34. Temperature record of sample B taken during the isothermal treatment at 175 °C. B_1–B_{12} label the points of the curve at which the isothermal treatment was stopped and the phase composition of as-prepared samples was checked by Mössbauer spectroscopy and XRD.

Table 6 The conditions at which samples B_1–B_{12} were prepared. Furnace temperature: 175 °C.

Sample	Conditions of preparation
B_1	25 min of the isothermal treatment
B_2	50 min of the isothermal treatment
B_3	75 min of the isothermal treatment
B_4	100 min of the isothermal treatment
B_5	Sample temperature of 177 °C, temp. effect – upward trend
B_6	Sample temperature of 179 °C, temp. effect – upward trend
B_7	Sample temperature of 181 °C, temp. effect – upward trend
B_8	Sample temperature of 183 °C, temp. effect – upward trend
B_9	Sample temperature of 188 °C, temp. effect – upward trend
B_{10}	Sample temperature of 194 °C, maximum of the effect
B_{11}	Sample temperature of 188 °C, temp. effect – downward trend
B_{12}	Sample temperature of 183 °C, temp. effect – downward trend

5.6.1 MÖSSBAUER SPECTROSCOPY

The Mössbauer spectra of the chosen samples are shown in Fig. 35; hyperfine parameters of the fitted components are summarized in Table 7.

The Mössbauer spectra of samples B_1–B_3 are very similar. They are fitted with two doublets, where the hyperfine parameters of $\delta = 1.18$ mm s^{-1} and $\Delta E_Q = 1.17$ mm s^{-1} of the dominant one are typical for divalent iron and represent clearly undecomposed $FeC_2O_4{\cdot}2H_2O$ structure. The isomer shift value ($\delta =$ *ca.* 0.30 mm s^{-1}) of the second weak doublet indicates high spin Fe^{3+} cations in a highly distorted ($\Delta E_Q =$ *ca.* 0.80 mm s^{-1}) iron oxide structure, which obviously arises as a primary decomposition product.

Besides both the Fe^{2+} and rather broadly quadrupoly split trivalent iron components there is another Fe^{3+} doublet visible in the Mössbauer spectrum of sample B_4, which exhibits still far lower value of quadrupole splitting ($\Delta E_Q =$ *ca.* 0.60 mm s^{-1}) indicating more ordered surroundings of Fe atoms. All the samples B_1–B_4 exhibit only a very low degree of decomposition of the oxalate structure; after 100 min of the isothermal treatment (sample B_4) there are still remaining 68.8 % of $FeC_2O_4{\cdot}2H_2O$ from the viewpoint of the relative spectrum areas.

The Mössbauer spectrum of sample B_5 (the very beginning of the arising temperature effect: an increase of sample temperature from 175 to 177 °C) indicates the first significant decrease of the content of ferrous oxalate dihydrate in favour of both Fe^{3+} components (54.6 % of $FeC_2O_4{\cdot}2H_2O$ *vs.* 45.4 % of both Fe^{3+} doublets).

Despite a sample temperature increase of only 2 °C (from 177 to 179 °C), the Mössbauer spectrum of sample B_6 shows a dramatic change of its shape in comparison to the previous one (B_5). Besides the two Fe^{3+} components ascribed to superparamagnetic Fe_2O_3 and the Fe^{2+} one belonging to the undecomposed oxalate structure, there are apparent two new magnetically split patterns, the hyperfine parameters of which $\delta = 0.33$ mm s^{-1}, $\varepsilon_Q = 0.08$ mm s^{-1}, $H = 48.3$ T and $\delta = 0.24$ mm s^{-1}, $\varepsilon_Q = 0.06$ mm s^{-1}, $H = 43.5$ T could be assigned to the bulk and surface of the nanocrystalline maghemite particles respectively. Especially the quadrupole shift values close to zero enable to clearly identify the cubic maghemite structure. As typical for surface parts of particles, isomer shift and hyperfine magnetic field of the latter sextet are significantly reduced to the lower values in comparison to those representing bulk particle parts.[4]

The Mössbauer spectrum of sample B_7 (sample temperature 181 °C) shows a shape similar to that of sample B_6, yet the phase composition differs. Again, there are present two magnetically split components but the hyperfine parameters $\delta = 0.37$ mm s^{-1} and $\varepsilon_Q = -0.21$ mm s^{-1} of the more magnetically split ($H = 48.7$ T) one indicate now clearly the hematite structure. Hyperfine parameters of the second sextet component ($\delta = 0.33$ mm s^{-1}, $\varepsilon_Q = 0.02$ mm s^{-1}, $H = 44.4$ T) evidence still the presence of very small crystalline maghemite particles. It should be also noted that the extremely broad linewidth ($\Gamma = 1.92$ mm s^{-1}) of the latter sextet could also hide a certain minor contribution of ultrafine crystalline hematite particles, though its relative proportion cannot be computed at these conditions. It should be also emphasised that all the samples B_6–B_{12} (including final sample B of course) exhibit strong magnetic behaviour and are therefore predominantly made of ferrimagnetic maghemite. As clearly seen from Table 7, the highest content of crystalline maghemite exhibits just sample B_6 (39.3 %), in all following samples (B_7–B_{12}) nevertheless the content of ferrimagnetic γ-Fe_2O_3 does not fall below 30 %.

Samples B_8–B_{12} show nearly the same phase composition as sample B_7. They exhibit only a gradual decrease of the content of the ferrous oxalate dihydrate in favour of the Fe^{3+} components; relative contributions of maghemite and hematite remain nearly constant (*ca.* 30 *vs. ca.* 10 %). In samples B_{10}–B_{12} (the maximum and the points on the descending edge of the temperature effect respectively) is in addition a small proportion of anhydrous ferrous oxalate visible together with the remnants of the decreasing iron oxalate dihydrate content.

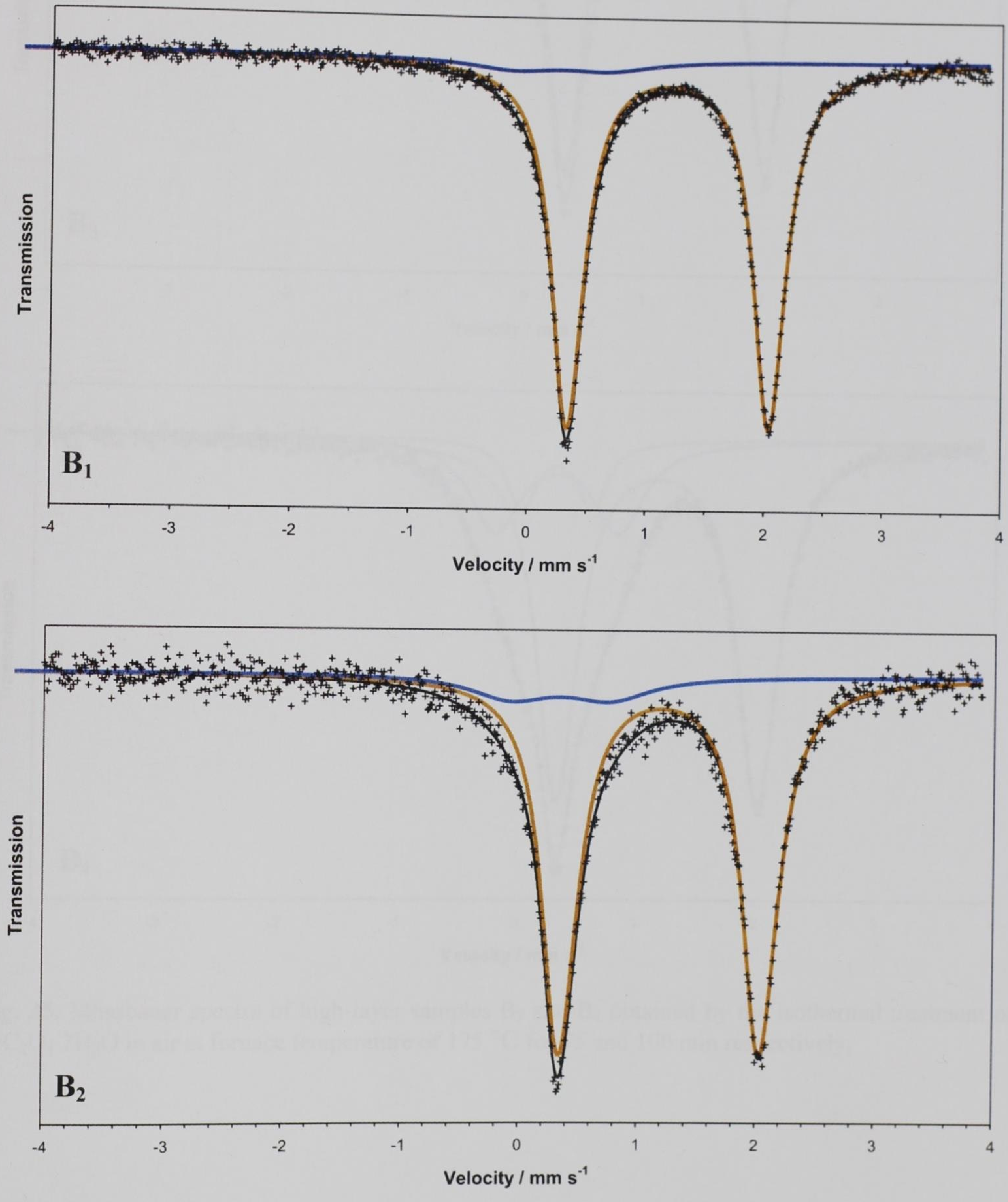

Fig. 35. Mössbauer spectra of high-layer samples B_1 and B_2 obtained by the isothermal treatment of $FeC_2O_4 \cdot 2H_2O$ in air at furnace temperature of 175 °C for 25 and 50 min respectively.

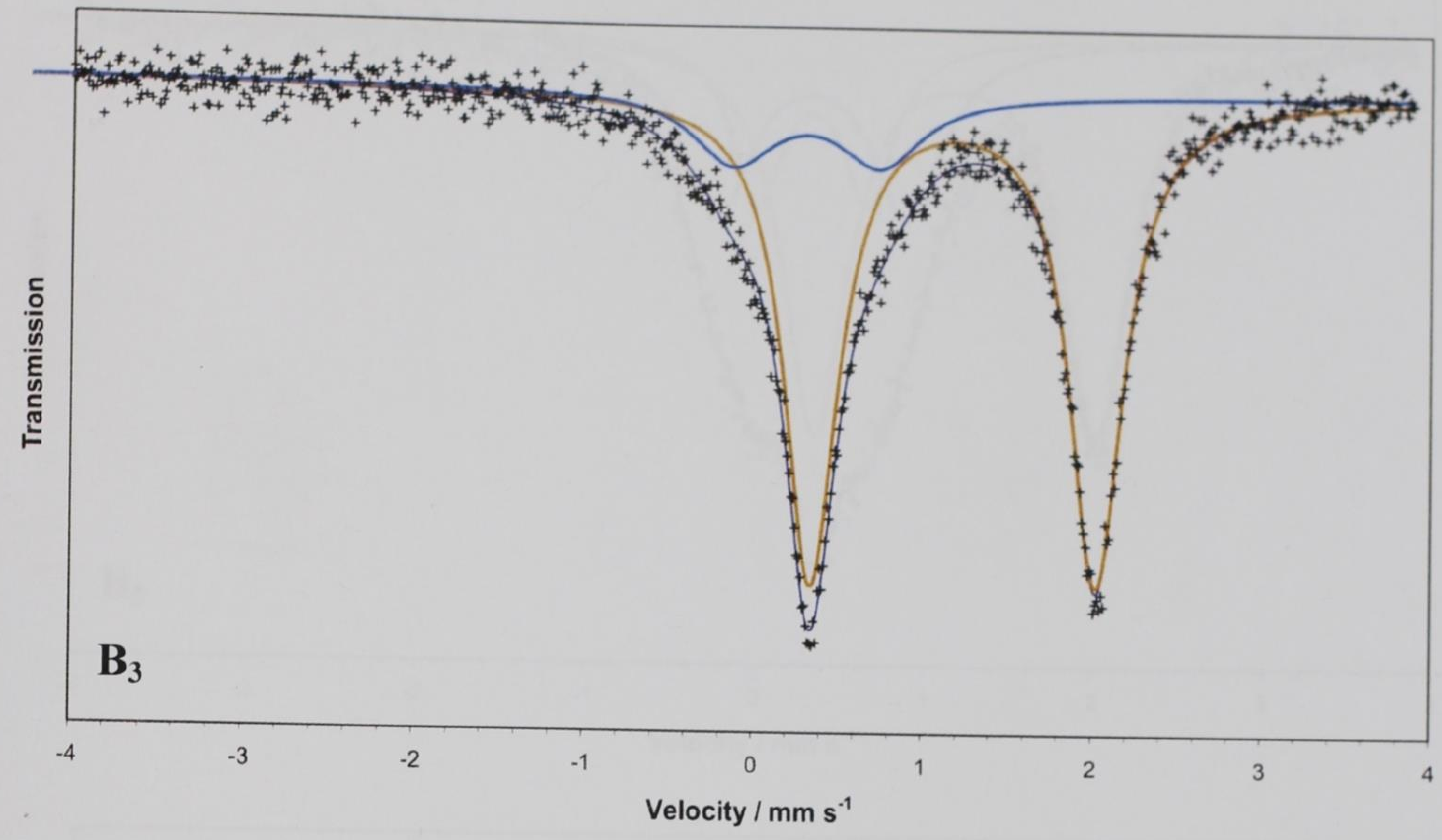

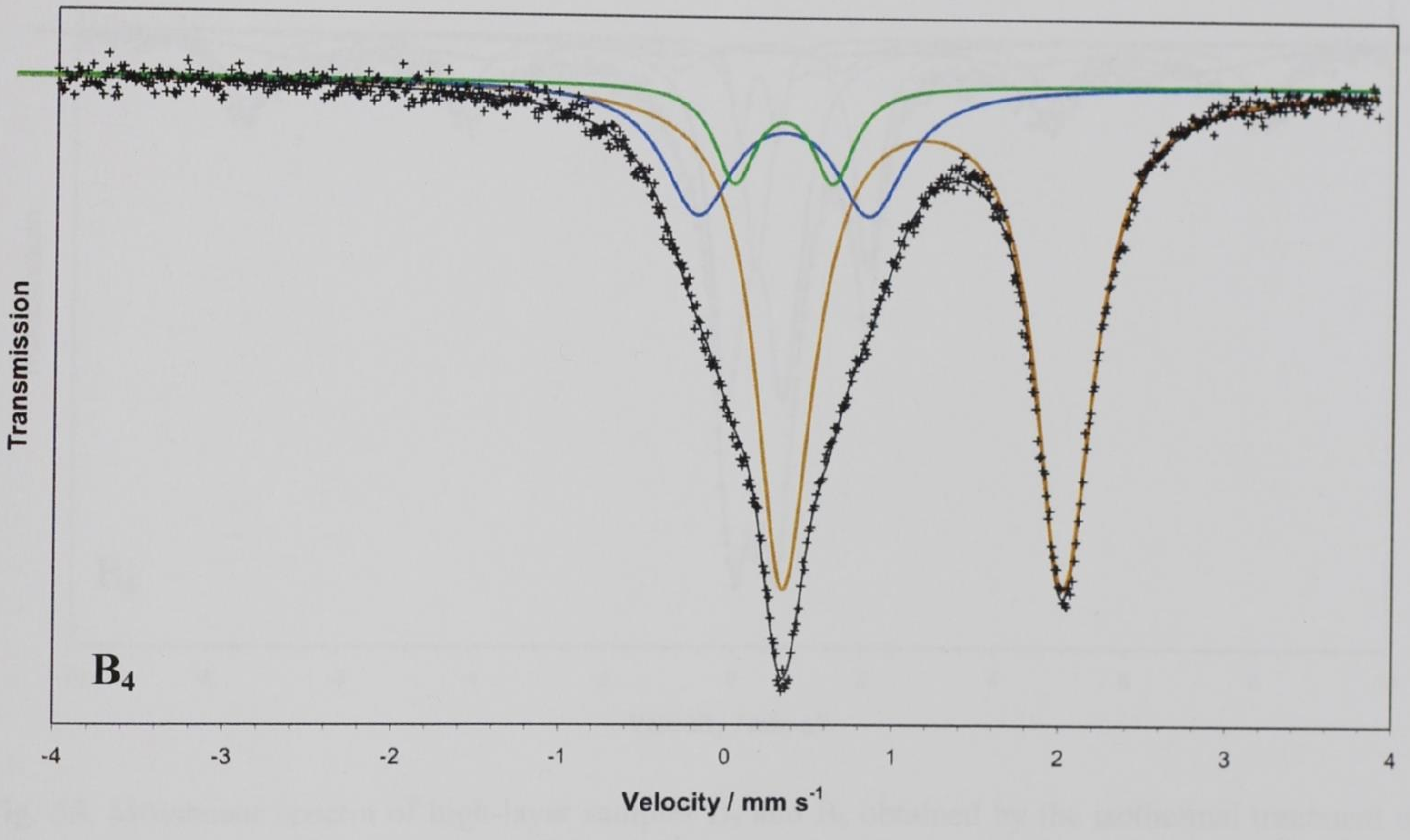

Fig. 35. Mössbauer spectra of high-layer samples B$_3$ and B$_4$ obtained by the isothermal treatment of $FeC_2O_4 \cdot 2H_2O$ in air at furnace temperature of 175 °C for 75 and 100 min respectively.

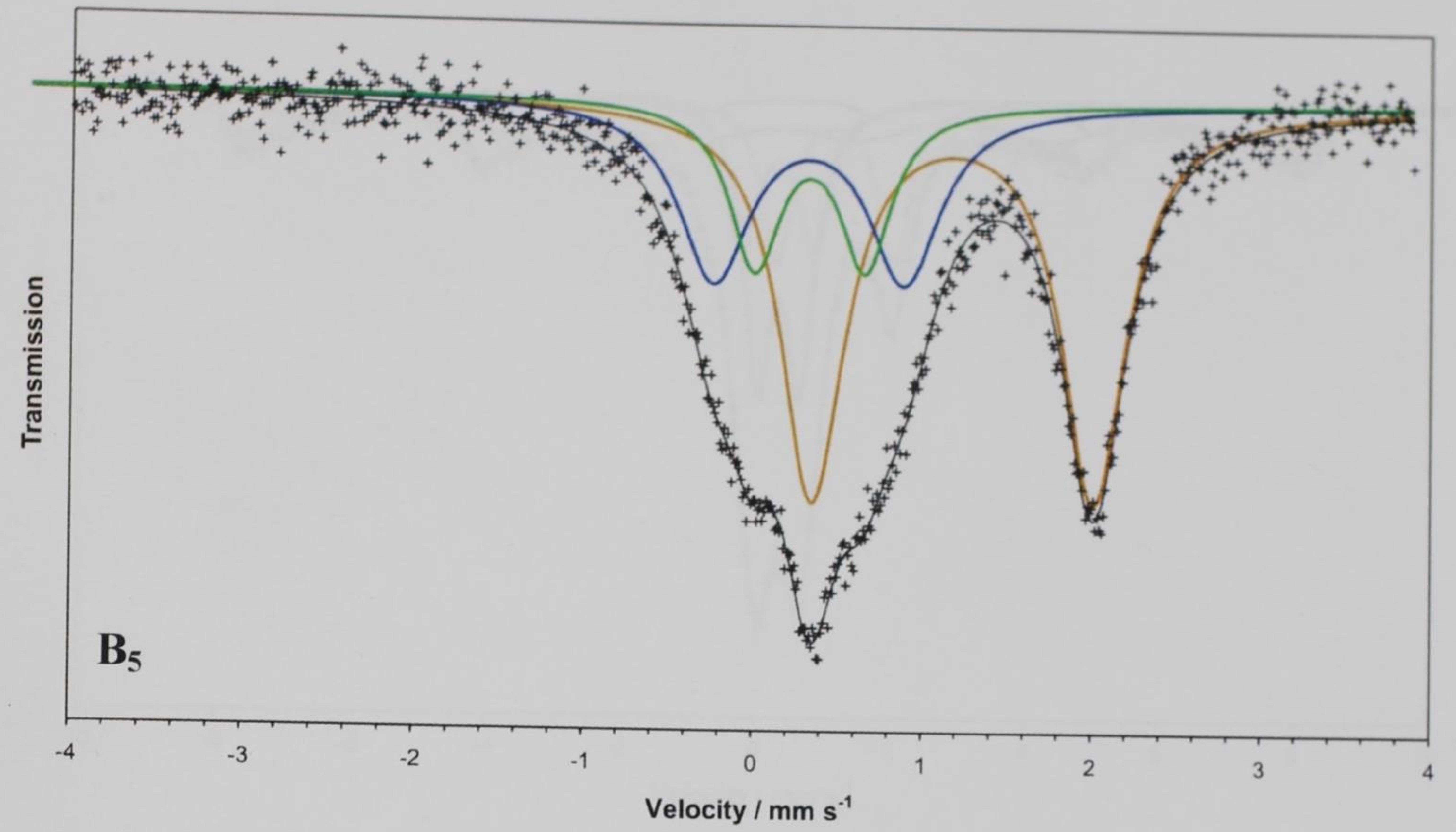

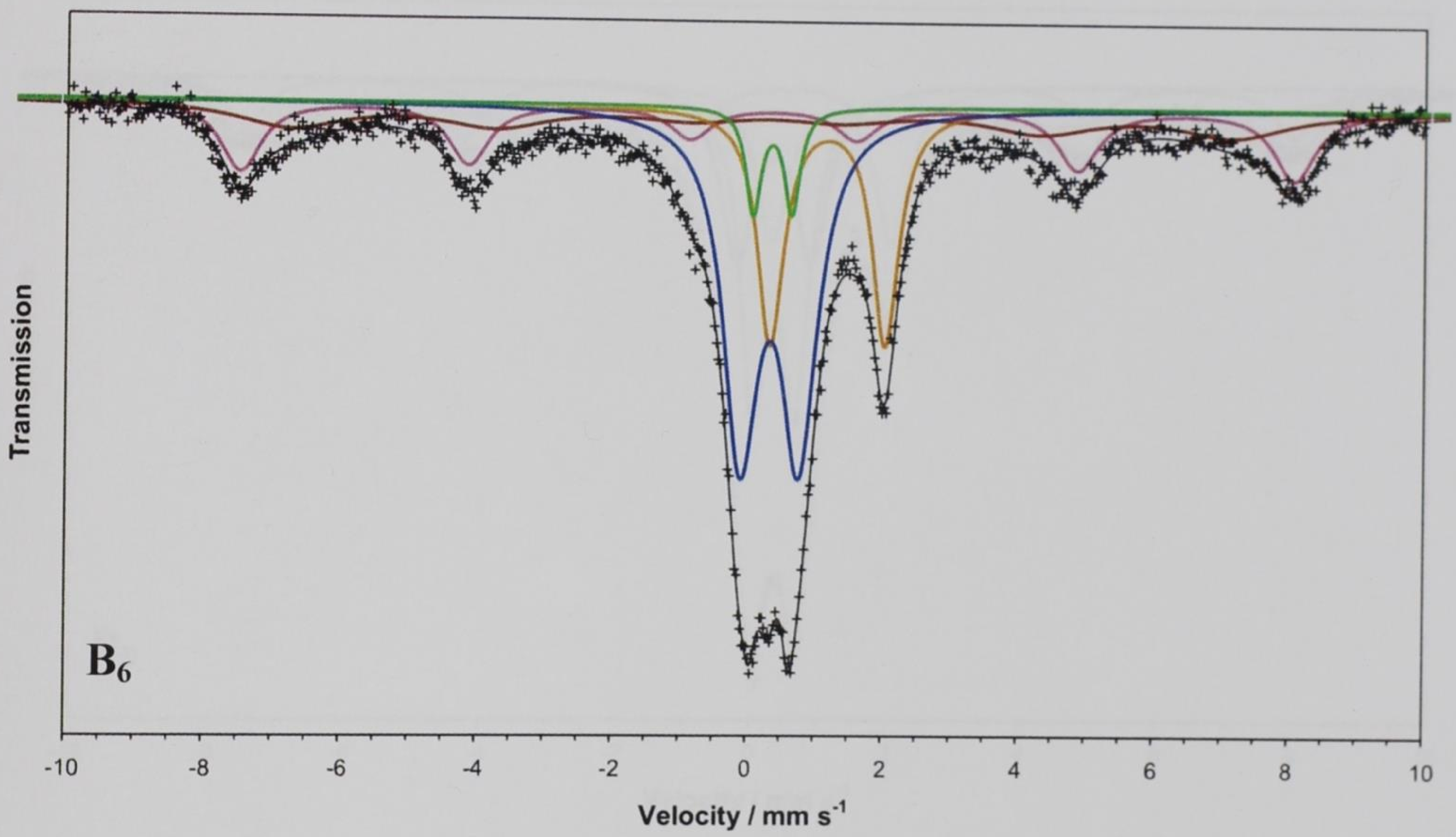

Fig. 35. Mössbauer spectra of high-layer samples B_5 and B_6 obtained by the isothermal treatment of $FeC_2O_4 \cdot 2H_2O$ in air at furnace temperature of 175 °C up to the sample temperature of 177 and 179 °C respectively (upward trend).

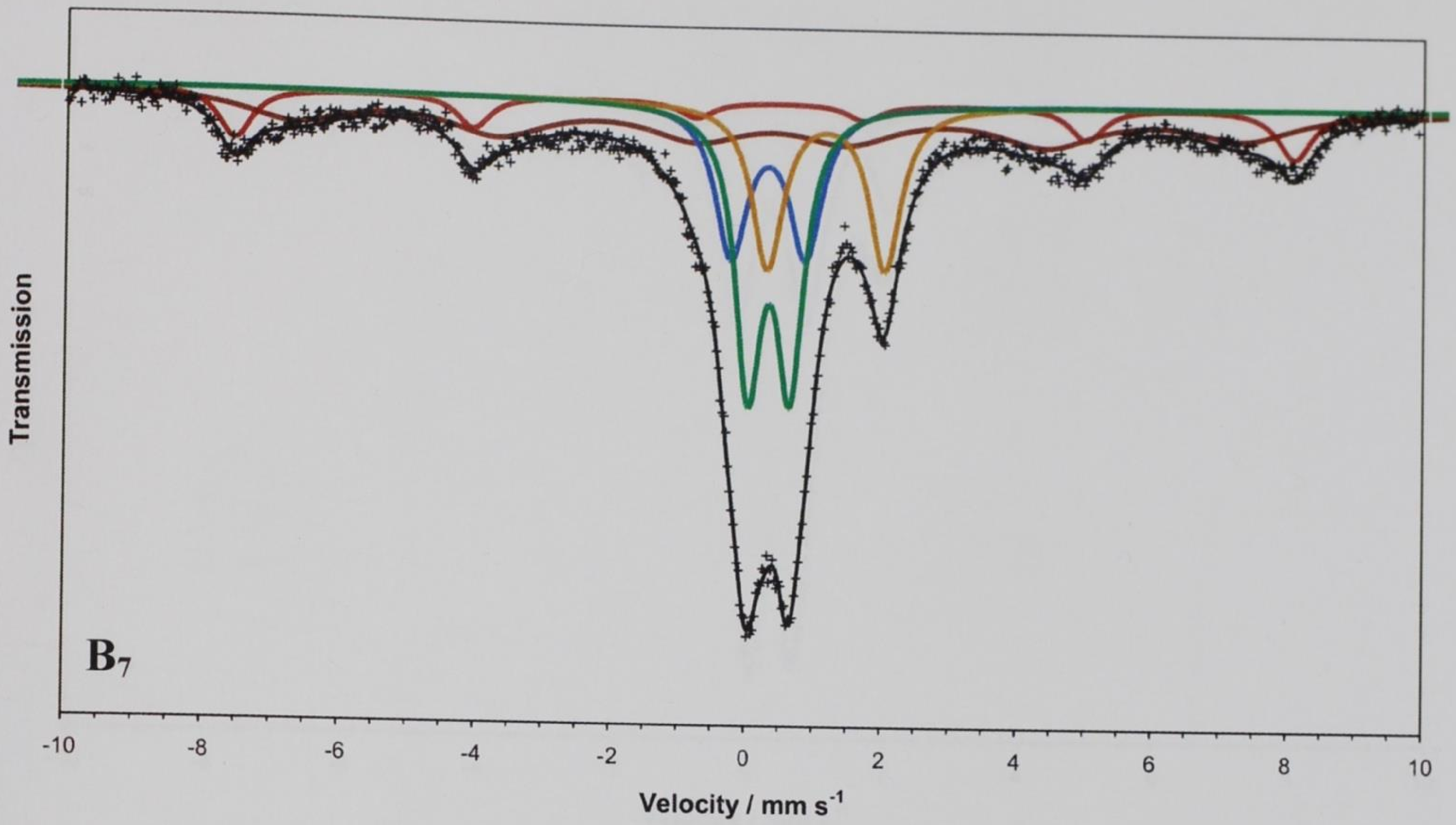

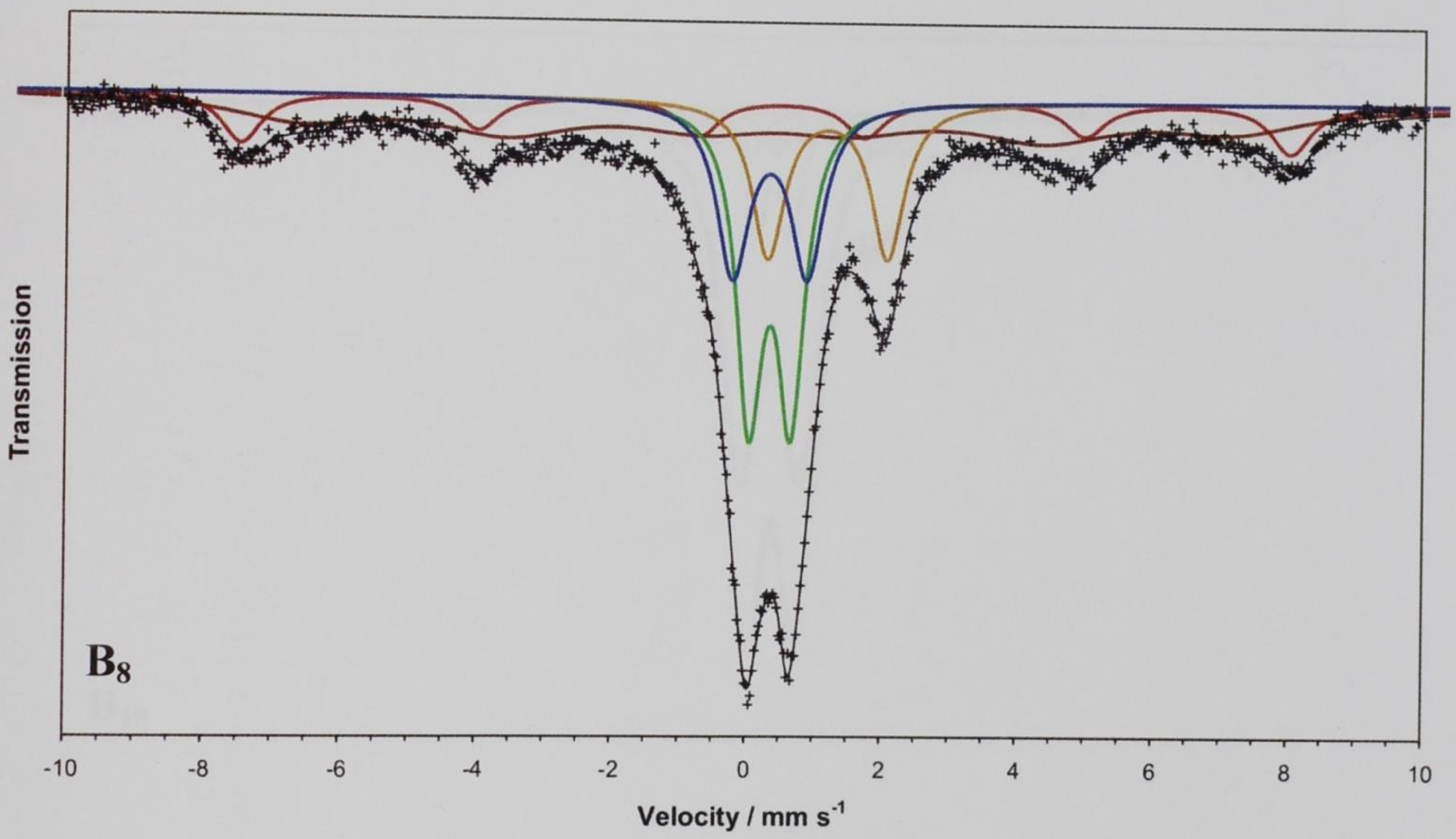

Fig. 35. Mössbauer spectra of high-layer samples B_7 and B_8 obtained by the isothermal treatment of $FeC_2O_4 \cdot 2H_2O$ in air at furnace temperature of 175 °C up to the sample temperature of 181 and 183 °C respectively (upward trend).

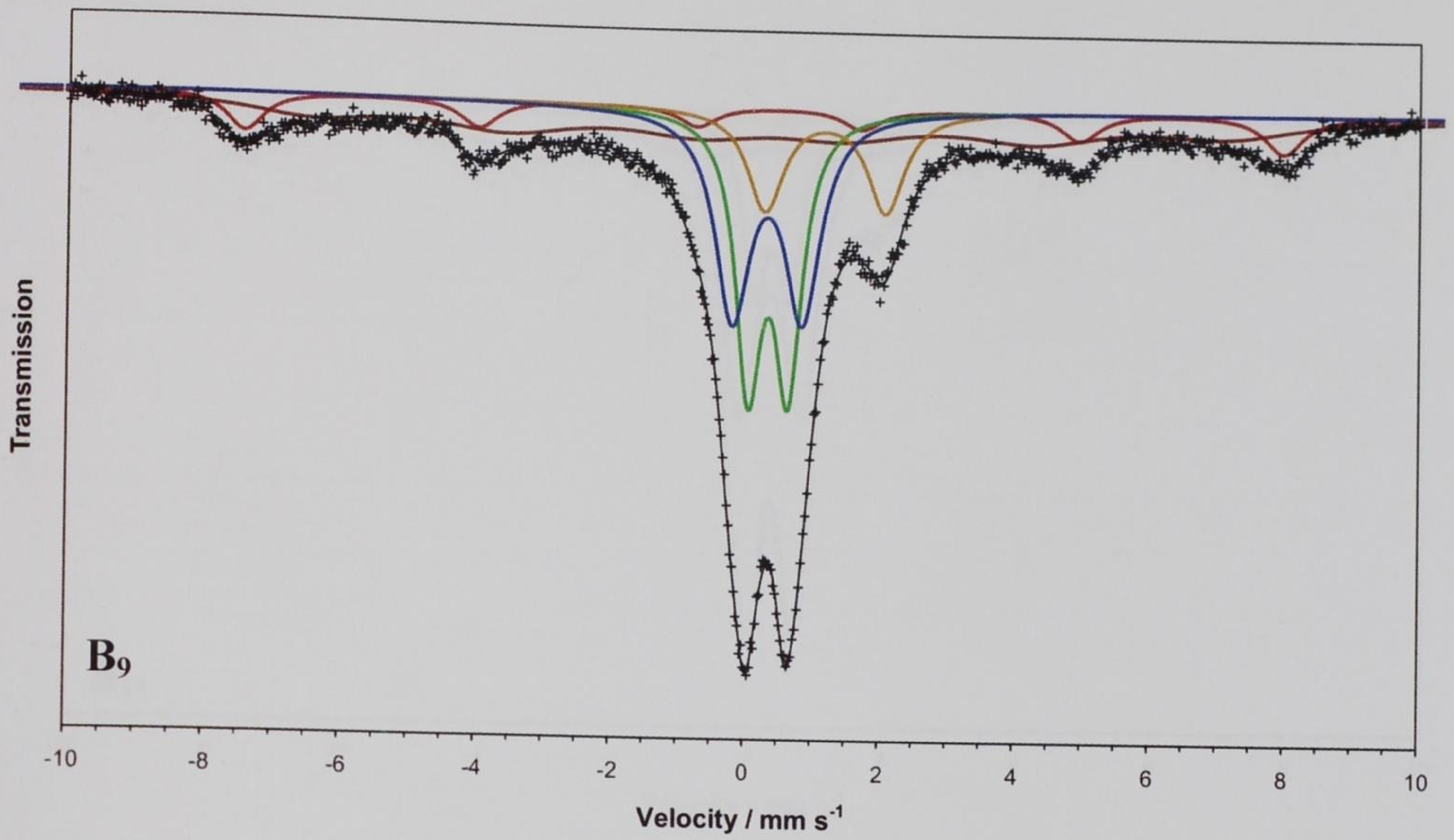

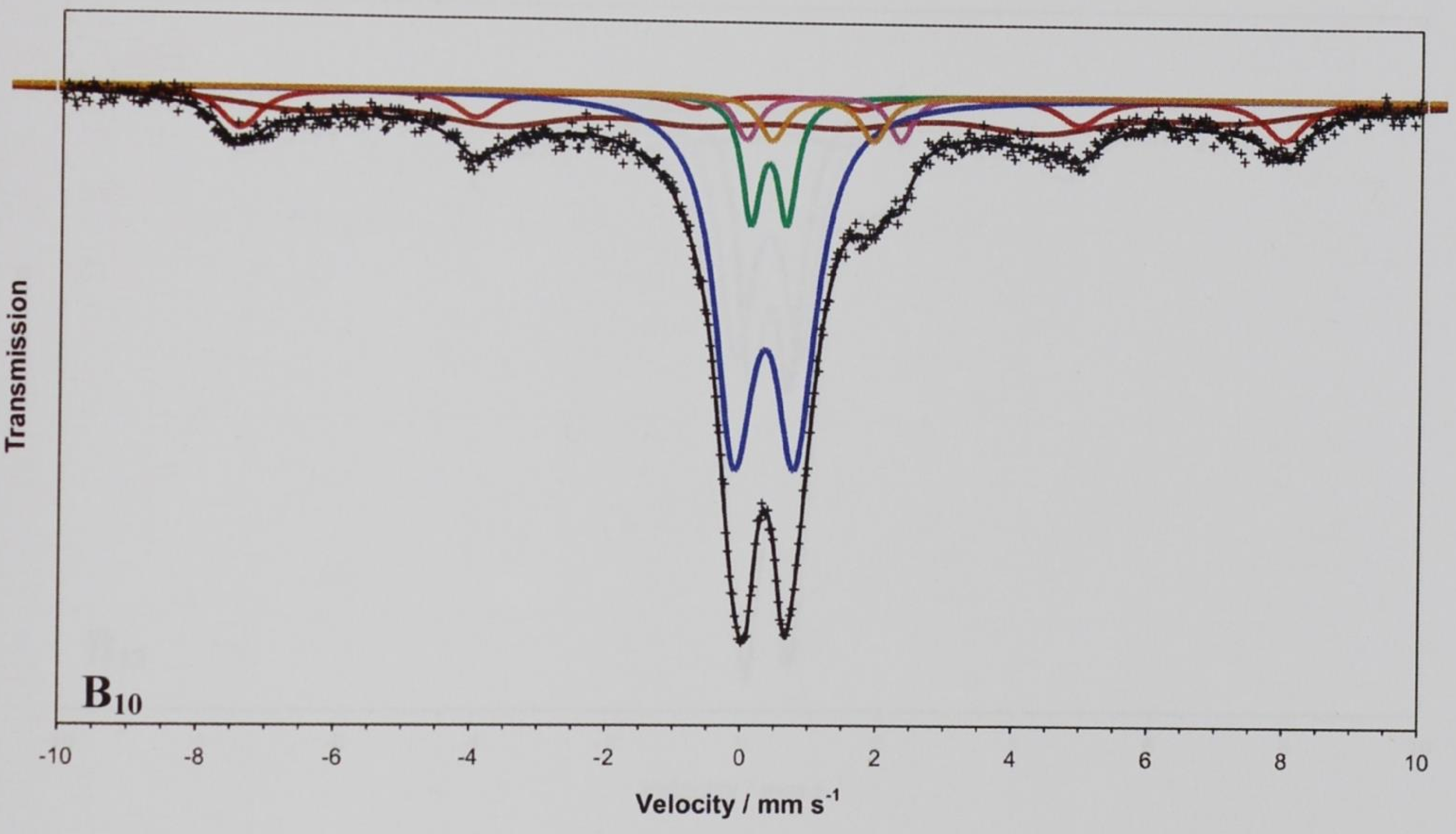

Fig. 35. Mössbauer spectra of high-layer samples B_9 and B_{10} obtained by the isothermal treatment of $FeC_2O_4 \cdot 2H_2O$ in air at furnace temperature of 175 °C up to the sample temperature of 188 and 194 °C respectively (upward trend).

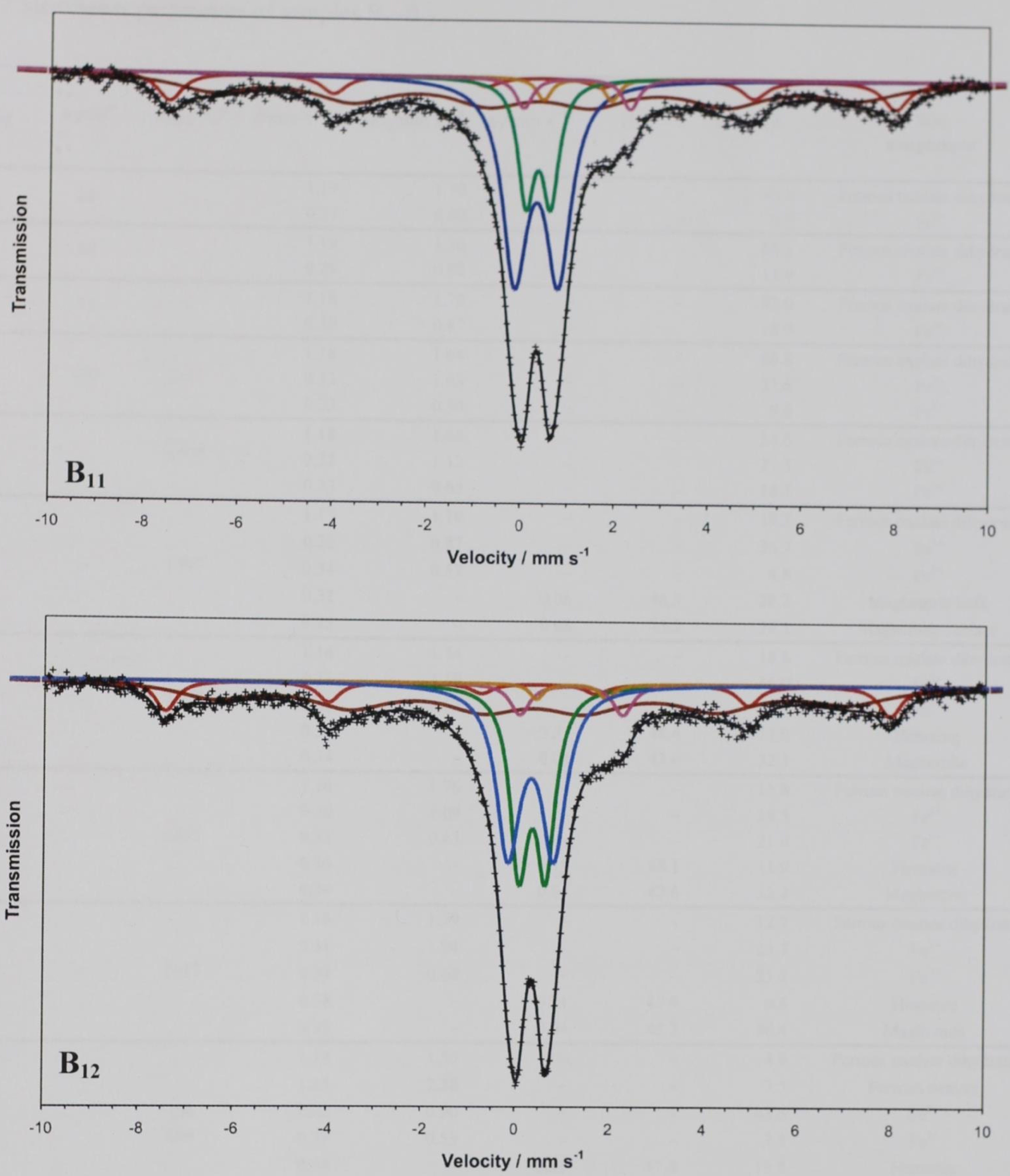

Fig. 35. Mössbauer spectra of high-layer samples B$_{11}$ and B$_{12}$ obtained by the isothermal treatment of $FeC_2O_4 \cdot 2H_2O$ in air at furnace temperature of 175 °C up to the sample temperature of 188 and 183 °C respectively (downward trend).

Table 7 Mössbauer parameters of samples B_1–B_{12}.

Sample	t/min[a]	T_{samp}/°C[b]	δ/mm s^{-1}[c]	ΔE_Q/mm s^{-1}[d]	ε_Q/mm s^{-1}[e]	H/T[f]	RA (%)[g]	Site assignment
B_1	25	–	1.19	1.70	–	–	93.1	Ferrous oxalate dihydrate
			0.27	0.80	–	–	6.9	Fe^{3+}
B_2	50	–	1.19	1.70	–	–	88.1	Ferrous oxalate dihydrate
			0.29	0.82	–	–	11.9	Fe^{3+}
B_3	75	–	1.18	1.70	–	–	82.0	Ferrous oxalate dihydrate
			0.30	0.87	–	–	18.0	Fe^{3+}
B_4	100	–	1.18	1.68	–	–	68.8	Ferrous oxalate dihydrate
			0.33	1.03	–	–	21.6	Fe^{3+}
			0.33	0.59	–	–	9.6	Fe^{3+}
B_5	–	177↑	1.18	1.66	–	–	54.6	Ferrous oxalate dihydrate
			0.32	1.12	–	–	27.3	Fe^{3+}
			0.33	0.65	–	–	18.1	Fe^{3+}
B_6	–	179↑	1.17	1.70	–	–	19.2	Ferrous oxalate dihydrate
			0.32	0.87	–	–	36.7	Fe^{3+}
			0.34	0.57	–	–	4.8	Fe^{3+}
			0.32	–	0.06	48.3	20.2	Maghemite bulk
			0.25	–	0.08	43.2	19.1	Maghemite surface
B_7	–	181↑	1.16	1.74	–	–	16.8	Ferrous oxalate dihydrate
			0.31	1.10	–	–	16.0	Fe^{3+}
			0.33	0.62	–	–	23.9	Fe^{3+}
			0.37	–	−0.21	48.6	11.0	Hematite
			0.34	–	0.04	43.6	32.3	Maghemite
B_8	–	183↑	1.16	1.76	–	–	15.8	Ferrous oxalate dihydrate
			0.30	1.09	–	–	18.5	Fe^{3+}
			0.33	0.63	–	–	21.6	Fe^{3+}
			0.36	–	−0.19	48.1	11.9	Hematite
			0.34	–	0.04	42.6	32.2	Maghemite
B_9	–	185↑	1.16	1.79	–	–	12.7	Ferrous oxalate dihydrate
			0.31	1.04	–	–	23.7	Fe^{3+}
			0.34	0.60	–	–	23.5	Fe^{3+}
			0.38	–	−0.21	47.9	9.6	Hematite
			0.33	–	0.04	42.3	30.4	Maghemite
B_{10}	–	194 max	1.14	1.50	–	–	4.0	Ferrous oxalate dihydrate
			1.15	2.28	–	–	3.5	Ferrous oxalate
			0.32	0.90	–	–	43.5	Fe^{3+}
			0.35	0.53	–	–	7.5	Fe^{3+}
			0.36	–	−0.21	47.8	10.8	Hematite
			0.35	–	0	43.0	30.7	Maghemite
B_{11}	–	188↓	1.19	1.45	–	–	2.4	Ferrous oxalate dihydrate
			1.17	2.27	–	–	3.8	Ferrous oxalate
			0.33	0.93	–	–	34.7	Fe^{3+}
			0.35	0.52	–	–	14.0	Fe^{3+}
			0.36	–	−0.22	48.1	10.1	Hematite
			0.33	–	0.07	42.9	35.0	Maghemite
B_{12}	–	183↓	1.16	1.49	–	–	1.5	Ferrous oxalate dihydrate
			1.16	2.20	–	–	4.3	Ferrous oxalate
			0.32	0.97	–	–	27.9	Fe^{3+}
			0.35	0.57	–	–	22.9	Fe^{3+}
			0.36	–	−0.21	47.9	9.4	Hematite
			0.34	–	0.02	41.9	33.9	Maghemite

[a] t = time of the isothermal treatment at furnace temperature (175 °C), [b] T_{samp} = sample temperature when different from furnace temperature (the arrows ndicate either increasing or decreasing trend of sample temperature), [c] δ = isomer shift (with respect to metallic iron, ±0.01), [d] ΔE_Q = quadrupole splitting ±0.01), [e] ε_Q = quadrupole shift (±0.01), [f] H = hyperfine magnetic field (±0.1), [g] RA = relative spectrum area (±0.2).

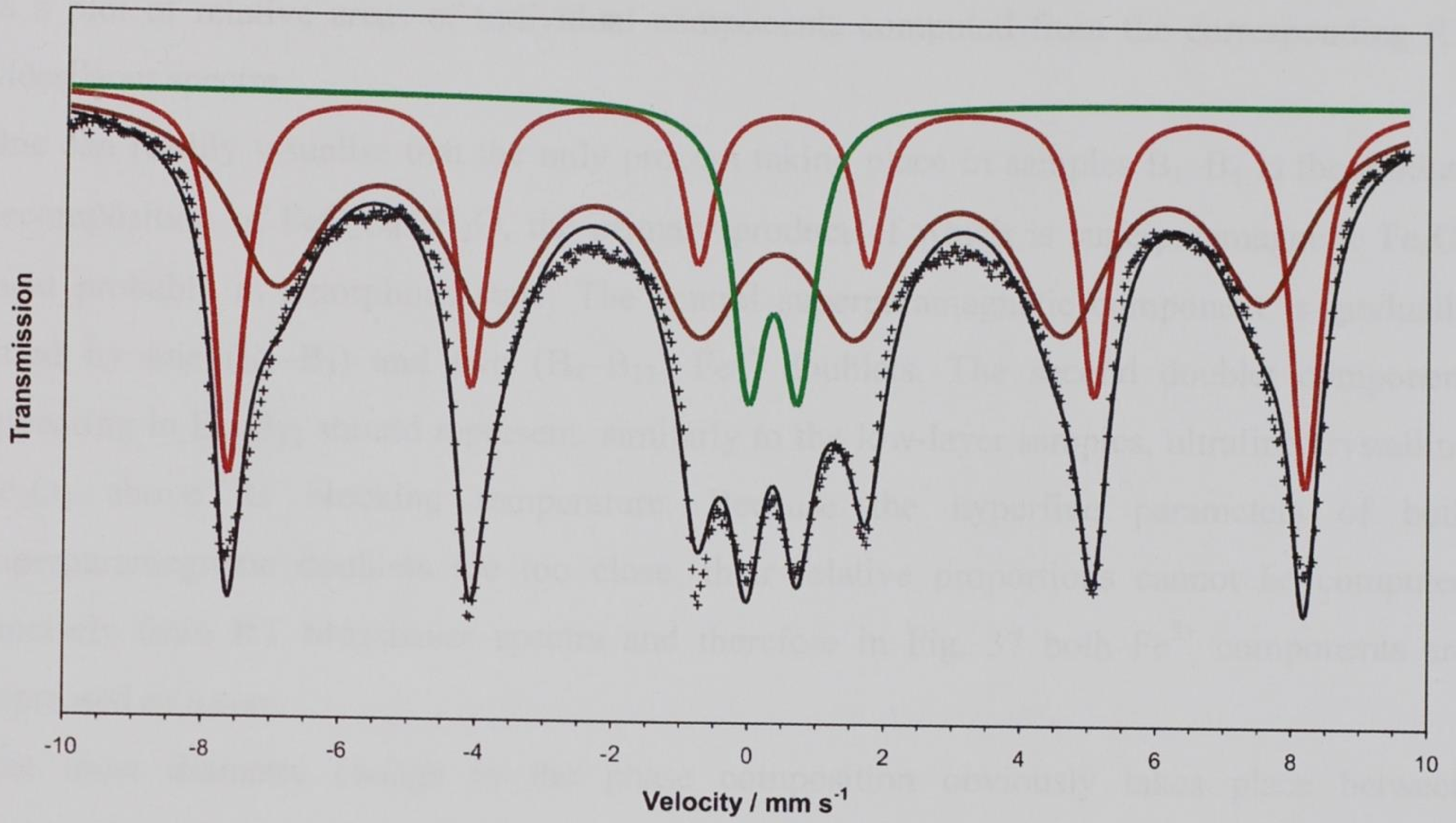

Fig. 36. Mössbauer spectrum of a high-layer sample (2.4 g) after 100 hrs of the isothermal treatment at 175 °C.

In Fig. 36 the Mössbauer spectrum of a sample isothermally treated for 100 hours is shown. It is obvious that this sample does not contain any remnants of ferrous oxalate dihydrate. It consists of one doublet and two sextet components representing superparamagnetic Fe_2O_3, hematite (the more magnetically split pattern; H = 49.1 T) and maghemite respectively. Hyperfine parameters of the above mentioned components are listed in Table 8. When compared to sample B_{12} one can clearly visualise a decrease of the content of SP Fe_2O_3 accompanied by a simultaneous increase of the contents of γ-Fe_2O_3 and α-Fe_2O_3. There is also apparent an increase of hyperfine magnetic fields of both magnetic components (41.9 *vs.* 45.0 T in the case of maghemite and 47.9 *vs.* 49.1 T in the case of hematite) evidencing their gradual crystallization.

Table 8 Hyperfine parameters of a sample (2.4 g) isothermally treated at 175 °C for 100 hrs.

δ/mm s^{-1a}	ΔE_Q/mm s^{-1b}	ε_Q/mm s^{-1c}	H/T^d	RA (%)^e	Site assignment
0.35	0.73	–	–	10.3	SP Fe_2O_3
0.38	–	−0.21	49.1	28.4	Hematite
0.35	–	0.10	45.0	61.3	Maghemite

^{a} δ = isomer shift (with respect to metallic iron, ±0.01), ^{b} ΔE_Q = quadrupole splitting (±0.01), ^{c} ε_Q = quadrupole shift (±0.01), ^{d} H = hyperfine magnetic field (±0.1), ^{e} RA = relative spectrum area (±0.2).

The phase composition of samples B_1–B_{12} is clearly demonstrated in Fig. 37. It is expressed as a plot of relative areas of individual components computed from the corresponding RT Mössbauer spectra.

One can readily visualise that the only process taking place in samples B_1–B_5 is the gradual decomposition of $FeC_2O_4 \cdot 2H_2O$, the primary product of which is superparamagnetic Fe_2O_3 most probably in amorphous state. The central superparamagnetic component is gradually fitted by one (B_1–B_3) and two (B_4–B_{12}) Fe^{3+} doublets. The second doublet component appearing in B_4–B_{12} should represent, similarly to the low-layer samples, ultrafine crystalline Fe_2O_3 above its blocking temperature. Because the hyperfine parameters of both superparamagnetic doublets are too close, their relative proportions cannot be computed precisely from RT Mössbauer spectra and therefore in Fig. 37 both Fe^{3+} components are expressed as a sum.

The most dramatic change in the phase composition obviously takes place between temperatures expressed by samples B_5 (177 °C) and B_6 (179 °C) – a very rapid fall of the ferrous oxalate dihydrate content is accompanied by the simultaneous creation of ferrimagnetic γ-Fe_2O_3. The question is, however, what the cause of the accompanying temperature increase is (see Fig. 34) – whether thermally induced oxidative decomposition of ferrous oxalate dihydrate towards ferrimagnetic maghemite as indicated in Fig. 37 or another process taking part between both superparamagnetic components and by the means of RT measurements therefore unexplainable.

To answer this question, low temperature in-field (IF) Mössbauer spectra ($T_{\text{meas}} = 50$ K, $B_{\text{ext}} = 5$ T) of samples B_5, B_6 and B representing the very beginning and the very end of the temperature effect respectively were measured. The Mössbauer spectra are shown in Fig. 38, hyperfine parameters are listed in Table 9.

IF Mössbauer spectrum of sample B_5 is fitted by two components. The huge central doublet belongs obviously to Fe^{2+} in undecomposed (44.5 %) ferrous oxalate structure. Isomer shift value of the sextet component (0.41 mm s^{-1}) is typical for Fe(III) oxides, a very low value of hyperfine magnetic field (32 T) could be ascribed to its amorphous character.[24] Moreover, enhanced 3rd and 4th lines obviously indicate the breaking point of the magnetic ordering – the transition from superparamagnetic to magnetically ordered state.

IF Mössbauer spectrum of sample B_6 exhibits a completely different shape. There is a remnant of the oxalate structure (4.7 %) represented by a broad central doublet. The magnetically split pattern is fitted by three sextets. The one with the lowest value of H (40 T) represents equally to the previous case (sample B_5) amorphous Fe_2O_3; an increase of the value of hyperfine magnetic field (from 32 to 40 T) could be ascribed to the more 'ordered' structure, which is achieved by the higher sample temperature. Hyperfine parameters of the two other sextet components are typical for distinguished tetrahedral (A) and octahedral (B) Fe^{3+} positions in maghemite structure (see Fig. 9). Not completely vanished 2nd and 5th lines of both sextets (for B positions more significantly due to present vacancies) indicate not precisely collinear spin arrangement. This arises as a consequence of a spin canting between bulk and surface of the particles as typical for ultrafine powders.

IF Mössbauer spectrum of sample B (the very end of the temperature effect) shows a completely split magnetic pattern. There are not any indications of the oxalate structure. Besides maghemite and amorphous Fe_2O_3, hyperfine magnetic field (44 T) and the shape of which indicate now a significant shift towards a nearly arranged crystal structure, there is another sextet present. The ratio of the line intensities of 3:4:1:1:4:3 (enhanced 2nd and 5th lines) indicate hematite structure as already discussed earlier (Section 5.5.1, Fig. 22, sample E_1).

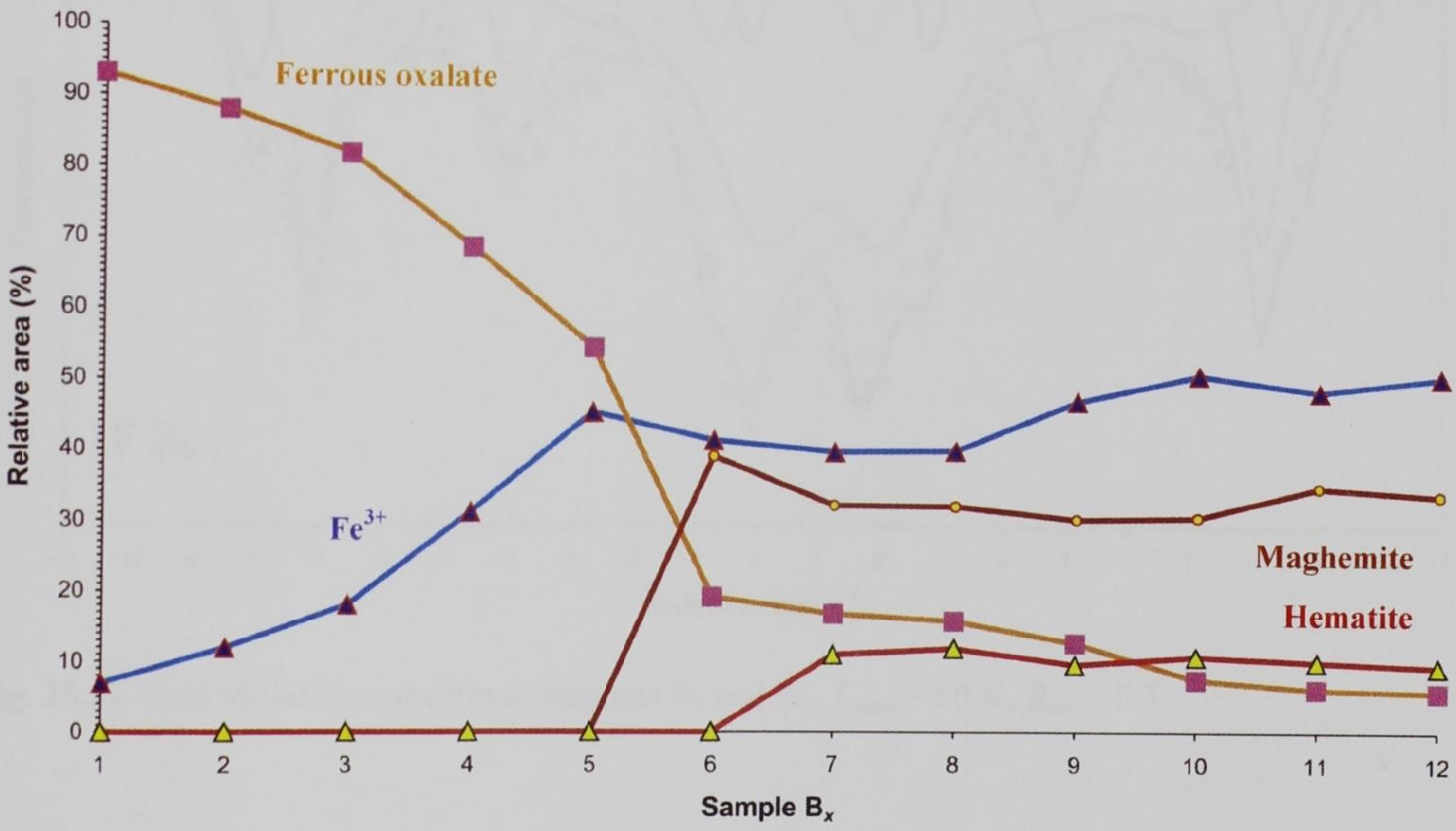

Fig. 37. Relative areas of the individual components from the RT Mössbauer spectra of the certain samples B_x (x = 1–12).

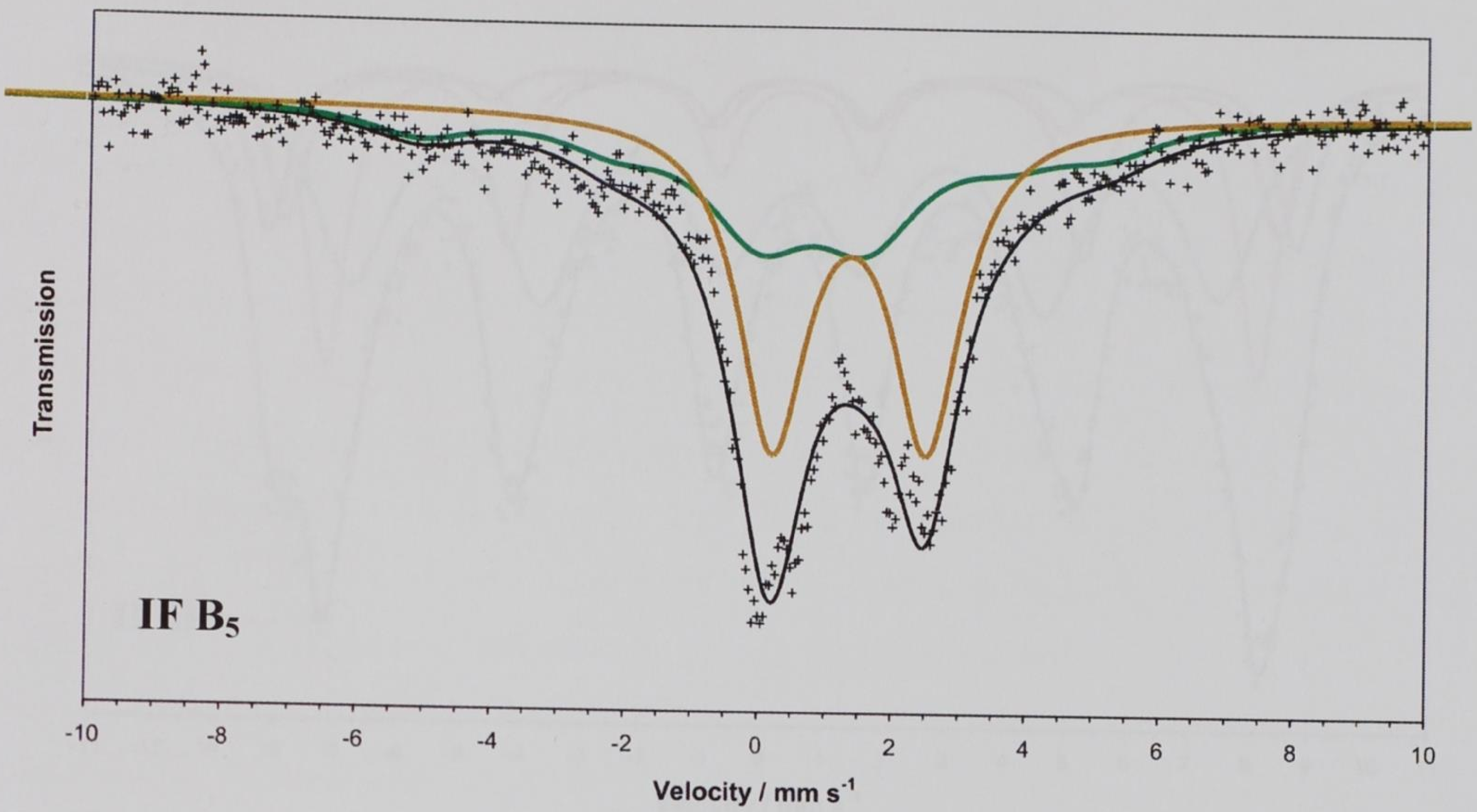

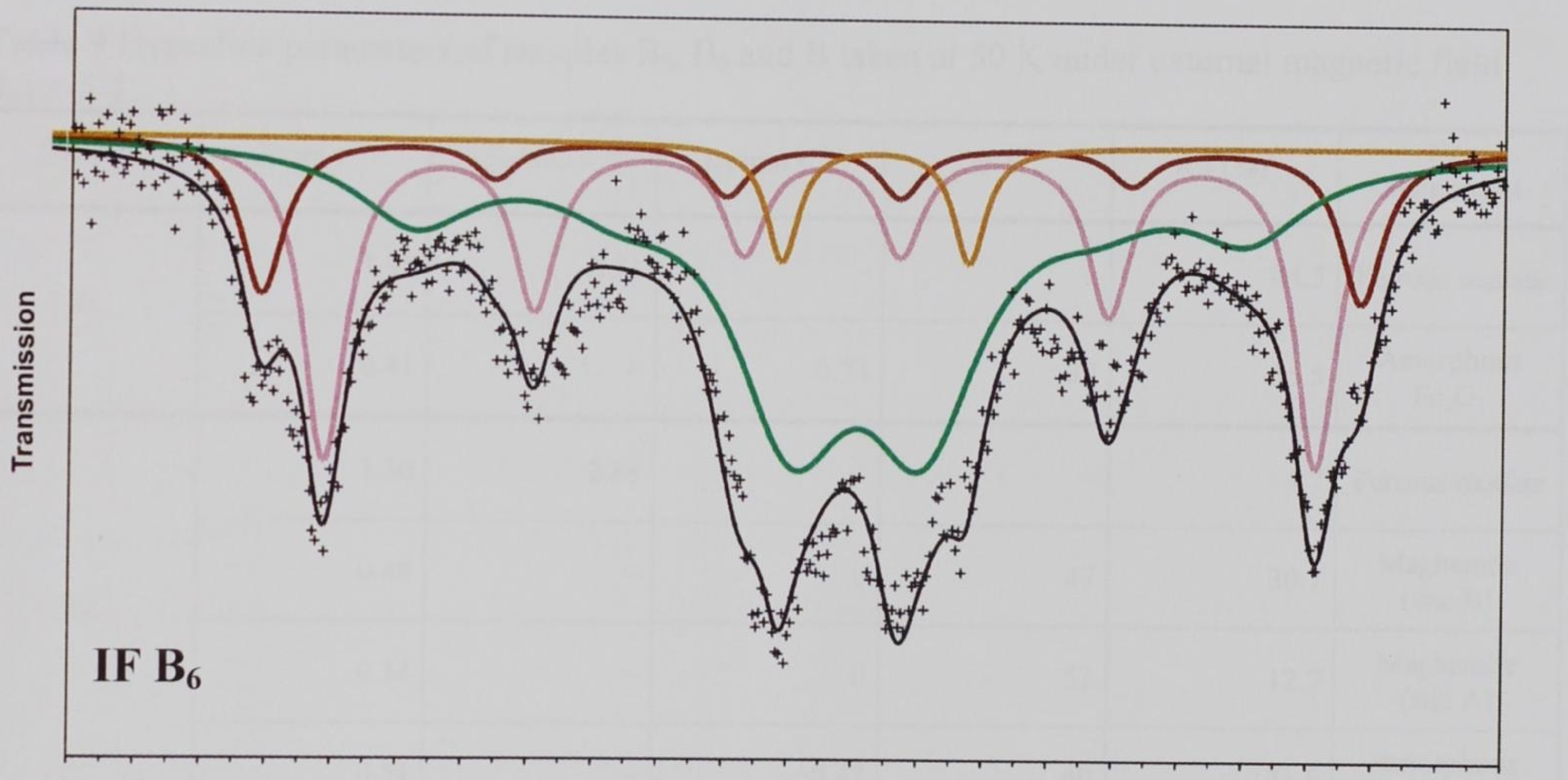

Fig. 38. In-field Mössbauer spectra of samples B_5 and B_6. T_{meas} = 50 K, B_{ext} = 5 T.

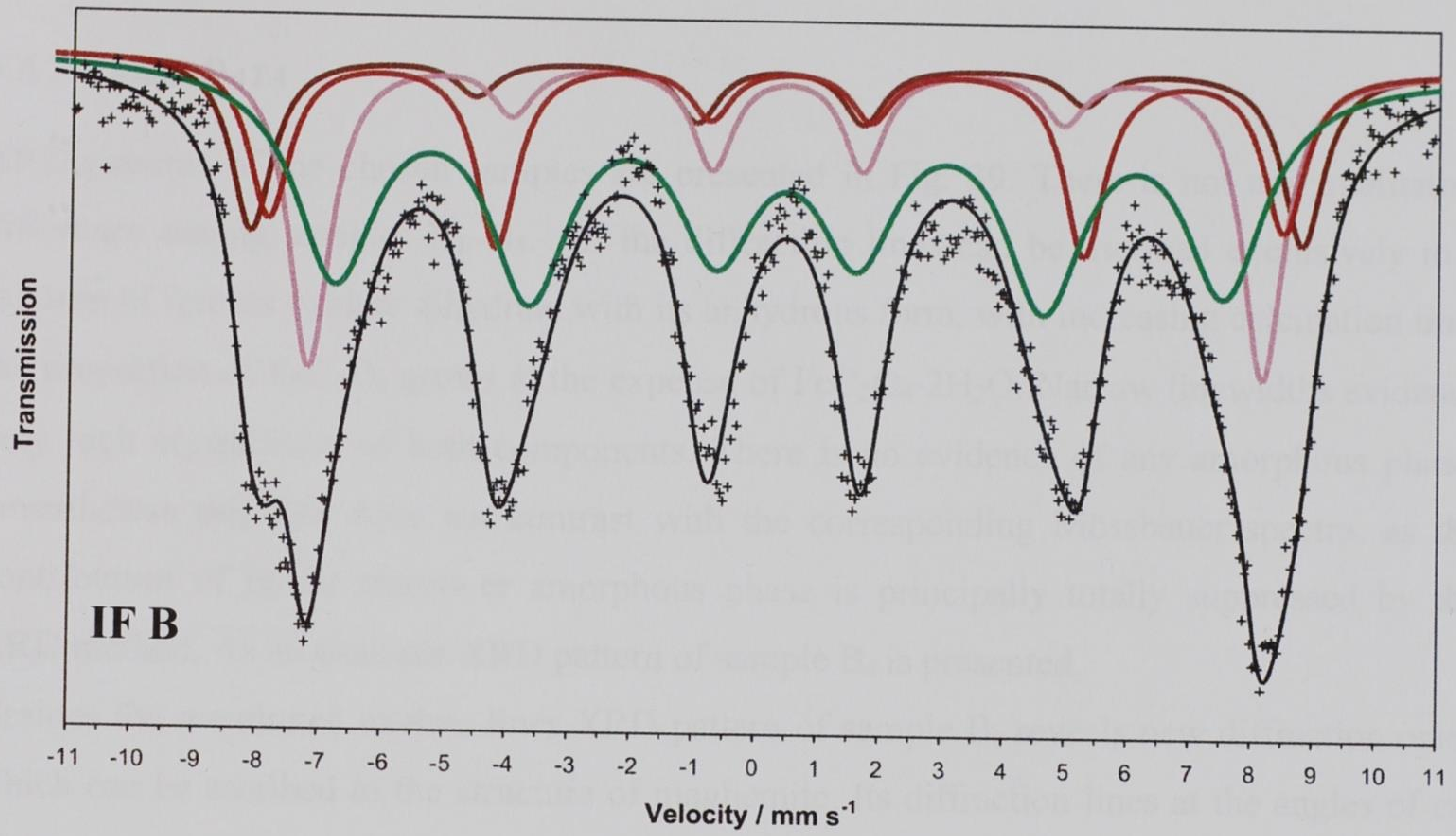

Fig. 38. In-field Mössbauer spectrum of sample B. $T_{\mathrm{meas}} = 50$ K, $B_{\mathrm{ext}} = 5$ T.

Table 9 Hyperfine parameters of samples B_5, B_6 and B taken at 50 K under external magnetic field $B_{\mathrm{ext}} = 5$ T.

Sample	δ/mm s^{-1a}	ΔE_Q/mm s^{-1b}	ε_Q/mm s^{-1c}	H/T^d	RA (%)^e	Site assignment
B_5	1.35	2.31	–	–	44.5	Ferrous oxalate
	0.41	–	0.74	32	55.5	Amorphous Fe_2O_3
B_6	1.30	2.88	–	–	4.7	Ferrous oxalate
	0.48	–	0	47	30.7	Maghemite (site B)
	0.34	–	0	52	12.7	Maghemite (site A)
	0.54	–	−0.42	40	51.9	Amorphous Fe_2O_3
B	0.48	–	0	47	18.4	Maghemite (site B)
	0.34	–	0.03	52	13.5	Maghemite (site A)
	0.42	–	−0.21	50	26.8	Hematite
	0.43	–	0.10	44	41.3	Amorphous Fe_2O_3

[a] δ = isomer shift (with respect to metallic iron, ±0.01), [b] ΔE_Q = quadrupole splitting (±0.01), [c] ε_Q = quadrupole shift (±0.01), [d] H = hyperfine magnetic field (±0.5), [e] RA = relative spectrum area (±0.5).

*5.6.2 **XRD DATA***

XRD patterns of the chosen samples are presented in Fig. 39. There is not any qualitative difference among samples B_1–B_5. All the diffraction lines can be ascribed exclusively to a mixture of ferrous oxalate dihydrate with its anhydrous form, with increasing calcination time the proportion of FeC_2O_4 grows at the expense of $FeC_2O_4 \cdot 2H_2O$. Narrow linewidths evidence very high crystallinity of both components. There is no evidence of any amorphous phase, nevertheless this fact does not contrast with the corresponding Mössbauer spectra, as the contribution of minor moreover amorphous phase is principally totally suppressed by the XRD method. As an example XRD pattern of sample B_4 is presented.

Besides the mentioned oxalate lines XRD pattern of sample B_6 reveals new diffraction ones, which can be ascribed to the structure of maghemite. Its diffraction lines at the angles of *ca.* 41.6° and 63.7° 2Θ overlap with those of hematite, but as the most intensive '100' diffraction line of hematite at 38.695° 2Θ in the pattern completely misses, it can be stated that α-Fe_2O_3 is not present in sample B_6 and except the oxalate structures maghemite is the only present crystalline phase in this sample.

XRD pattern of sample B_7 (not shown) reveals presence of another component, diffraction lines of which can be assigned to the hematite structure. Especially the '100' diffraction line standing alone at 38.695° 2Θ is the main characteristic feature allowing hematite identification in a pattern. Similarly to maghemite the diffraction lines of hematite are rather broad and less intensive compared to those belonging to the oxalate structures and indicate therefore quite poor crystallinity of the particles.

The XRD patterns of samples B_8, B_9, B_{10} (not shown), B_{11} (not shown) and B_{12} show identical phase composition as the previous sample (B_7). In these samples one can clearly visualize that the content of ferrous oxalate gradually decreases, gentle narrowing and growth of the diffraction lines of maghemite and hematite indicate then their growth and higher degree of crystallinity.

It can be stated that the phase composition observed by XRD entirely agrees with corresponding Mössbauer data.

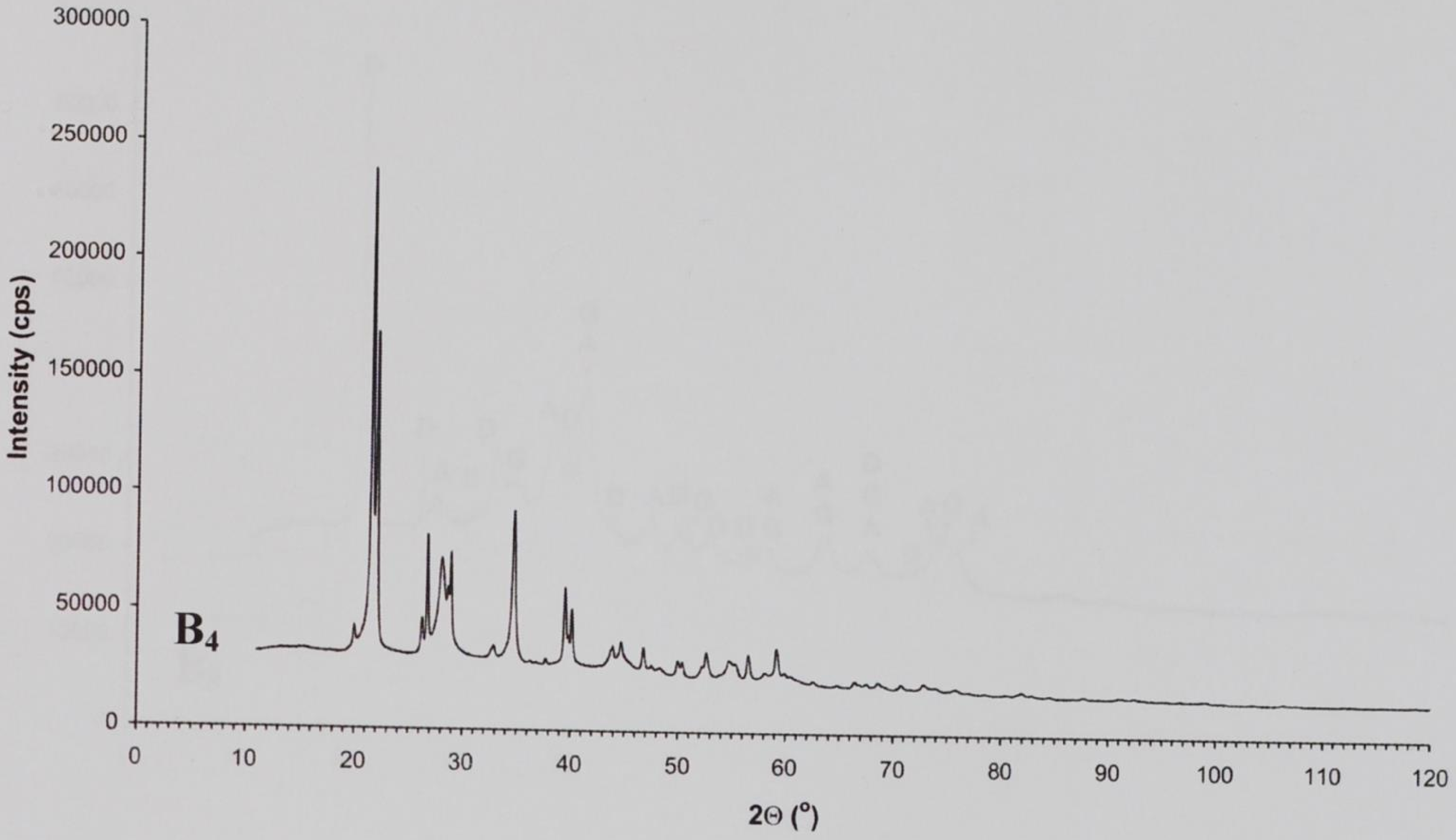

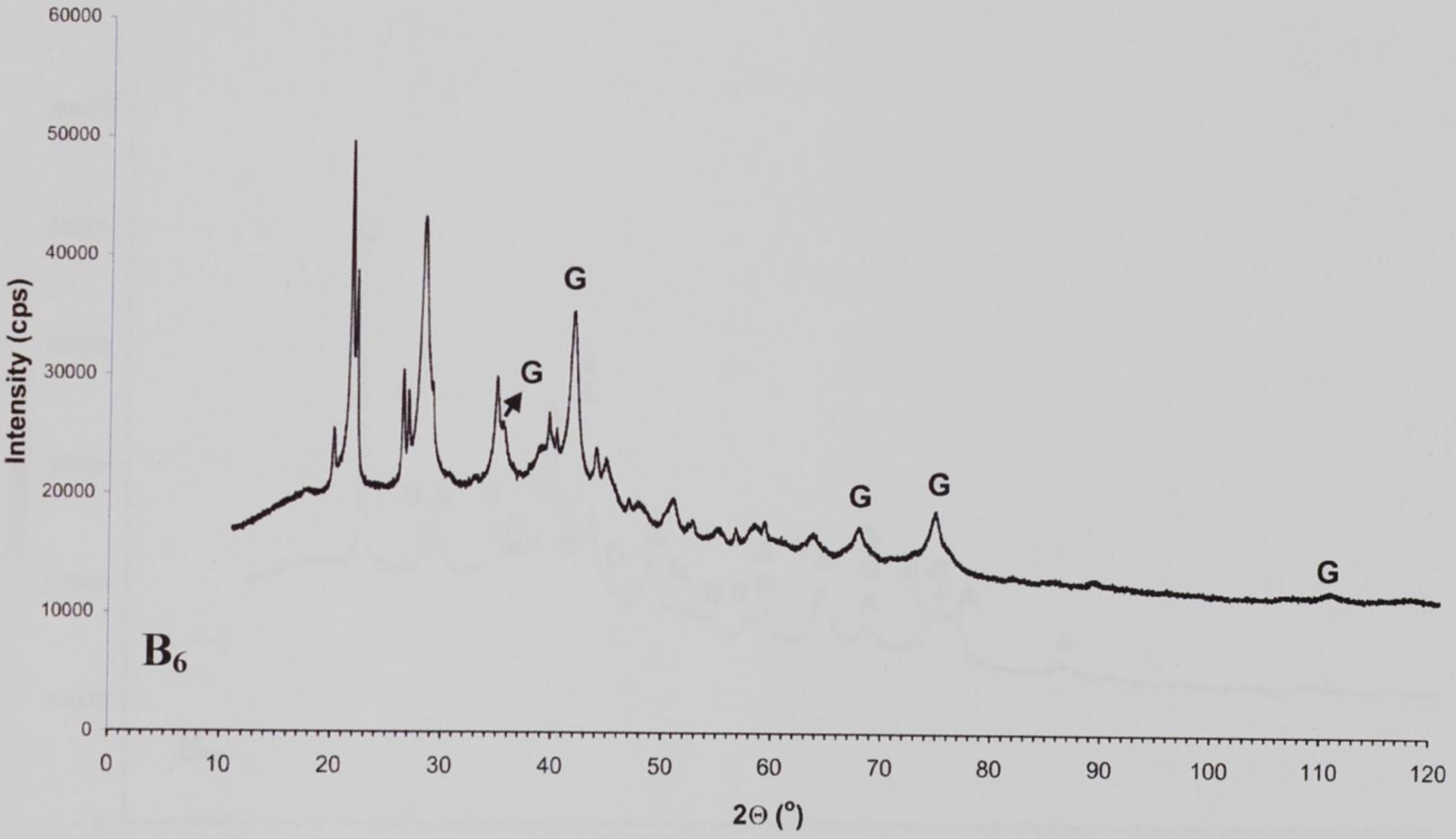

Fig. 39. XRD patterns of high-layer samples B_4 and B_6 (Assignment of individual phases: G – maghemite).

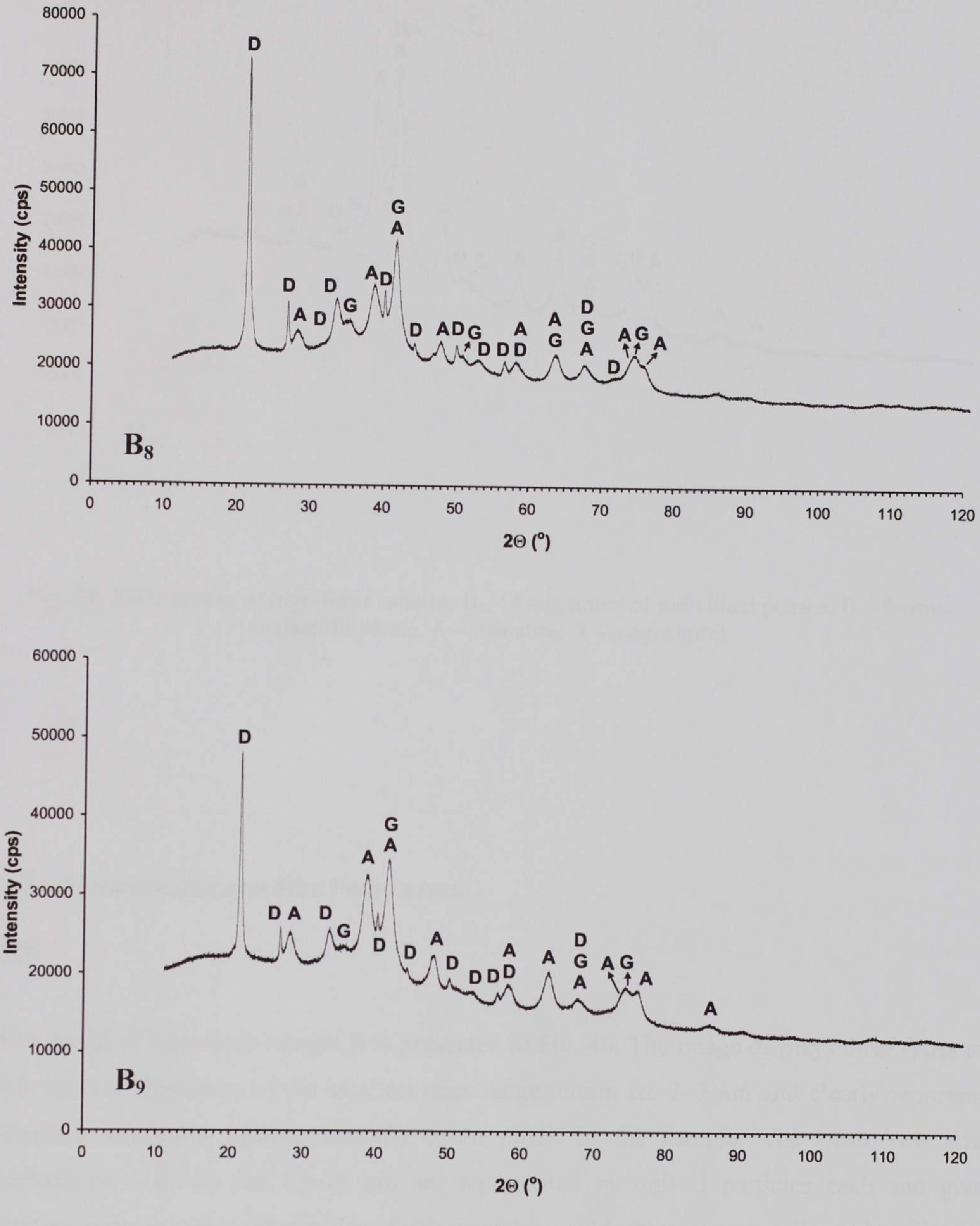

Fig. 39. XRD patterns of high-layer samples B_8 and B_9 (Assignment of individual phases: D – ferrous oxalate/dihydrate, A – hematite, G – maghemite).

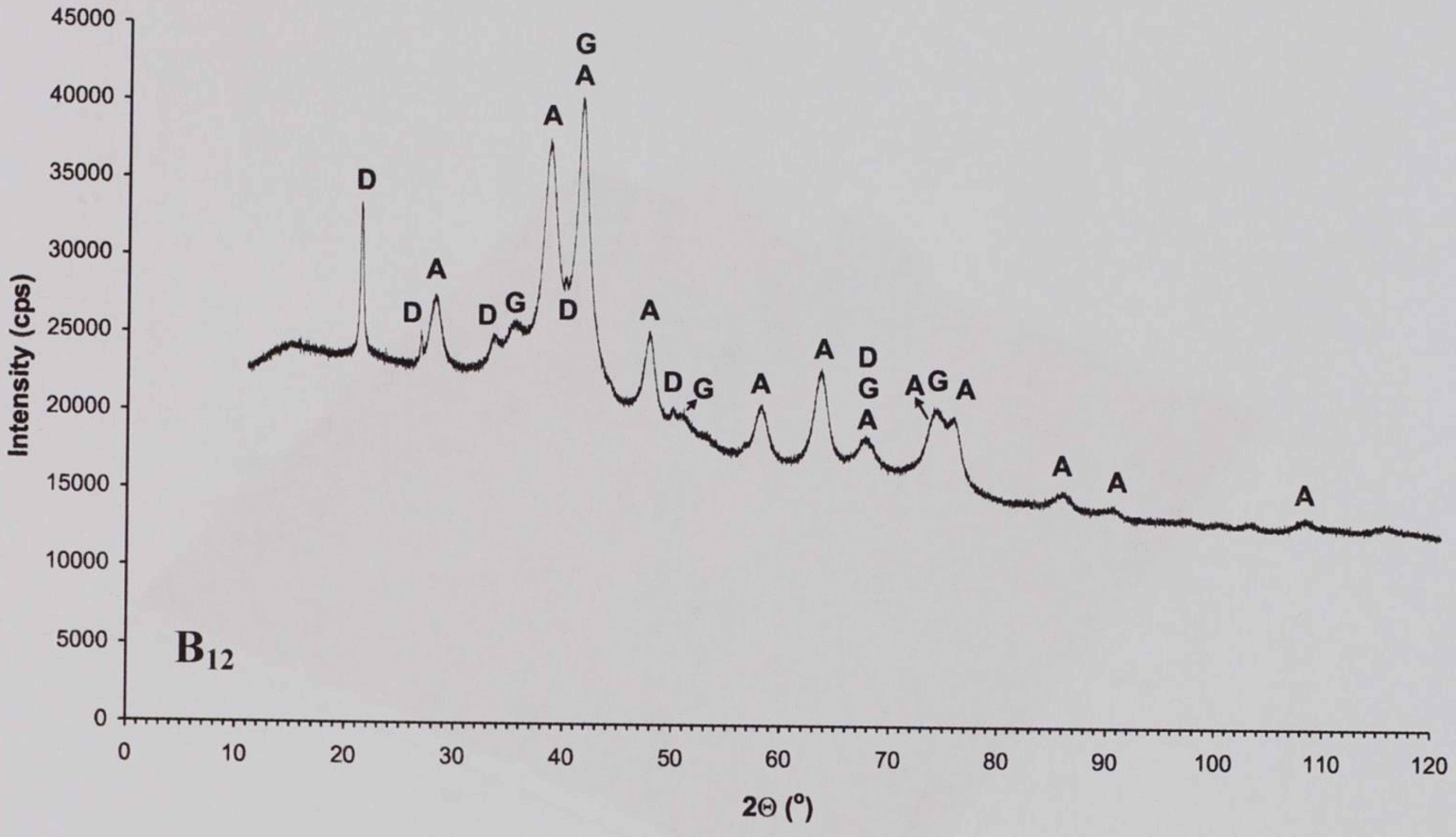

Fig. 39. XRD pattern of high-layer samples B_{12} (Assignment of individual phases: D – ferrous oxalate/dihydrate, A – hematite, G – maghemite).

5.6.3 *MORPHOLOGY AND SIZE PROPERTIES*

AFM

AFM image of high-layer sample B is presented in Fig. 40. The image displays three types of particles. The diameters of the smallest ones range within *ca.* 2–3 nm and clearly represent prevailing superparamagnetic iron(III) oxide phase in the sample. The other two size distributions 5–8 nm and 15–19 nm are represented by only 3 particles each and give therefore only intuitive information. Such particles could represent crystalline phase in the sample – the smaller ones maghemite and the bigger ones hematite particles.

It should be also mentioned that in the case of high-layer samples we again dealt with different results given by AFM and TEM concerning the overall character of a sample (see next section).

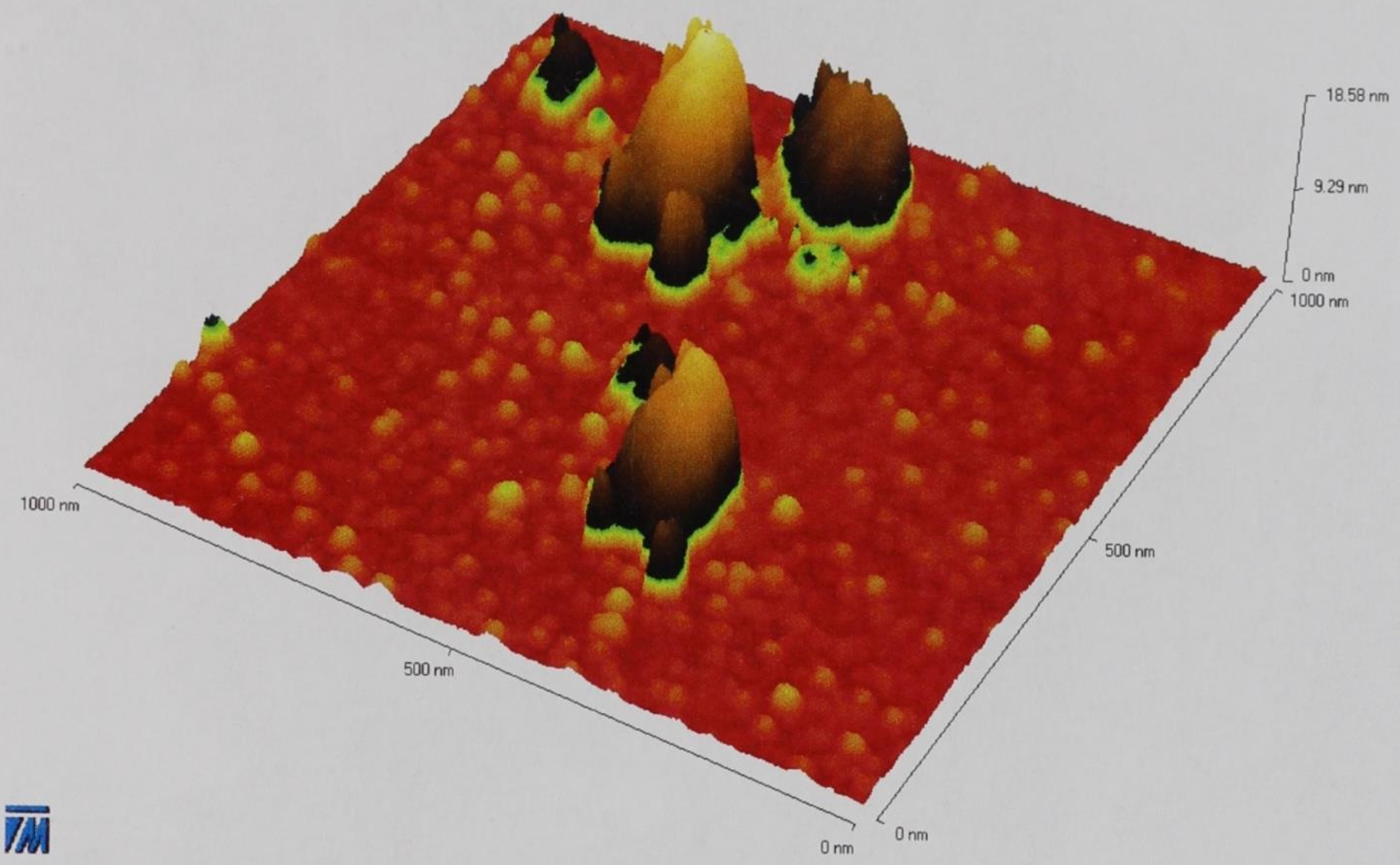

Fig. 40. AFM image of sample B.

TEM

TEM images of sample B are shown in Figs. 41 and 42. The overall character of the sample (Fig. 41) is very similar to that observed in the case of the low-layer samples and discussed earlier. From the magnified image (Fig. 42) it is apparent, however, that the large objects of oxalate-like-shape consist of various dimensional fractions ranging within *ca.* 3–20 nm. From the viewpoint of the morphology, small spherical particles (below 10 nm) could be assigned to superparamagnetic Fe_2O_3, whilst bigger (10–20 nm) spherical and hexagonal ones clearly represent crystalline maghemite and hematite respectively. Such a result agrees well with the phase composition predicted from Mössbauer spectroscopy and XRD.

Fig. 41. TEM image of high-layer sample B. An overall view.

Fig. 42. TEM image of high-layer sample B. A detailed view.

5.6.4 APPLICABILITY

As it has been mentioned earlier all the samples B_6–B_{12} showed strong magnetic behaviour. Such a property predestines their possible use especially for magnetic applications. Sample B_6 consists only of maghemite with a certain proportion of $FeC_2O_4{\cdot}2H_2O$ (*ca.* 19 %, see Table

7), which is soluble in water. In Fig. 43 a Mössbauer spectrum of sample B_6 after the process of rinsing (B_{6R}) is shown. It is apparent that as-prepared sample does not contain any remnants of the precursor and consists exclusively of maghemite in crystalline and superparamagnetic forms (hyperfine parameters are listed in Table 10). So prepared material has been recently tested in several applications. The best result has so far been obtained when tested as a possible MRI (Magnetic Resonance Imaging) agent. Fig. 44 shows a result of such a test. Contrasting properties of five plus one (pure water as a background) samples were tested. One can readily visualise that sample B_{6R} is the best contrasting material in this test. These days excellent contrasting properties are achieved by a mixture of bentonite just with sample B_{6R}.

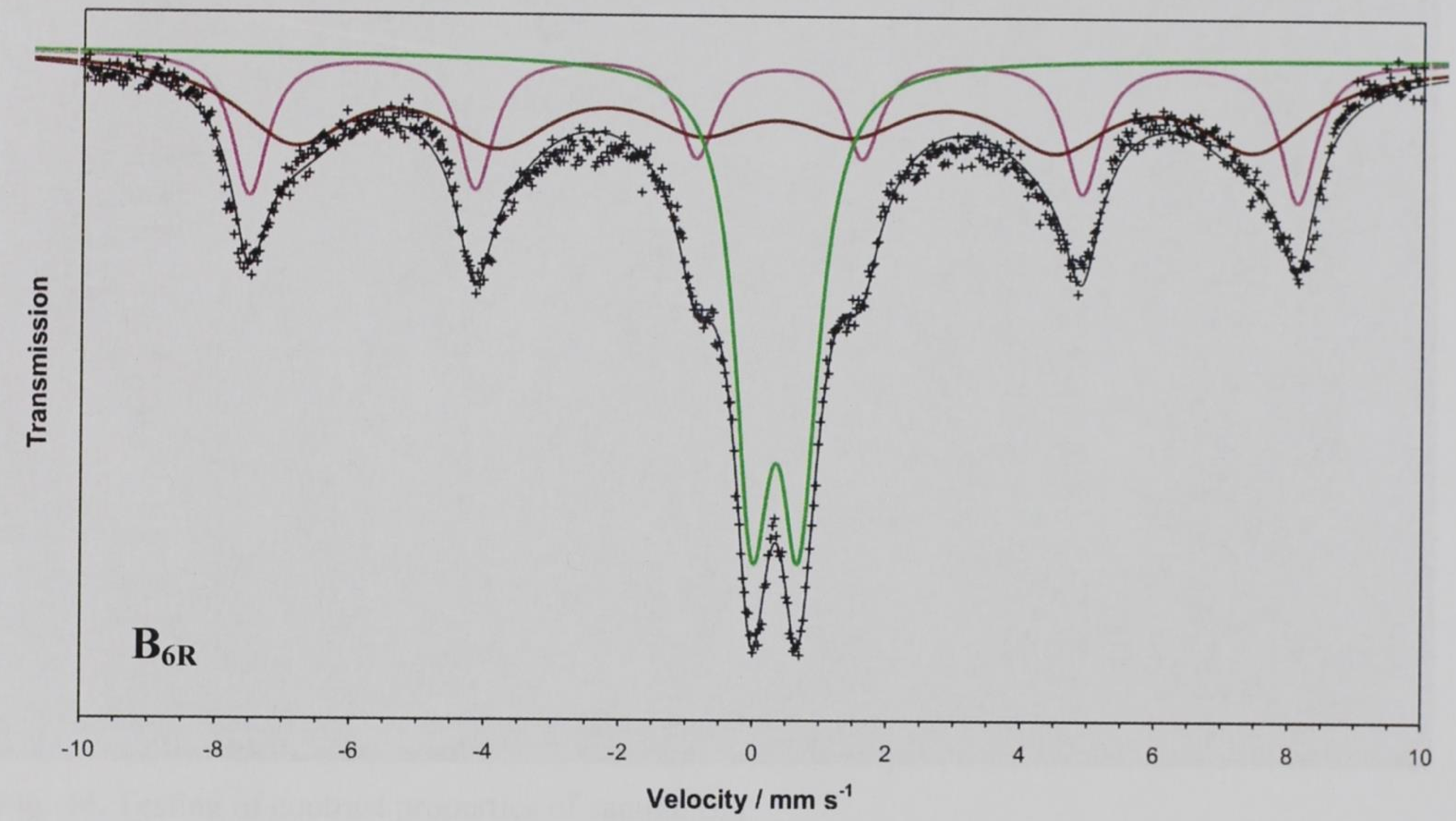

Fig. 43. Mössbauer spectrum of sample B_{6R} (sample B_6 after the process of rinsing).

Table 10 Hyperfine parameters of a sample B_{6R}.

δ/mm s^{-1a}	ΔE_Q/mm s^{-1b}	ε_Q/mm s^{-1c}	H/T^d	RA (%)^e	Site assignment
0.33	0.70	–	–	29.2	SP maghemite
0.32	–	0.06	48.6	24.7	Maghemite bulk
0.30	–	0.02	44.6	46.1	Maghemite surface

^{a} δ = isomer shift (with respect to metallic iron, ±0.01), ^{b} ΔE_Q = quadrupole splitting (±0.01), ^{c} ε_Q = quadrupole shift (±0.01), ^{d} H = hyperfine magnetic field (±0.1), ^{e} RA = relative spectrum area (±0.2).

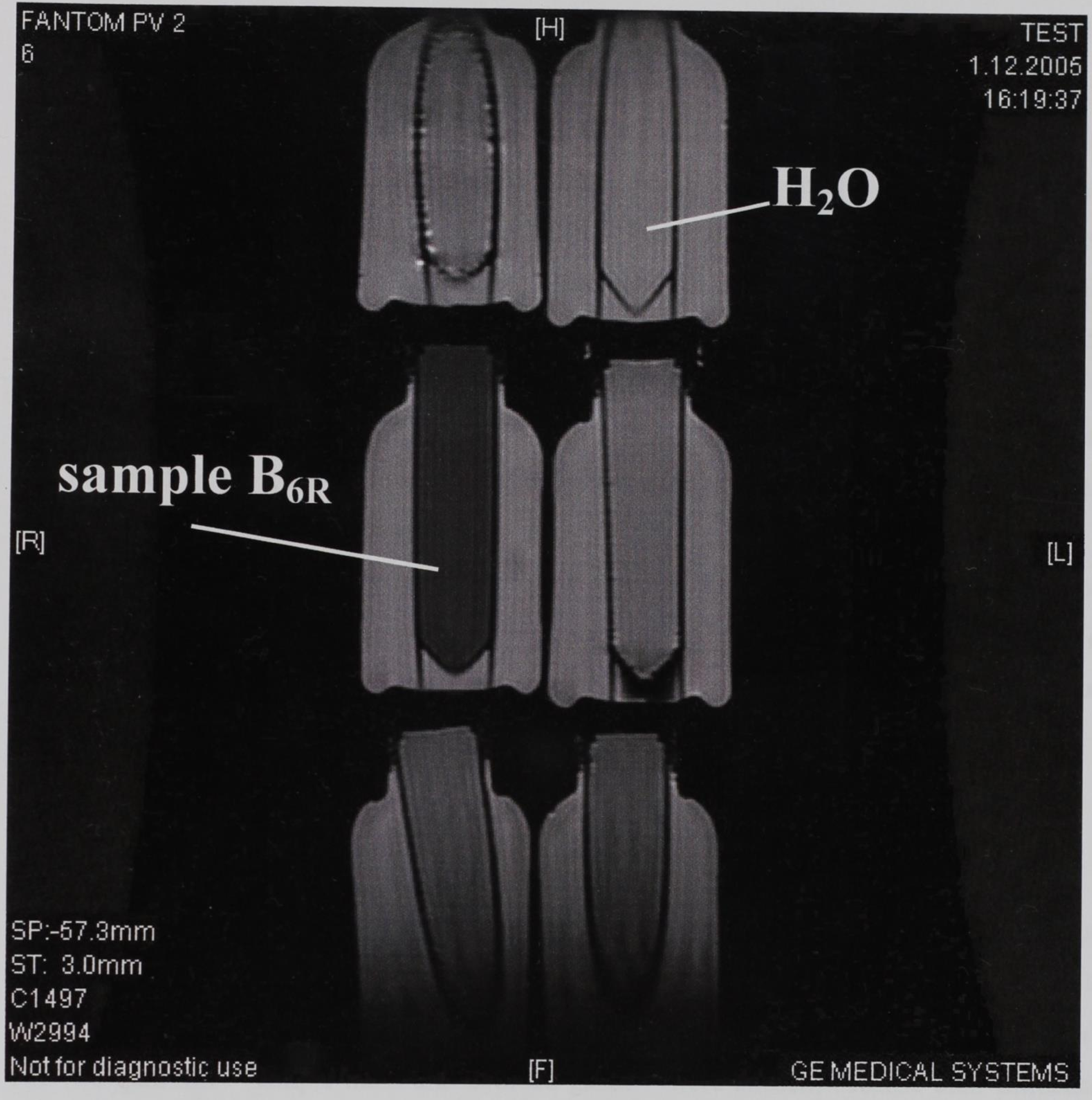

Fig. 44. Testing of contrast properties of sample B_{6R}.

5.6.5 Conclusion

On the grounds of the discussed results it can be concluded that the primary product of the thermally induced decomposition of $FeC_2O_4 \cdot 2H_2O$ in air, when the sample mass (the layer of the precursor) is above a certain critical value is **amorphous Fe_2O_3** with diameters ranging within 2–3 nm equally to the case of the low layer. With increasing calcination time $FeC_2O_4 \cdot 2H_2O$ gradually decomposes (see Fig. 37 up to point 5) and just in the moment when there is enough amorphous material within the sample volume, **collective crystallization** process towards superparamagnetic γ-Fe_2O_3 takes place as evidenced by IF Mössbauer spectra. The crystallization process is accompanied by a massive increase of the temperature within the sample, which accelerates the decomposition of the oxalate structure (Fig. 37, between points 5 and 6). The temperature increase accelerates also the crystallization itself; bigger particles are formed, and size induced transformation **superparamagnetic γ-Fe_2O_3 → ferrimagnetic γ-Fe_2O_3 → α-Fe_2O_3** takes place. However, the amount of the created energy is limited, which is evidenced by the almost ceased change in the phase composition between points 7–12 in Fig. 37. When compared to the phase composition of sample B_{12}, phase composition observed from the Mössbauer spectrum of a sample taken after 100 hrs of the isothermal treatment (Fig. 36) evidences only slow crystallization process resulting in the formation of ferrimagnetic maghemite as a prevailing component (*ca.* 60 %).

From the morphological point of view TEM images evidence form of the material similar to that observed in the case of low-layer samples: oxalate-like objects made of smaller well resolved particles of different shapes and sizes.

As already mentioned all the samples consist predominantly of maghemite and exhibit therefore strong magnetism. Sample B_6 evidences that when the decomposition process is stopped at the very beginning of the temperature effect, after rinsing pure nanomaghemite can be prepared. Such a material is suitable for example as a contrast agent in MRI.

6 Summary

The general aim of the presented work has been to study the influence of the sample mass and participation of evolving gases on the thermally induced decomposition of ferrous oxalate dihydrate ($FeC_2O_4 \cdot 2H_2O$), by which Fe_2O_3 used in many applications is generally formed. The two qualities – sample mass and evolved gases – were chosen, because their influence had never been adequatelly studied. The literature discrepancies however indicated that their impact on the decomposition process could be substantial. The obtained results can be summarized as follows:

1.

Thermal decomposition of $FeC_2O_4 \cdot 2H_2O$ in the atmosphere of the conversion gases proceedes in five steps:

I. $FeC_2O_4 \cdot 2H_2O \rightarrow FeC_2O_4 + 2H_2O$

II. $3FeC_2O_4 \rightarrow Fe_3O_4 + 4CO + 2CO_2$

III. $3FeC_2O_4 + 2CO \rightarrow Fe_3C + 7CO_2$

IV. $Fe_3C \rightarrow 3Fe + C$

V. $Fe_3O_4 + CO \rightarrow 3FeO + CO_2$

On the grounds of the equations it could be concluded that evolved gases (especially reducing ones) substantially influence the decomposition mechanism. More importantly, such a result obtained for ferrous oxalate dihydrate can be generalized and should be always strongly considered when studying solid-state reactions.

Moreover, reactions II, III and IV could serve as guides for simple syntheses of magnetic Fe_3O_4, Fe_3C and α-Fe respectively.

2.

It was observed that the decomposition process of $FeC_2O_4{\cdot}2H_2O$ in air proceeds in two very different ways concerning the phase composition depending on the weight of the precursor (the layer, which the precursor occupies in a certain experimental arrangement).

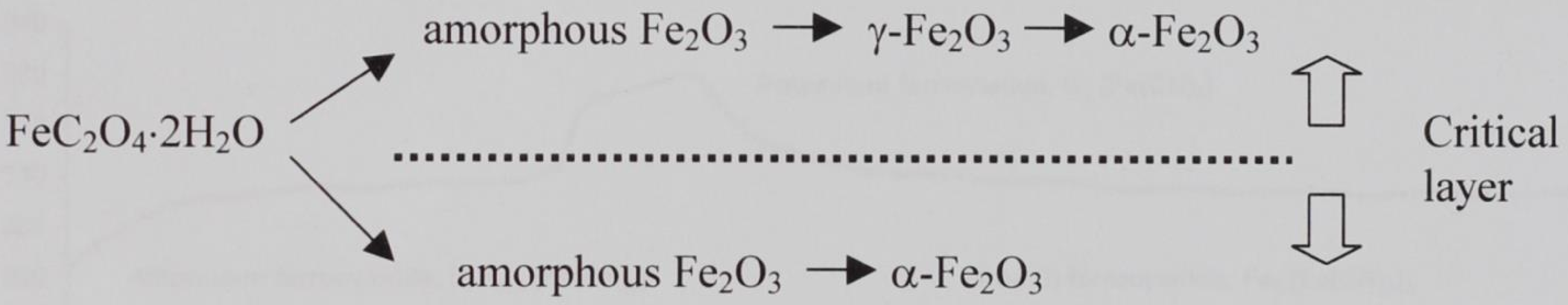

When the sample mass is lower than a certain critical one (its layer is below a certain critical layer), primary product of the decomposition is amorphous Fe_2O_3, which exhibits enormous values of specific surface area of *ca.* 400 $m^2\ g^{-1}$. With increasing calcination time amorphous Fe_2O_3 gradually crystallizes and superparamagnetic hematite is formed. Materials with certain advantageous combination of specific surface area and degree of crystallinity exhibit excellent catalytic activity. Hematite is the only crystalline decomposition product.

In the opposite case, when the weight of $FeC_2O_4{\cdot}2H_2O$ is higher than the critical one (high-layer samples), amorphous Fe_2O_3 is the primary decomposition product too. Mössbauer spectra and XRD evidence that the decomposition process is very slow. However, when there is a certain sufficient amount of amorphous phase in the sample, collective crystallization of amorphous Fe_2O_3 takes place and superparamagnetic γ-Fe_2O_3 is formed. The crystallization is accompanied by a consequent increase of sample temperature and both the decomposition and crystallization processes are accelerated and particle size induced transformations take place. In the first stage, only ferrimagnetic γ-Fe_2O_3 is formed. Such a material consisting solely of superparamagnetic and ferrimagnetic maghemites was successfully tested as a possible contrast agent for MRI. In the second stage, with a next increase of the sample temperature, a certain proportion of maghemite converts to hematite.

7 Outlook

The most recent results indicate that an increase of a sample temperature accompanying thermally induced decompositions is a general phenomenon, which for the time being has been observed in the case of four other precursors (see Fig. 45). The monitoring of a sample temperature seems to be a revolutionary step enabling direct observation of a crystallization process and therefore allowing successful distinguishing between amorphous and nanocrystalline phases, which has up to now proved to be very problematic.

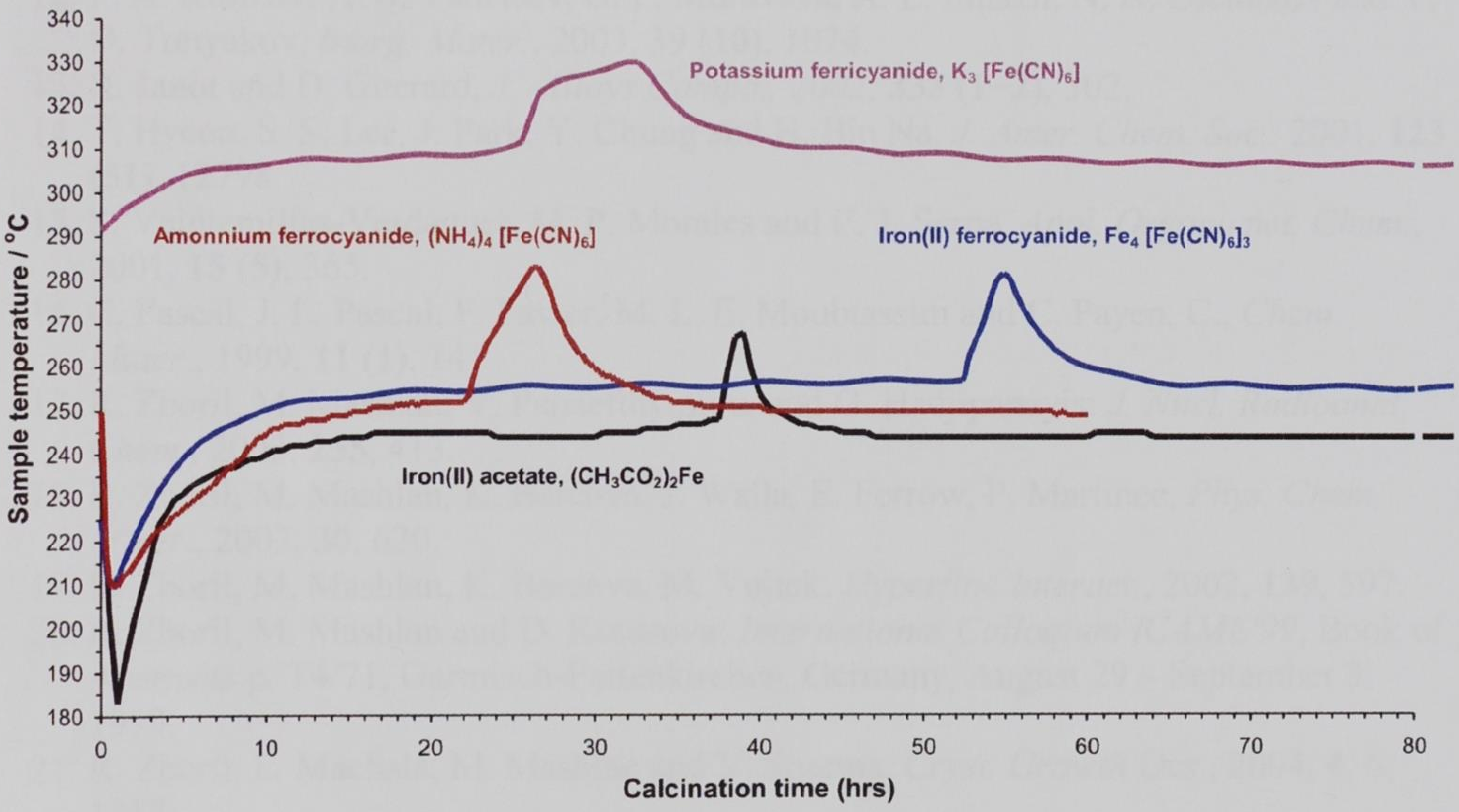

Fig. 45. Temperature records of the thermal decompositions of four samples: potassium ferricyanide, ammonium ferrocyanide, iron(II) ferrocyanide and iron(II) acetate.

8 References

1. R. M. Cornell and U. Schwertmann, *The Iron Oxides,* VCH, Weinheim, Germany, 1996.
2. R. Zboril, M. Mashlan and D. Petridis: *Chem. Mater.*, 2002, **14**, 969.
3. A. B. Bourlinos, R. Zboril and D. Petridis, *Microporous Mesoporous Mater.*, 2003, **58**, 155.
4. J. Tuček, R. Zboril and D. Petridis, *J. Nanosci. Nanotechnol.*, 2006, **6**, 926.
5. Z. M. Wang, Y. Liu and X. Y. Zeng, *Powder Technol.,* 2006, **161 (1),** 65.
6. Y. Zhou, Z. J. Zhang and Y. Yue, *Mater. Lett.*, 2005, **59 (27),** 3375.
7. K. Deshpande, M. Nersesyan, A. Mukasyan and A. Varma, *Ind. Eng. Chem. Res.*, 2005, **44 (16)**, 6196.
8. D. Makovec, A. Kosak, A. Znidarsic and M. Drofenik, *J. Magn. Magn. Mater.,* 2005, **289**, 32.
9. K. Woo and H. J. Lee, *On the Convergence of Bio-Information-, Environmental-, Energy-, Space- and Nano-Technologies, PTS 1 and 2*, 2005, **876**, 277.
10. S. J. Lee, J. R. Jeong, S. C. Shin, J. C. Kim and J. D. Kim, *J. Magn. Magn. Mater.*, 2004, **282**, 147.
11. M. Popovici, M. Gich, A. Roig, L. Casas, E. Molins, C. Savii, D. Becherescu, J. Sort, S. Surinach, J. S. Munoz, M. D. Baro and J. Nogues, *Langmuir*, 2004, **20 (4)**, 1425.
12. F. A. Kulikov, A. S. Vanetsev, G. P. Muraveva, A. L. Ilinskii, N. N. Oleinikov and Y. D. Tretyakov, *Inorg. Mater.*, 2003, **39 (10)**, 1074.
13. R. Janot and D. Guerard, *J. Alloys Compd.,* 2002, **333 (1−2)**, 302.
14. T. Hyeon, S. S. Lee, J. Park, Y. Chung and H. Bin Na, *J. Amer. Chem. Soc.,* 2001, **123 (51)**, 12798.
15. S. Veintemillas-Verdaguer, M. P. Morales and C. J. Serna, *Appl. Organomet. Chem.*, 2001, **15 (5)**, 365.
16. C. Pascal, J. L. Pascal, F. Favier, M. L. E. Moubtassim and C. Payen, C., *Chem. Mater.*, 1999, **11 (1)**, 141.
17. R. Zboril, M. Mashlan, V. Papaefthymiou, and G. Hadjipanayis: *J. Nucl. Radioanal. Chem.*, 2003, **255**, 413.
18. R. Zboril, M. Mashlan, K. Barcova, J. Walla, E. Ferrow, P. Martinec, *Phys. Chem. Miner*., 2003, **30**, 620.
19. R. Zboril, M. Mashlan, K. Barcova, M. Vujtek: *Hyperfine Interact.*, 2002, **139**, 597.
20. R. Zboril, M. Mashlan and D. Krausova: *International Colloqium ICAME'99*, Book of Abstracts p. T4/71, Garmisch-Partenkirchen, Germany, August 29 – September 3, 1999.
21. R. Zboril, L. Machala, M. Mashlan and V. Sharma, *Cryst. Growth Des.*, 2004, **4**, 6, 1317.
22. R. Zboril, M. Mashlan, L. Machala, J. Walla, K. Barcova and P. Martinec, *Hyperfine Interact*., 2004, **156**, 403.
23. R. Zboril, L. Machala, M. Mashlan, J. Tucek, R. Muller and O. Schneeweiss, *Phys. Status Solidi C*., 2004, **1**, 3710.
24. L. Machala, R. Zboril and A. Gedanken, *Nanotechnology*, being reviewed.
25. E. Murad and J. Cashion, *Mössbauer Spectroscopy of Environmental Materials and their Industrial Utilization*, Kluwer Academic Publishers, Boston, U. S. A., 2004.
26. S. Mitra, *Applied Mössbauer spectroscopy – Theory and Practice for Geochemists and Archeologists*, Pergamon Press, Oxford, UK, 1992.

27. G. J. Long and F. Grandjean, *Mössbauer Spectroscopy Applied to Magnetism and Materials Science*, Volume 1, Plenum Press, New York, U.S.A., 1993.
28. C. J. Cong, L. Liao, J. C. Li, L. X. Fan and K. L: Zhang, *Nanotechnology*, 2005, **16 (6)**, 981.
29. M. E. Mendoza, F. Donado, R. Silva, M. A. Pérez and J. L. Carrillo, *J. Phys. Chem. Solids*, 2005, **66 (6)**, 927.
30. K. F. Zhang, X. Z. Sun, G. W. Lou, X. Liu, H. L. Li and Z. X. Su, *Mater. Lett.*, 2005, **59 (22)**, 2729.
31. N. Audebrand, S. Raite and D. Louer, *Solid State Sci.*, 2003, **5 (5)**, 783.
32. E. Jeanneau, N. Audebrand and D. Louer, *J. Solid State Chem.,* 2003, **173 (2)**, 387.
33. C. Drouet and P. Alphonse, *J. Mater. Chem.*, 2002, **12 (10)**, 3058.
34. E. Jeanneau, N. Audebrand and D. Louer, *J. Mater. Chem.*, 2002, **12 (8)**, 2383.
35. C. Boudaren, J. P. Auffredic, P. Benard-Rocherulle and D. Louer, *Solid State Sci.*, 2001, **3 (8)**, 847.
36. S. Dash, R. Krishnan, M. Kamruddin, A. K. Tyagi and B. Raj, *J. Nucl. Mater.*, 2001, **295 (2−3)**, 281.
37. V. Carles, C. Laurent, M. Brieu and A. Rousset, *J. Mater. Chem.*, 1999, **9 (4)**, 1003.
38. N. Audebrand, J. P. Auffredic and D. Louer, *Chem. Mater.*, 1998, **10 (9)**, 2450.
39. J. H. Choy, Y. S. Han and S. J. Kim, *J. Mater. Chem.*, 1997, **7 (9)**, 1807.
40. X. S. Li, L. Y. Chen, C. Y. Xie, Y. F. Miao, D. M. Li and Q. Xin, *Thermochim. Acta,* 1995, **260**, 115.
41. M. Insausti, M. K. Urtiaga, R. Cortes, J. L. Mesa, M. I. Arriortua and T. Rojo, *J. Mater. Chem.*, 1994, **4 (12)**, 1867.
42. P. K. Dutta, P. K. Gallagher and J. Twu, *Chem. Mater.*, 1993, **5 (12)**, 1739.
43. V. Rao, A. L. Shashimohan and A. B. Biswas, *J. Mater. Sci.*, 1974, **9**, 430.
44. B. Boyanov, D. Khadzhiev and V. Vasilev, *Thermochim. Acta*, 1985, **93**, 89.
45. K. S. Rane, A. K. Nikumbh and A. J. Mukhedkar, *J. Mater. Sci.*, 1981, **16**, 2387.
46. M. Popa, J. M. Calderon-Moreno, D. Crisan and M. Zaharescu, *J. Therm. Anal. Calorim.*, 2000, **62**, 633.
47. A. S. Brar and K. S. Khabre, *Indian J. Chem.*, 1982, **21A**, 920.
48. R. Zboril, L. Machala, M. Mashlan, M. Hermanek, M. Miglierini and A. Fojtik, *phys. stat. sol. (c)*, 2004, **1**, 3583.
49. V. Chhabra, M. Lal, A. N. Maitra and P. Ayyub, *Colloid Polym. Sci.,* 1995, **273**, 939.
50. V. Borker, K. S. Rane and V. N. Kamat Dalal, *J. Mater. Sci .- Mater. Electron.*, 1993, **4**, 241.
51. R. A. Brown and S. C. Bevan, *J. Inorg. Nucl. Chem.*, 1966, **28**, 387.
52. M. A. Mohamed and A. K. Galwey, *Thermochim. Acta*, 1993, **213**, 269.
53. M. R. Anantharaman, S. S. Shewale, V. S. Rao, K. Seshan and H. V. Keer, *Indian J. Chem.*, 1982, **21A**, 990.
54. V. Carles, P. Alphonse, P. Tailhades and A. Rousset, *Thermochim. Acta*, 1999, **334**, 107.
55. Y. Kong, D. Xue and F. Li, *phys. stat. sol. (a)*, 1996, **154**, 553.
56. F. Li, Y. Kong and D. Xue, *phys. stat. sol. (a)*, 1995, **148**, 129.
57. N. N. Mallikarjuna, B. Govindaraj, A. Lagashetty and A. Venkataraman, *J. Therm. Anal. Calorim.,* 2003, **71**, 915.
58. Ll. Casas, A. Roig, E. Molins, J. M. Greneche, J. Asenjo and J. Tejada, *Appl. Phys. A*, 2002, **74**, 591.
59. A. Peigney, P. Coquay, E. Flahaut, R. E. Vandenberghe, E. De Grave and C. Laurent, *J. Phys. Chem. B*, 2001, **105 (40)**, 9699.

60. S. Herreyre, P. Gadelle, P. Moral and J. M. M. Millet, *J. Phys. Chem. Solids*, 1997, **58 (10)**, 1539.
61. S. Si, A. Kotal, T. K. Mandal, S. Giri, H. Nakamura and T. Kohara, *Chem. Mater.*, 2004, **16 (18)**, 3489.
62. D. K. Kim, M. Mikhaylova, Y. Zhang and M. Muhammed, *Chem. Mater.*, 2003, **15 (8)**, 1617.
63. A. A. Novakova, V. Y. Lanchinskaya, A. V. Volkov, T. S. Gendler, T. Y. Kiseleva, M. A. Moskvina and S. B. Zezin, *J. Magn. Magn. Mater.*, 2003, **258**, 354.
64. V. S. Zaitsev, D. S. Filimonov, I. A. Presnyakov, R. J. Gambino and B. Chu, *J. Colloid Interface Sci.*, 1999, **212 (1)**, 49.
65. M. A. Karakassides, D. Gournis, A. B. Bourlinos, P. N. Trikalitis and T. Bakas, *J. Mater. Chem.*, 2003, **13 (4)**, 871.
66. A. C. Doriguetto, N. G. Fernandes, A. I. C. Persiano, E. Nunes Filho, J. M. Greneche and J. D. Fabris, *Phys. Chem. Miner.*, 2003, **30 (5)**, 249.
67. R. E. Vandenberghe, C. A. Barrero, G. M. da Costa, E. Van San and E. De Grave, *Hyperfine Interact.*, 2000, **126 (1–4)**, 247.
68. P. Coquay, E. De Grave, R. E. Vandenberghe, C. Dauwe, E. Flahaut, C. Laurent, A. Peigney and A. Rousset, *Acta Mater.*, 2000, **48**, 3015.
69. F. J. Berry, S. Skinner and M. F. Thomas, *J. Phys.: Condens. Matter*, 1998, **10 (1)**, 215.
70. I. V. Murin, V. M. Smirnov, G. P. Voronkov, V. G. Semenov, V. G. Povarov and B. M. Sinelnikov, *Solid State Ion.*, 2000, **133 (3–4)**, 203.
71. G. M. da Costa, E. De Grave, P. M. A. de Bakker and R. E. Vandenberghe, *J. Solid State Chem.*, 1994, **113 (2)**, 405.
72. F. X. Redl, C. T. Black, G. C. Papaefthymiou, R. L. Sandstrom, M. Yin, H. Zeng, C. B. Murray and S. P. O'Brien, *J. Am. Chem. Soc.*, 2004, **126 (44)**, 14583.
73. E. Van San, E. De Grave and R. E. Vandenberghe, *J. Magn. Magn. Mater.*, 2004, **269**, 54.
74. F. Rouquerol, J. Rouquerol and K. Sing, *Adsorption by powders and porous solids*. Academic Press, London, UK, 1999.